Title	Optimization of Dry Etching Processes and Characterization of Optical Properties on Photonic Crystal Laser with Circular Resonator
Author(s)	張, 秀宇
Citation	大阪大学, 2018, 博士論文
Version Type	VoR
URL	https://doi.org/10.18910/69585
rights	Copyright ©2017 IEICE
Note	

Doctor Dissertation

Optimization of Dry Etching Processes and Characterization of Optical Properties on Photonic Crystal Laser with Circular Resonator

（円形共振器を用いたフォトニック結晶レーザにおける

ドライエッチングプロセスの最適化と光学特性の評価）

Xiuyu Zhang

July 2017

Graduate School of Engineering,

Osaka University

Abstract

This dissertation addressed the research of the dry etching process for fabricating photonic crystal (PhC) structure in a GaAs/AlGaAs-based epi-wafer and optical measurement of the PhC laser with a circular resonator.

Chapter 1 introduces the research background. It explains the basic mechanism of utilizing PhC structure to realize the quantum photonic devices, and introduces the structure of the PhC laser with a circular resonator proposed by Kondow Laboratory. The proposed PhC laser is called as CirD laser for abbreviation of circular defect cavity laser. The basics of the proposed CirD laser, including the lasing mechanism and the band diagram are presented in Chapter 1. The lasing mechanism of CirD laser is similar with typical micro disk lasers. The requirements of the resistivity and the *Q* factor for the realizing electrically driven CirD laser have also been investigated in this chapter. A structure which can realize wavelength-division multiplexing (WDM) using the CirD lasers emitting different wavelength is also proposed. Furthermore, the features of CirD laser and other PhC lasers researched by other groups were compared. CirD laser shows advantages in the ability of high integration density, which is important to achieve WDM with high transmission bandwidth.

Chapter 2 introduces the basics of the fabrication and measurement techniques used in this study, including the electron beam (EB) lithography, inductively coupled plasma (ICP) dry etch, and scanning electron microscope.

Chapter 3 discussed deep dry etching process of $Al_{0.8}Ga_{0.2}As$ and GaAs substrate for PhC fabrication using a Cl_2, BCl_3, and CH_4 mixed gas. In this chapter, SiN_x and SiO_2 are both used as the mask layer in dry etching process for $Al_{0.8}Ga_{0.2}As$. Samples with SiN_x and SiO_2 masks for deep dry etching were fabricated and compared. The results show that different materials of mask may affect the trajectory of the incident ions during the dry etching process, and the profiles of the etched air holes are different as a result. Finally, it is found that using a SiN_x mask with the

thickness of 80 nm, deep air holes with fine profiles can be achieved on the $Al_{0.8}Ga_{0.2}As$ substrate. During the process of optimizing the dry etching of GaAs, the EB lithography process was firstly optimized for obtaining larger diameter of the air holes in the PhC structures. The lines of the PhC structure were also increased for eliminating the adverse impact induced by the proximity effect in the EB lithography process. Finally, air holes with high regular shape and depth of 1.4 μm were etched in the GaAs substrates by using the etching parameters optimized for etching $Al_{0.8}Ga_{0.2}As$ substrate and a SiN_x mask with the thickness of 150 nm.

Chapter 4 discussed the optimization of ICP dry etching process for etching the GaAs/AlGaAs-based epi-wafer. The structure of the epi-wafers used in this chapter is similar with the one used for fabricating the electrical driven CirD laser. The epi-wafer contains various materials for different stacked layers, like GaAs, $Al_{0.95}Ga_{0.05}As$, and InAs quantum dots. However, the InAs quantum dots in the epi-wafer cause the contraction of the diameter in the air holes during the etching process. By enhancing the physical etching effect, the verticality of the profile for the air holes etched in the epi-wafer with heterostructure is greatly improved.

Chapter 5 discussed the optical measurement of the fabricated PhC laser having a circular defect cavity and a line defect output waveguide, which is fabricated on an epi-wafer consisting of a slab layer with InAs quantum dots and an AlO_x cladding layer. Samples with different parameters have similar threshold values of about 25 μW. Room-temperature continuous-wave lasing operation at 1.3 μm range is confirmed by observing the spectrum of output light from the line defect waveguide. The wavelengths of the lasing modes show the dependence on the radius of the circular resonator and the radius of air holes, which indicate that the lasing mode is the whispering-gallery mode.

Chapter 6 presents the conclusion of this study and the achievements obtained in this study.

For the first time, I fabricated the PhC laser having a circular defect cavity using various techniques, such as EB lithography and dry etching process. The fabricated samples show single-mode lasing operation under room-temperature continues-wave condition. It implies that the PhC laser with circular defect cavities is promising for WDM laser sources.

Contents

Chapter 1

Introduction

1.1 Background

The amount of data transferred through networks is rapidly increasing all over the world, and powerful optical communication systems are used in these networks. Recent advances in photonics technologies have made optical interconnection network an attractive option for computing systems covering high-performance computers, data centers, automobiles and so on.

Today, microprocessors used in computers have multicores. Electrical signals are currently used for data communications between cores. However, the classic microprocessors which use metal buses to connect each core have drawbacks. For example, communications between distant cores require multiple routing hops. The resistance of the metal buses becomes higher when the length of the buses is longer and width is smaller, and overlapping messages experience significant contention. As a result, the electrical connections used in the microprocessors cause many limitations in improving the bandwidth of each core and limit the computing power of the microprocessors. Therefore, replacing the electrical datacom system in the multi-core microprocessors with optical data communication technology is a possible option in the future because optical data communication technology has promised to allow a higher bandwidth than the communication systems using electrical signals. The technology used to connect each core in microprocessors is also the basic concept for realizing the intra-chip interconnections. Assume that an optical broadcast network is designed to connect several cores on one single chip. Each core transmits multiple-wavelength lasing signals and receives some set of signals from the waveguide. So that benefitting from the advantages of the optical communications, such as low power consumption and extreme high transmission bandwidth, drastically improvements of the computing power for the microprocessors can be expected. Both supercomputers and personal computers will benefit from this technology. It will also radically change the architecture of the processors today and breed new processor designs.

One of the challenges in realizing intra-chip optical interconnections is to develop proper light sources. Traditional light sources used in current optical communication systems cannot be applied to intra-chip optical interconnections because intra-chip optical interconnections need light sources with an extreme small footprint for integrating the light sources with the cores on the same chip.

The development of room-temperature (RT) continuous-wave (CW) operated semiconductor lasers closely influences the evolution of optical communication systems. InP-based distributed feedback lasers were initially applied to telecommunication networks which are long-reach optical-fiber communication systems [1,2]. Recently, optical communication technologies have begun to be applied to short-reach data transmission in datacenters (datacom) as optical interconnections between electronic circuit boards. Some light sources have been replaced by Vertical-cavity surface-emitting lasers (VCSEL) whose active volume is smaller. The power consumption of transmitters decreased greatly due to the reduction of active volume. The whole optical transmission system benefits from the invention of VCSELs and are widely used for datacom networks [3,4]. The next challenge is developing proper light sources which can be applied to intra-chip transmissions in microprocessors.

Photonic crystal (PhC) cavities can strongly confine photons in a very small volume with a very high quality factor (Q factor) [5,6]. Due to the small active volume and high Q, PhC cavity lasers are considered to be used as a light source with ultra-low threshold lasers for usage in short-range optical communication systems. Furthermore, the cavity Q factor per modal volume V, Q/V, determines the strength of various cavity interactions, so that the strong light-matter interaction opens up new possibilities in various fields, such as more efficient light sources, low-threshold nanolasers, and photonic chips. Therefore, PhC cavity lasers are considered one of the best candidates with small footprint and ultra-low threshold lasers which can be applied to intra-chip optical interconnections. The applications of PhC cavity lasers can bring the next evolution in photonic networks by realizing intra-chip transmission in microprocessors.

1.1.1 Photonic crystal

PhC is proposed by Yablonovitch [7] and John [8] in 1987. PhC structures are generally formed by periodic dielectric nanostructures. According to the dimensions of the periodic stacks, one, two or three-dimensional PhC structures can be realized. The simplest PhC structures is constructed by two periodically stacked dielectrics which is denoted as one-dimensional (1D) PhC structure. An ideal two-dimensional (2D) PhC structure is periodic in two directions and homogeneous in the third direction. 2D and three-dimensional (3D) PhC structures are attracting particular attention in recent years.

2D PhC structure is adopted in this study because 2D PhC geometries can be practically constructed, and have the ability of the applications in guiding and manipulating light in planar defect designs. These features are important for realizing a laser device. There are many kinds of lattice types in 2D PhCs. The universal types are the triangular and square lattice. The PhC structures using triangular lattice have a larger PBG area than the PhC using a square lattice [9]. Larger PBG area has advantages in giving higher tolerance for determining the parameters of the PhC structure when designing the devices. Therefore, triangular lattice is used in designing the laser structure in this study. Besides the lattice types, there are two basic topologies for 2D PhCs using a triangular lattice as depicted in Fig. 1.1(a) and 1.1(d). The PhC structure shown in Fig. 1.1(a) is constructed by low index dielectric holes in high index dielectric materials. This topology structure is denoted as a hole type. The PhC structure shown in Fig. 1.1(d) is constructed by high index dielectric rods surrounded by low index materials. This type is denoted as pillar type. The distance between two holes or rods is the lattice constant a. For calculating typical band diagrams for these two PhC strctures, the radius of the air holes and rods r are both set as $0.3a$. Air and GaAs are widely used as the low index dielectric material and high index dielectric material, respectively, for fabricating basic 2D PhC structures. Therefore, the dielectric constants of low index dielectric materials are set as 1.0 and the dielectric constants of high index dielectric materials are set as 11.6. By observing the band diagrams shown in Fig. 1.1(b) and 1.1(e), the hole type of 2D PhC structure has a complete photonic band gap (PBG) of transverse electric (TE) mode, and the pillar type has a PBG of transverse magnetic (TM) mode. Generally, the pillar type structure is suited for designing devices with the application of TM light and the hole type structure is suited for designing devices with the application of TE light.

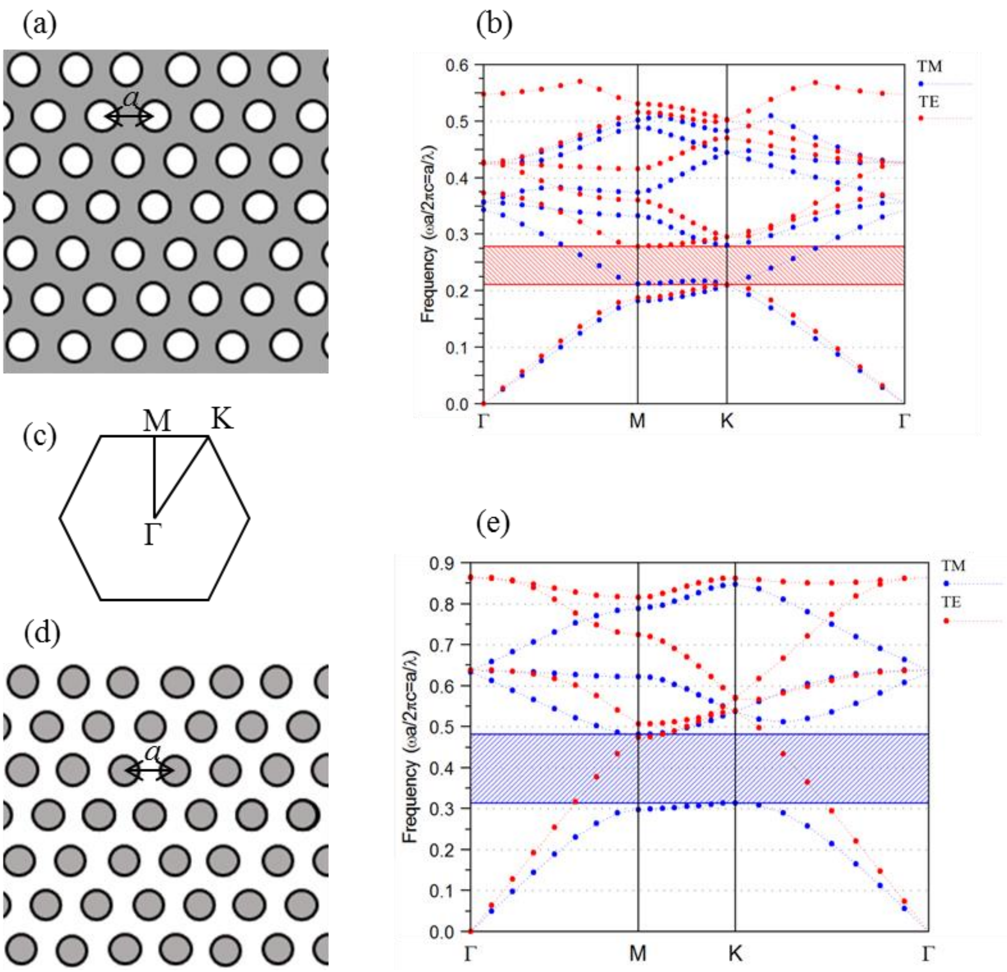

Fig. 1.1 (a) A typical 2D PhC structure using hole type where the radius of the air holes r is $0.3a$. (b) Band diagrams and PBG for triangular lattices of hole type. (c) The Brillouin zone of triangular lattices. (d) A typical 2D PhC structure using pillar type where the radius of the air holes r is $0.3a$. (e) Band diagrams and PBG for triangular lattices of pillar type.

The InAs quantum dots (QDs) are used as the gain materials in fabricating the PhC cavity lasers in this study. Due to the biaxial strain effects [10], the gain of TE mode increases with increasing compressive strain in the gain materials. Therefore, the InAs QDs are supposed to have high gain of TE modes due to the high compressive strain. The emitting light form the QDs are expected to be lights with TE mode. Therefore, we adopted the 2D PhC structure using hole type and triangular lattices for fabricating the PhC laser in this study. The basic PhC structure used in this study is based on a slab having triangular arranged air holes on GaAs. The bird view of the triangular lattice in the PhC structure is shown in Fig 1.2. The dielectric constants of air and GaAs are ε_1=1.0 and ε_2=11.6. The basic parameters of the PhC structure is the lattice constant a, the radius of the air holes r, and the thickness of the slab d. By using a PhC structure like this, the confinement of light in the vertical direction is strong, so that the region outside the air light cone is wide. A broad PBG can be obtained by using this structure.

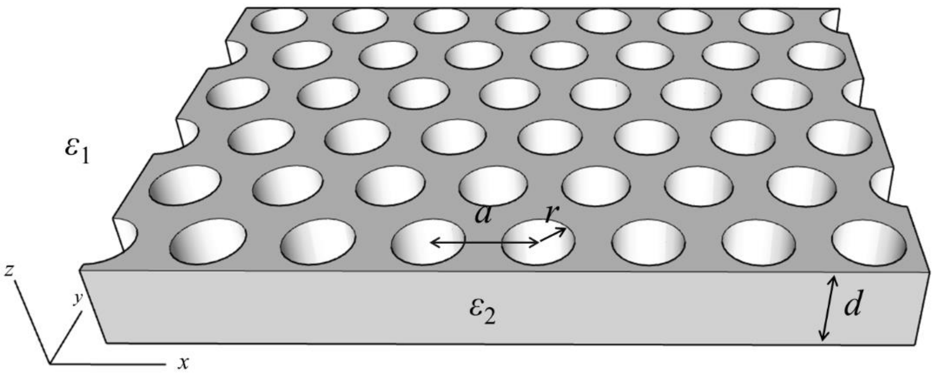

Fig. 1.2 The bird view and parameters of the PhC structure used in this study. a is the lattice constant of the triangular lattice and r is the radius of the air holes. ε_a and ε_b represent the dielectric constants of air and GaAs.

Defect region with various shapes can be introduced in a 2D PhC structure for realizing resonator cavities or waveguides. When a point defect or small hexagonal defect is created in a photonic crystal, it is possible for that defect to pull a light mode into the band gap. Because such a state is forbidden from propagating in the PhC, the light can be trapped. The mode decays exponentially into the PhC area. By changing the size or the shape of the defect, its frequency can easily be tuned to any value within the band gap.

When a defective cavity is introduced into a PhC structure, the light can be confined in the defect region. The defect region can be treated as a resonator. Q factor is a dimensionless parameter that describes how under-damped an oscillator or resonator is, and characterizes a resonator's bandwidth relative to its center frequency. Higher Q indicates a lower rate of energy loss relative to the stored energy of the resonator. It also means that the ability of light confinement is better. Q is defined as

$$Q = w_0 \frac{U}{-dU/dt}, \tag{1.1}$$

where w_0 is the resonance frequency, and U is the electromagnetic energy at time t [12,13]. The resolution of this equation is

$$U = U_0 \exp(-w_0 t / Q). \tag{1.2}$$

U_0 is the stored energy in the resonator when t=0. Therefore, the light can be stored in the resonator for a long time when Q is larger and the loss is little. The attenuation of energy in the resonator can be evaluated by using Q factor. In the simulation process using Finite-difference time-domain (FDTD) method, Q factor was derived from Eq. (1.2) which is obtained by calculating the attenuation of energy in the resonator.

The defect in PhC structure can also be formed as the line shape or line shape with bend. In these cases, the light with the frequency which corresponding to the complete PBG of the PhC structure cannot propagate through the periodic structure. Therefore, the light can be confines and guided through the line defect. The line shape defect can be treated as a waveguide with the size closing to wavelength [11].

1.1.2 Overview of PhC lasers

Although Some research groups have proposed and discussed PhC lasers using various designs [12-25], PhC cavity lasers have not been widely applied in the optical communications industry yet because of the lack of practical electrically driven devices. Most reports on PhC cavity lasers are optical pump lasers [21-29]. In order to minimize radiation loss through the cladding layers, air or SiO_2 is generally used to clad the 2D PhC slab. But it is difficult to develop practical devices because carrier injection is difficult through the insulator of cladding layers, resulting in the difficulty in developing practical devices. Since low resistivity is required for high-speed operation, it is an important and challenging task to design a device structure in which light confinement and carrier injection are highly compatible with each other. Therefore, most reported PhC cavity lasers still use optical pumping structures, and several researchers are pushing the study on realizing electrical pumping devices [13-20]. The following introduces the reported PhC lasers.

Lee's group at the Korea Advanced Institute of Science and Technology (Daejeon, South Korea) demonstrated the first electrical pumping of a single-nanocavity laser [13,14]. The group applied a ring contact to an n-type surface layer on top of a thin PhC slab, with a central post beneath the slab connecting to the p-type InP substrate. However, this device can only operate under pulse conditions due to large electrical resistance and thermal resistance.

Matsuo et al. obtained lasing by developing so called lambda-scale embedded active-region photonic-crystal laser (LEAP laser) which used a lateral current injection structure [15-18]. They fabricated a pin-junction in the plane of the PhC slab by using Zn diffusion and Si ion implantation into the non-doped InP burying region. LEAP laser is the world's first current-injection PhC laser operating with CW light at RT [4]. A threshold current of 14 μA and high-speed modulation at 10 Gbit/s and energy cost of 170 fJ/s were demonstrated on LEAP laser at room temperature. However, LEAP laser has a low output power of about 10 μW which should be attributed to the high electrical resistance and lateral current injection structure.

Noda et al. [19] have also demonstrated a kind of laser fabricated with PhC structure which is called as Photonic Crystal Surface Emitting Lasers (PCSEL). The vertical constructive structure of PCSEL is similar with VCSEL. An n-AlGaAs cladding layer, an active layer containing InGaAs/AlGaAs multi quantum wells, and an AlGaAs carrier blocking layer and a GaAs layer were successively grown on an n-GaAs substrate. A 2D PhC structure consists of a square lattice was then fabricated on the top GaAs layer. Watt-class high-power, single-mode operation of lasing is obtained on PCSELs under RT-CW conditions. The lasing mechanism of PCSEL is different from PhC lasers with a cavity. The lasing principle of the PCSEL is based on the band-edge effect of a 2D PhC [19]. PCSEL usually need relative large footprint with the size of 100×100 μm for obtaining high output power. However, the light generated in the PhC cavity laser is confined and amplified in the resonator.

Crosnier et al. [20] reported a 1D PC cavity laser made in InP nanoribs. The specific nanorib design enables an efficient electrical injection of carriers in the nanocavity without spoiling its optical properties. The 1D PhC nanocavity lasers consists in a 450 nm thick, 600 nm wide and 15 μm long InP-based rib waveguide drilled with a single row of equally sized holes with the radius of 90 nm. The hole-to-hole distance radually increases from 300 nm in the centre of the structure to 330 nm. The nanorib structure keeps the radiative losses to a minimum. RT-CW single-mode operation is obtained with a current threshold of 100 μA and laser emission is at 1.56 μm.

1.1.3 CirD laser

Kondow Lab proposed a novel design of a current-driven PhC cavity laser which is aim to realize intra-chip optical communications [30,31]. The structure of the proposed PhC cavity laser are shown in Fig. 1.3. It is called as CirD laser for the abbreviation of circular defect cavity laser which is fabricated in a 2D PhC structure. CirD laser also has a vertical current injection structure. The details of the CirD laser is introduced as follows.

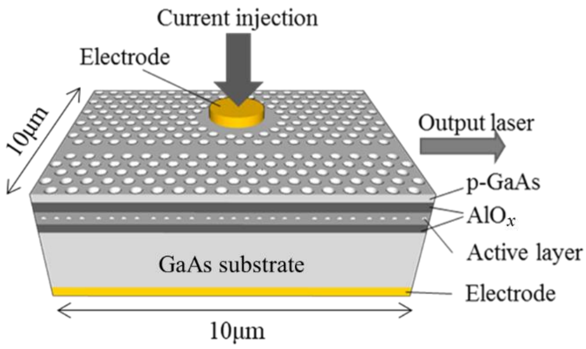

Fig. 1.3 Schematic illustrated structure of CirD laser [32]. CirD laser is proposed for aiming to realize intra-chip optical communications. It has a vertical current injection structure.

InAs QDs are considered to be used in the active region of the CirD laser. Generally, for obtaining the 1.30 μm or 1.55 μm range emitting, the active regions of lasers usually use GaInAsP/InP-based materials [33]. However, the barrier between the core layer (GaInAsP) and the light emitting layer (GaInAsP with different composition) is small in the GaInAsP/InP-based lasers. The illustration of the energy barrier is shown in Fig. 1.4. Thus, the threshold increases and light emitting efficiency decreases when the temperature is higher. On the other hand, InAs QDs can be grown on GaAs substrates which is cheaper than growing on InP substrates. If AlGaAs with large bandgap was used as the cladding layer, the barrier between the GaAs layer and the light emitting layer (InAs QDs) is relatively big. Therefore, the lasers using GaAs/AlGaAs-based materials have advantages, such as better thermal stability, low power consumption, and low cost. The lasing mechanism of CirD laser is very similar with the micro disk lasers which will be expound in Section 1.2 with details.

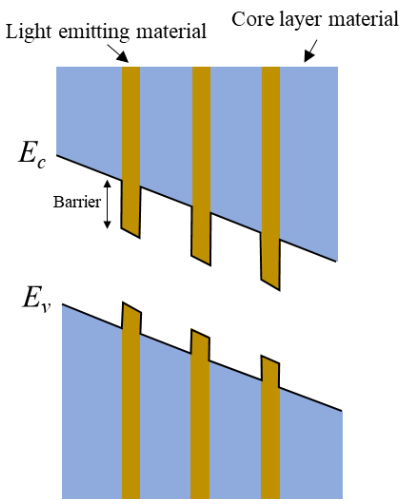

Fig. 1.4 A typical energy band diagram of the core layer in a laser which has triple light emitting layers. The barrier is the energy offset between the light emitting material and the core layer material.

For realizing the CirD lasers, the plane design consists of a circular defect on a 2D PhC structure as the cavity and a line defect as a waveguide. A typical plane view of a typical CirD laser is shown in Fig. 1.5. The defect cavity is obtained by removing air holes and shifting the air holes around the cavity into a round shape. A waveguide which is formed by line defect was placed beside the circular cavity. The light generated in the cavity can couple to the waveguide and output through the horizontal direction.

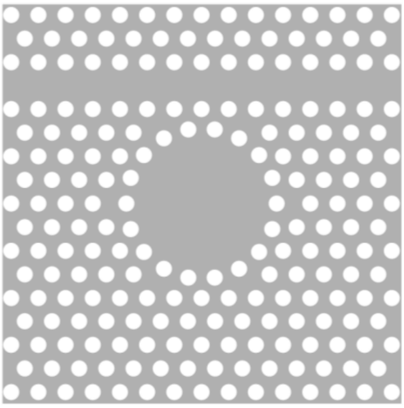

Fig. 1.5 The plane view of a typical CirD laser. The circular defect on the 2D PhC structure serves as the resonator, and the line defect serves as a waveguide.

The cross sectional view of the vertical structure of the CirD laser is shown in Fig. 1.6. As depicted in the picture, CirD laser is fabricated on a GaAs/AlGaAs-based epi-wafer. The epi-wafer has one GaAs cap layer, two AlGaAs layers, and a core layer consisting InAs QDs in GaAs, which are grown on a GaAs substrate. The pattern shown in Fig. 1.5 is drawn on the epi-wafer firstly using electron beam lithography. Air holes are fabricated in the epi-wafer using dry etching process. Then aluminum oxide AlO_x cladding layers are obtained from oxidizing AlGaAs around the air holes. The refractive index of AlO_x is 1.6 [34], which is much smaller than that of AlGaAs (2.9 at 1 eV), so improvement of light confinement can be expected. Furthermore, the AlGaAs remained in the center of the cavity area is used for current injection. Therefore, as a standard for low power consumption, we decided to target 200 Ω for the proposed CirD laser by concerning the electrical resistance of VCSEL which is about 50 to 100 Ω [35]. This value is much lower than the resistance of 5.4 kΩ for the reported LEAP laser [36]. The circular resonator is required to have a structure with good ability of light confinement and low electrical resistance which is essential for realizing electrical driven devices.

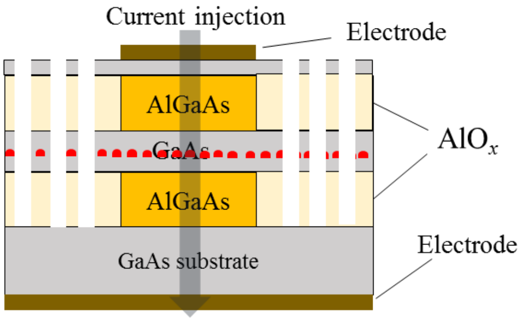

Fig. 1.6 Cross sectional structure of CirD laser. The AlGaAs remained in the center of the cavity area is used for current injection, and the device has a vertically current injection structure.

1.2 Basics of CirD laser

1.2.1 Circular resonator

One of the most important parts of the CirD laser is the circular defect on the 2D PhC structure. The circular cavity acts as a resonator and confines the light. Here introduces the formation of the circular defect. Figure 1.7(a) shows the plane view of a typical 2D PhC structure with circular air holes arranged by triangular lattice. The lattice constant is denoted as a, and r is the radius of the air holes. When air holes constructing a hexagon having 3 air holes on each side are removed to form a cavity as shown Fig. 1.7(b), the defect is usually denoted as H3 structure. The circular cavity used in this study is modified from a H3 structure. If the air holes around the peripheral of the H3 defect was shifted to a circular shape as shown in Fig. 1.7(c), a circular defect cavity can be obtained. The circular defect is denoted as modified H3 structure. R is the radius of the circular cavity.

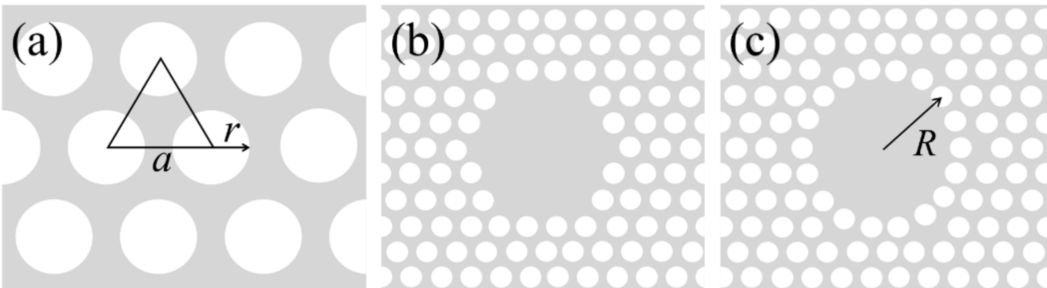

Fig. 1.7 (a) Schematic illustration of a typical 2D PhC structure, (b) H3 defect, and (c) modified H3 defect.

Whispering gallery mode (WGM) can also be expected in the circular resonators for CirD lasers. Figure 1.8 shows the distribution of magnetic field of the WGM in a typical circular cavity calculated by 3D FDTD method [37-40]. Because the cavity is circular and there are 18 air holes on the peripheral of the circular cavity, the WGM has 18 antinodes where is the highest amplitude for the standing wave. Furthermore, when the radius of the circular cavity is modified, the wavelength of the WGM changes for fitting the peripheral of the circular cavity [30].

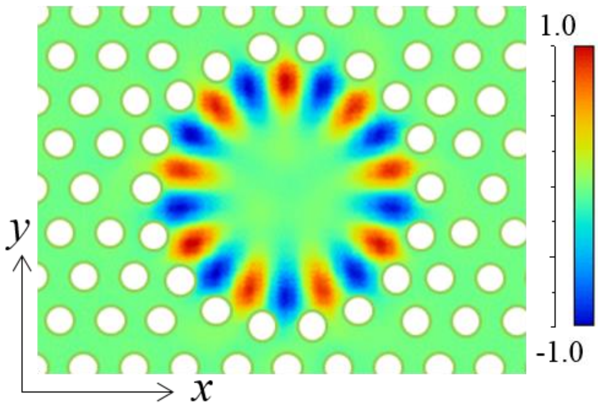

Fig. 1.8 A typical distribution of magnetic field of WGM in the circular cavity calculated by 3D FDTD method. There are 18 antinodes where is the highest amplitude for the standing wave of the WGM, because there are 18 air holes on the peripheral of the circular cavity.

The circular cavity used in this study is modified from a H3 structure. However, this kind of circular cavity can be obtained by modifying a hexagonal defect on the PhC structure having a length of side with any number of air holes. The PhC laser reported by Lee's group [25] adopted a H2 cavity which obtained pulsed lasing operation at RT. An H2 cavity is constructed by a hexagonal defect on the PhC structure having a length of side with 2 air holes. Considering the smaller area of the cavity comparing with the H3 cavity, the resistance of the PhC lasers using a -H2 structure is too high to realize RT-CW operation. On the other hand, the cavities using H4 structure or bigger area have lower *Q* factors which may not meet the requirement for lasing [41].

Therefore, the modified H3 structure is the best option for fabricating the CirD laser.

There two important requirements for realizing the electrically driven CirD laser. One requirement is concerning the resistivity of the CirD laser, another is about the Q factor of the circular resonator. Typical resistance values for VCSEL are 50 ~ 100Ω [42,43]. Since the CirD laser has a small foot print size, it will have small capacitance. Therefore, the resistance can be several times larger than that of VCSEL. Furthermore, the resistance of CirD laser is inversely propotional to the area of the circular defect cavity. For obtaining smaller resistance, the area of the cavity should be large enough. The resistivity ρ of the proposed CirD laser can be estimated using the following equation.

$$\rho = \frac{1}{\sigma} = \frac{1}{en\mu}, \tag{1.3}$$

where e represents elementary charge, σ is the conductivity, n is the carrier density and μ is the mobility. Assuming that the thickness of the upper and down AlGaAs cladding layers are total 1 μm, and carrier density is 10^{18} cm^{-3}. The mobility of AlGaAs is assumed as 100 cm^2/Vs. The resistivity of AlGaAs is about 10^{-3} Ω·cm. Moreover, the resistivity of the GaAs core layer is also about 10^{-3} Ω·cm. Therefore, the estimated resistance of typical CirD laser is smaller than 0.2 kΩ when the area of the cavity is larger than 1 μm^2. This value is much less than values of reported electrically driven PhC lasers [35,36].

According to the calculated curves of the threshold current density as a function of Q factor for a PhC cavity laser [17,31], the Q factor of the cavity should be higher than 4000, so that the threshold current density is small enough for RT-CW lasing. Before fabricating the CirD laser, the parameters, such as the lattice a, the radius of the air holes r, and the radius of the circular cavity R, should be well designed for meeting the requirment of Q factor.

1.2.2 Lasing mechanism

The lasing mechanism of CirD laser is very similar with the micro disk lasers which have been widely researched. Figure 1.9(a) and 1.9(b) show schematic illustrations of cross sectional view and bird view for a typical micro disk laser [44,45]. The core layer containing gain material, such as quantum wells or quantum dots, is sandwiched by two cladding layers with lower refractive index materials. The carriers (electrons and holes) are pumped into the core layer and gain material from the n and p regions respectively. Holes are injected from the p doped region, and electrons from the n doped region. When an electron and a hole are present in the same region, they may recombine and produce a spontaneous emission. Spontaneous emission is necessary to initiate laser oscillation. When the input current is higher than the threshold current, a nearby photon with energy equal to the recombination energy can cause recombination by stimulated emission. This generates another photon of the same frequency, polarization, and phase, travelling in the same direction as the first photon. This means that stimulated emission will cause gain in an optical wave in the injection region, and the gain increases as the number of electrons and holes injected across the junction increases. Photons emitted into a mode of the resonator will travel around and be reflected on the peripheral of the inner side wall of the resonator, which is also called as WGM [46,47]. As a light wave passes through the cavity, it is amplified by stimulated emission, but light is also lost due to absorptions. Finally, if there is more amplification than loss, the diode begins to lase. Because similar current injection structure also exists in the CirD laser as shown in Fig. 1.9, the lasing mechanism is almost the same. The carriers are injected and laser light emits due to the stimulated emission. The WGM also generates in the cavity which should be attributed to the circular shape of the cavity. One difference is that the absorptions is the main loss in the micro disk laser. For the CirD laser, the loss in the 2D PhC structure should be also considered beside the absorptions. Another difference is that the light generated in the micro disk laser is confined by the air clad. On the other hand, the light generated in the core layer of CirD laser is confined by the 2D PhC structure and the AlO_x cladding layers. The micro disk lasers usually need another designed dielectric waveguide placing beside the core layer in specialty for output. Comparing with the micro disk laser, CirD laser has one advantage that the light can be easily output by using a line defect waveguide on the PhC structure. The waveguide and the cavity can be integrated in one PhC structure without any other redundant component.

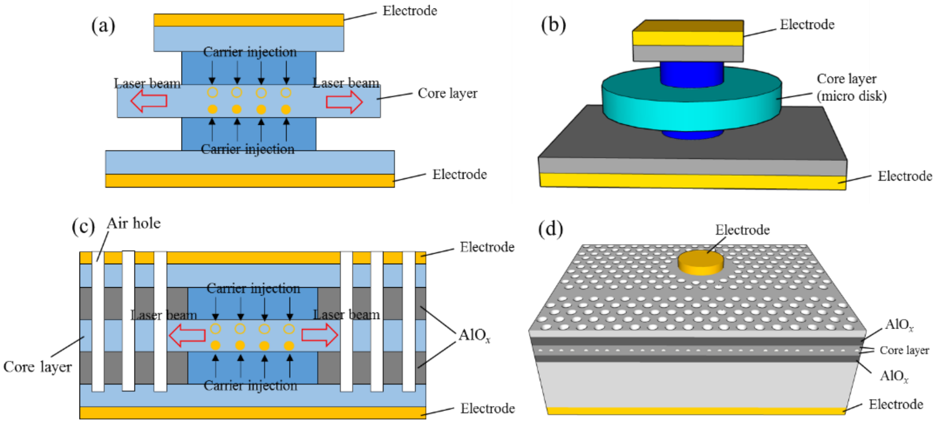

Fig. 1.9 Schematic illustration of (a) cross sectional view and (b) bird view of a typical micro disk laser. (c) Cross sectional view and (d) bird view of the CirD laser. The carrier injection structure is almost the same. Micro disk laser usually uses air cladding, and CirD laser uses 2D PhC structure and AlO_x cladding layers for light confinement.

Figure 1.10 shows the band structure distribution of the carrier injection part in the CirD laser. The GaAs core layer is sandwiched by the p-type and the n-type AlGaAs cladding layers. In a thermal equilibrium state, the electrons and holes exist separately in the n-type region and the p-type region. If a forward bias voltage is added to the junction, the potential of the n-type region is up injecting a small number of carriers. The carriers can be trapped in the core layer due to the energy offset between AlGaAs and GaAs. For suppressing the surface recombination on the side wall of the air holes, InAs QDs are used as the gain material. The GaAs core layer is implanted with multi-stacked layers of InAs QDs with high density, and the band diagram for the core layer is shown in Fig. 1.10(b). When the conditions for stimulated emission is met, light amplification was performed. Then, light wave generated from stimulated emission is trapped and amplified in the core layer due to confinement of the PhC structure and refractive index difference between GaAs and AlO_x. By trapping the light wave and carrier, it is possible to achieve laser oscillation with high efficiency.

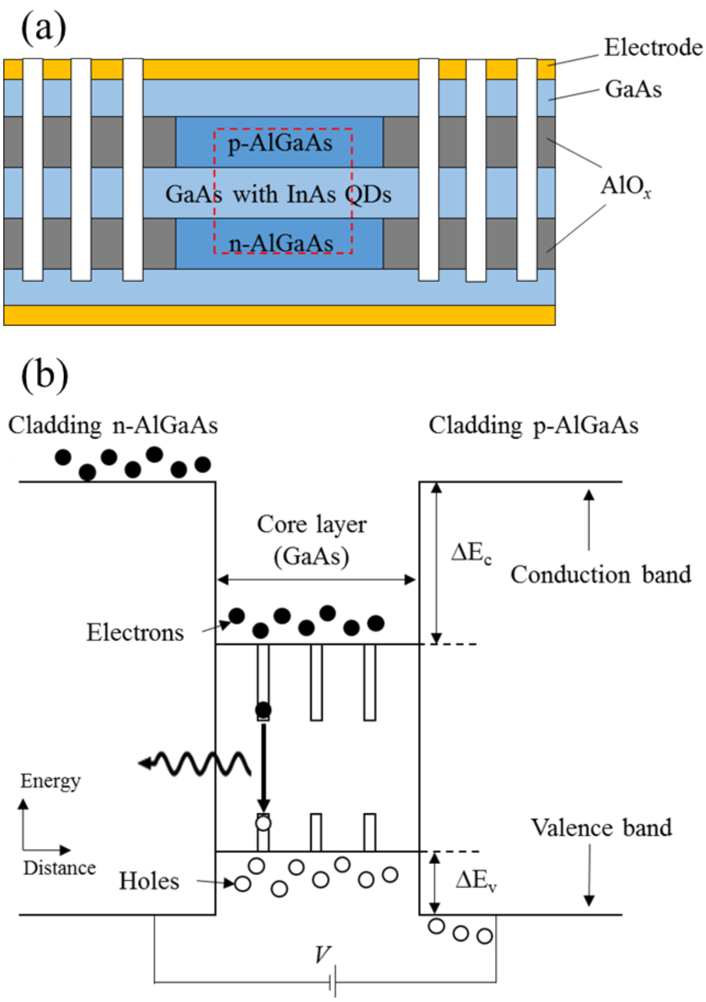

Fig. 1.10 (a) The cross sectional structure of a typical CirD laser. (b) Schematic illustration of the band structure for the current injection part in the CirD laser where is marked in Fig. 1.10(a).

1.2.3 Parameters of the PhC structure for the CirD laser

For ensuring the lasing operation of the CirD laser, the parameters of the 2D PhC structure should be well designed. Two conditions should be satisfied according to the lasing mechanism. One condition is that the cavity mode should be confined in the cavity with low radiation loss. It means that the frequency energy of the cavity mode should be contained in the PBG of the 2D PhC structure. The other condition is that the Q factor of the cavity should meet the requirement of lasing. The following discussion is using these two conditions to confine the parameters of the PhC structure for the CirD laser.

Concerning a GaAs based 2D PhC structures formed by a periodic array of holes arranged in a triangular lattice fashion, the PBG maps' dependence on filling ratio *r/a* with variance of *a* is shown in Fig. 1.11. The inset picture in Fig. 1.11 shows the PhC structure while *a* is the lattice constant and *r* is the radius of the air holes. The PBG map for each *a* is constructed by the complete PBG of the PhC structures with various *r*. For example, the arrow line marked in the figure demonstrates the complete PBG for the PhC structure with *a* of 340 nm and *r* of 0.3a. The vertical axis is set to be wavelength instead of frequency in regular PBG map figures, so that the upper and lower limits are reversed in Fig. 1.11 comparing with the band diagrams shown in Fig. 1.1. The cavity resonant modes should vary from 1.30 μm to 1.32 μm due to the applications of optical communications as shown in the gray area in Fig. 1.11. The wavelength range must be included in PBG map for confining the cavity modes. The crossover points of 1.3 μm wavelength on the PBG upper limits are the required minimum *r/a* for each *a*, and it is smaller when *a* is smaller. In this study, *a* was set as 340 nm during the fabricating processes. Therefore, the corresponding required minimum *r/a* is 0.28 when a is 340 nm, and *r/a* should not exceed 0.42. In summary, CirD lasers operating at the 1.3-μm range can be realized by fabricating circular cavities with various diameters, and a communal waveguide on this 2D PhC structure with *a*=340 nm and *r/a* higher than 0.28.

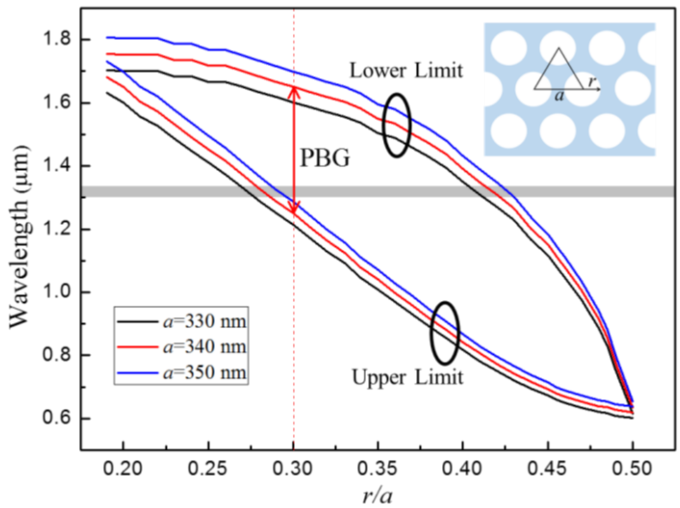

Fig. 1.11 Simulated PBG maps of the GaAs based 2D PhC structure for TE polarized light with various *a*. The inset picture shows the PhC structure.

On the other hand, in order to ensure that the Q factor of the circular resonator is high enough for lasing, the variable parameters of the samples, which are the radius of the air holes r and the radius of the circular cavity R, should be well designed. According to the calculated curves of the threshold current density as a function of Q factor for a PhC cavity laser [17,31], the Q factor of the cavity with a line defect waveguide should be higher than 4000, so that the threshold current density is small enough for RT-CW lasing. The Q factor of WGM by using 3D FDTD method was calculated because only WGM had large Q factor in the cavity. Figure 1.12 shows the calculated Q factor of the structure consisting of a circular defect cavity and a line defect waveguide with various R and r when a is 340 nm. It shows that Q factor is larger than 4000 when $2.75a \leq R \leq 2.77a$ and $0.29a \leq r \leq 0.33a$. It means that CirD lasers with designed parameters have high Q factor larger than 4000. The circular resonators within these parameters are expected to have small thresholds and lasing operations.

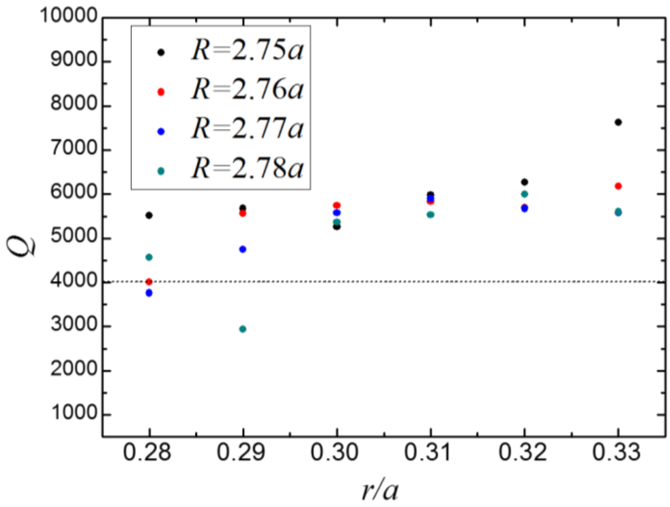

Fig. 1.12 Q factor for the optical pump CirD laser with various parameters. The points in the figure represent simulated structures with a=340 nm, $2.75a \leq R \leq 2.77a$ and $0.29a \leq r \leq 0.33a$.

1.3 Comparison and motivation

There are lot of reports about micro resonators using PhC structures which have been introduced in Section 1.1.2. However, PhC lasers have not been practically used until now because most reports are just optical excitation experiments. The practical use of PC lasers will not be realized until lasers with proper structure and properties are developed.

Noda *et al.* has researched and developed surface-emitting PhC lasers with current drive. Now, they are available on the market. However, their lasers have huge resonators and aim to high power applications. What we have researched and developed are lasers used for optical communications. In modern Information and Communication Technology (ICT) society, improving the properties of laser diodes (LD) used in optical communications is an urgent and challengeable research topic. Because there are some mature technologies in LD, developments of new breakthrough technologies are limited. Accordingly, PhC lasers with cavity resonators are expected. In this field of application, only LEAP laser developed by Matsuo's group in NTT and 1D PhC nanorib cavity laser developed by Crosnier et al. have realized RT CW operation.

Although LEAP-LD is the world's most advanced PhC laser, the road to commercialization is still long. According to their paper [18], the footprint of the device could be one problem. Because of the big footprint, there will be less devices fabricated on one wafer, so that LEAP-LD is hard to commercialize due to the high cost comparing with the conventional LD. Furthermore, there is another fundamental problem. The electrical resistance is very high because it adopted lateral current injection. The gain may saturate because of heat, so that the maximum output is less than 10 μW. On the other hand, Crosnier et al. used 1D nanorib PC cavity to realize both current injection and light confinement. Relatively high output power of 80 μW can be achieved from the 1D cavity, but high threshold of 100 μA and large footpoint are weak points.

The PC laser we proposed and developed can deal with all the problems mentioned above, so it is possible to realize practical use. Furthermore, when circular resonators with different lasing wavelengths are placed alongside with an output waveguide as shown in Fig. 1.13, Wavelength Division Multiplexing (WDM) can be realized without a conventional optical multiplexer. Each laser can operate at a speed of above 50 Gbps due to small cavity volume [48]. So WDM with 20 channels results in bandwidth of 1 Tbps. Since the footprint of the proposed integrated device is expected to be 100×100 μm, the bandwidth density of 10 Pbps/cm^2 can be realized. This value is 1000 times higher than what Silicon photonics can achieve. The proposed PC laser has three unique points which are important in realizing WDM light source, and Table 1.1 shows the comparison of CirD laser with reported electrically driven PhC lasers. First of all, the wavelength tuning can be easily realized by changing the radius of the circular cavity. This feature enables to achieve WDM by using a simple structure as shown in Fig. 1.5. The second point is that it is possible to realize vertical current injection by using a special heterostructure which has been introduced in Refs. 30 and 31. The vertical current injection design reduces the footprint of the PC laser to the area of the cavity, so that the bandwidth density will be much higher than the one using LEAP laser and the 1D PhC nanorib cavity laser. Thirdly, the AlGaAs funnel area was used for current injection structure which is different from lateral current injection structure. Therefore, higher output power can be expected on the proposed structure due to smaller electrical resistance and thermal resistance.

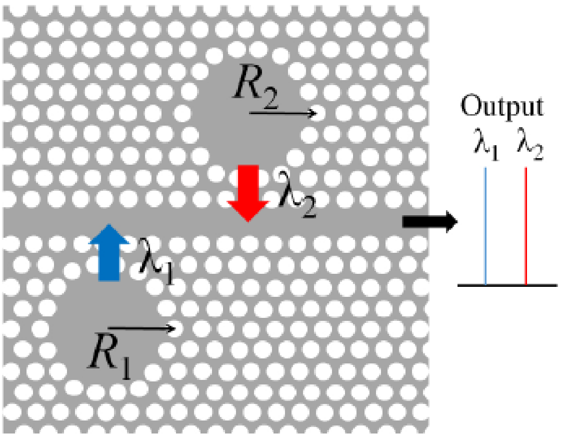

Fig. 1.13 Illustration of realizing WDM source using circular defect cavities with an output waveguide on a 2D PhC structure. Cavities with various radii generate lasers with different wavelengths. All lasers are able to couple to the line defect waveguide, so that WDM is realized [32].

Table 1.1 The comparison of CirD laser with reported electrically driven PhC lasers. Only CirD laser has proposal of realizing WDM.

	CirD laser	LEAP laser	1D nanorib laser	PCSEL
Electrical driven	Yes	Yes	Yes	Yes
Current direction	vertical	horizontal	vertical	vertical
Wavelength	~1.3μm	~1.5μm	~1.5μm	~0.9μm
Chip size*	$5\times5\mu m^2$	$10\times10\mu m^2$	$20\times5\mu m^2$	$200\times200\mu m^2$
WDM proposal	Yes	N/A	N/A	N/A

*Chip size doesn't contain the area of the electrode.

1.4 Problems and research objectives

For realizing the electrically driven CirD laser, there are several challenges should be faced. The first problem is that fine fabrication process should be developed for meeting the fabrication requirements. The fabrications of CirD lasers need microfabrication process with high accuracy. The most difficult step in the fabrication processes is the dry etching process which is used for fabricating air holes with fine shape on the epi-wafer. Therefore, the dry etching process used for fabricating CirD lasers should be well optimized. Another problem is that whether the designed structure of the CirD laser can lase should be examined.

For solving these problems, two objectives are researched and discussed in this study. The first objective is to optimize the dry etching process for the GaAs/AlGaAs-based epi-wafers. It is important to obtain deep etched air holes with vertical profile and regular shape on the epi-wafer, because the shape and profile of the air holes can affect the performance of the fabricated devices greatly. When the quality of the air holes is better, better performance of the devices can be expected. For obtaining the air holes on the epi-wafers, inductively coupled plasma (ICP) dry etching process is used in this study. The previous research in our group didn't optimize the dry etching process for the epi-wafer which is used for fabricating the electrically driven CirD laser. There are two difficulties in optimizing the dry etching process for this kind of epi-wafer. The first one is that deep etching with the depth larger than 1 μm is necessary. The epi-wafer usually has complex cross-sectional structure because it is designed for realizing an electrically driven device. The air holes should penetrate several layers which are served as the cladding layers, the core layer, and the contact layer. Another difficulty is that the dry etching process will apply on various materials. Different materials usually have different etching rate and mechanism for one dry etching recipe. However, for obtaining air holes with vertical profile, low selectivity of the dry etching process is expected. Therefore, strategy for solving this problem is that optimizing the dry etching process for each material used in the epi-wafer is firstly investigated. The dry etching of the epi-wafer is then optimized. Chapter3 and Chapter4 discussed the optimization of the dry etching process in details.

Chapter5 is focusing on the second objective which is to confirm that the design of the circular cavity can realize lasing operation. A PhC laser having a circular cavity was fabricated, and the optical properties were measured by using a optical measurement system. The structure of the PhC laser fabricated in this study is different from the electrically driven CirD laser, only properties under optical pump condition were examined. The electrodes were not deposited on the fabricated samples. Furthermore, the layers above the core layer were also removed for avoiding the absorption of excitation power. The AlGaAs layer was fully oxidized because of no requirement for electrical properties.

1.5 Organization of this dissertation

This dissertation addressed the optimization of dry etching process for fabricating PhC structure in a GaAs/AlGaAs-based epi-wafer and optical measurement of the PhC laser with a circular resonator.

Chapter 1 introduces the basics of 2D PhC structures and PBG. The design and the lasing mechanism of the proposed CirD laser has also been discussed.

Chapter 2 introduces the fabrication processes for fabricating the CirD laser.

Chapter 3 investigated dry etching of $Al_{0.8}Ga_{0.2}As$ and GaAs substrates for PhC fabrication using Cl_2, BCl_3, and CH_4 mixed gas.

Chapter 4 discussed the optimization of the GaAs/AlGaAs-based epi-wafers using a resist mask.

Chapter 5 presents the fabrication of CirD laser used for optical measurement. The characteristics of the optical properties are also discussed and analyzed.

Chapter 6 concludes the dissertation.

References

[1] C.-K. Lin, A. Tandon, K. Djordjev, S. Corzine, and M. Tan: ”High-Speed 985 nm Bottom-Emitting VCSEL Arrays for Chip-to-Chip Parallel Optical Interconnects,” IEEE Journal of Selected Topics in Quantum Electronics 13, 1332 (2007).

[2] P. Westbergh, J. Gustavsson, B. Kögel, Å. Haglund, A. Larsson, A. Mutig, A. Nadtochiy, D. Bimberg, and A. Joel: “40 Gbit/s error-free operation of oxide-confined 850 nm VCSEL,” Electronics Letters 46, 1014 (2010).

[3] T. Anan, N. Suzuki, K. Yashiki, K. Fukatsu, H. Hatakeyama, T. Akagawa, K. Tokutome, and M. Tsuji: “High-Speed 1.1-µm-Range InGaAs VCSELs,” OFC / NFOEC 2008, San Diego, CA, USA, paper OThS5 (2008).

[4] Y.-C Chang, C. Wang, and L. Coldren: “High-efficiency, high-speed VCSELs with 35 Gbit/s error-free operation,” Electronics Letters 43, 1022 (2007).

[5] P. B. Deotare, M. W. McCutcheon, I. W. Frank, M. Khan, and M. Lončar: “High quality factor photonic crystal nanobeam cavities,” Applied Physics Letters 94, 121106 (2009).

[6] K. Srinivasan, P. E. Barclay, and O. Painter: “Experimental demonstration of a high quality factor photonic crystal microcavity,” Applied Physics Letters 83, 1915 (2003).

[7] E. Yablonovitch: “Inhibited Spontaneous Emission in Solid-State Physics and Electronics,” Physical Review Letters 58, 2059 (1987).

[8] S. John: “Strong localization of photons in certain disordered dielectric superlattices,” Physical Review Letters 58, 2486 (1987).

[9] A. V. Dyogtyev, I. Sukhoivanov, R. D. L. Rue : “Photonic band-gap maps for different two dimensionally periodic photonic crystal structures,” Journal of Applied Physics 107, 013108 (2010).

[10] J. S. Hsu, M. R. Lee and K. F. Yarn: “Biaxial strain effects on optical characteristics of quantum well lasers,” Active and Passive Electronic Components 23, 237 (2001).

[11] M.J.L.Sangster and A.R.Q.Hussain: “The supercell method for calculating responses in defective lattices,” Physica B+C 131, 119 (1985).

[12] H. Park, J. Hwang, J. Huh, H. Ryu, and Y. Lee: “Nondegenerate monopole-mode two-dimensional photonic band gap laser,” Applied Physics Letters 79, 3032 (2001).

[13] H. Ryu, S. Kim, H. Park, J. Hwang, and Y. Lee: “Square-lattice photonic band-gap single-cell laser operating in the lowest-order whispering gallery mode,” Applied Physics Letters 80, 3883 (2002).

[14] H. Park, S. Kim, S. Kwon, Y.Ju, J. Yang, J. Baek, S. Kim, Y. Lee: “Electrically Driven Single-Cell photonic Crystal Laser,” Science 305, 1444 (2004).

[15] S. Matsuo, A. Shinya, T. Kakitsuka, K. Nozaki, T. Segawa, T. Sato, Y. Kawaguchi, and M. Notomi: “High-speed ultracompact buried heterostructure photonic-crystal laser

with 13 fJ of energy consumed per bit transmitted," Nature Photonics 4, 648 (2010).

[16] S. Matsuo, A. Shinya, C.-H. Chen, K. Nozaki, T. Sato, Y. Kawaguchi, H. Taniyama, and M. Notomi: "20-Gbit/s directly modulated photonic crystal nanocavity laser with ultra-low power consumption," Optics Express 19, 2242 (2011).

[17] S. Matsuo, K. Takeda, T. Sato, M. Notomi, A. Shinya, K. Nozaki, H. Taniyama, K. Hasebe, and T. Kakitsuka: "Room-temperature continuous-wave operation of lateral current injection wavelength-scale embedded active-region photonic-crystal laser," Optics Express 20, 3773 (2012).

[18] T. Sato, K. Takeda, A. Shinya, K. Nozaki, H. Taniyama, W. Kobaya-shi, K. Hasebe, T. Kakitsuka, M. Notomi, and S. Matsuo, "95°C CW Operation of InGaAlAs Multiple-quantum-well photonic-crystal Nanocavity Laser with Ultra-low Threshold Current," Proc. of the IEEE Photonics Conference, WF-2, Burlingame, California, USA, (2012).

[19] K. Hirose, Y. Liang, Y. Kurosaka, A. Watanabe, T. Sugiyama and S. Noda: "Watt-class high-power, high-beam-quality photonic-crystal lasers," Nature Photonics 8, 406 (2014).

[20] G. Crosnier, D. Sanchez, S. Bouchoule, P. Monnier, G. Beaudoin, I. Sagnes, R. Raj and F. Raineri: "Hybrid indium phosphide-on-silicon nanolaser diode," Nature Photonics 11, 297 (2017).

[21] D. M. Williams, K. M. Groom, B. J. Stevens, D. T. D. Childs, R. J. E. Taylor, S. Khamas, R. A. Hogg, N. Ikeda, and Y. Sugimoto: "Epitaxially Regrown GaAs-Based Photonic Crystal Surface-Emitting Laser," IEEE Photonics Technology Letters 24, 966 (2012).

[22] D. M. Williams, K. M. Groom, B. J. Stevens, D. T. D. Childs, R. J. E. Taylor, S. Khamas, R. A. Hogg, N. Ikeda, and Y. Sugimoto: "Optimisation of Coupling between Photonic Crystal and Active Elements in an Epitaxially Regrown GaAs Based Photonic Crystal Surface Emitting Laser," Japanese Journal of Applied Physics 51, 02BG05 (2012).

[23] H. Altug, D. Englund and J. Vuckovic: "Ultrafast Photonic crystal nanocavity laser," Nature Physics 2, 484 (2006).

[24] B. Ellis, M.A. Mayer, G. Shambat, T. Sarmiento, J. Harris, E. Haller, and J. Vučković: "Ultralow-threshold electrically pumped quantum-dot Photonic-crystal nanocavity laser," Nature Photonics 5, 297 (2011).

[25] O. Painter, R. K. Lee, Axel Scherer, A. Yariv, J. D. O'brien, P. D. Dapkus, and I. Kim: "Two-dimensional Photonic band-gap defect mode laser," Science 284, 1819 (1999).

[26] A. Tandaechanurat, S. Ishida, D. Guimard, M. Nomura, S. Iwamoto, and Y. Arakawa: "Lasing oscillation in a three-dimensional Photonic crystal nanocavity with a complete bandgap," Nature Photonics 5, 91 (2011).

[27] M Nomura, N Kumagai, S Iwamoto, Y Ota, Y Arakawa: "Laser oscillation in a strongly coupled single-quantum-dot–nanocavity system," Nature Physics 6, 279 (2010).

[28] K Nozaki, S Kita, T Baba: "Room temperature continuous wave operation and controlled spontaneous emission in ultrasmall photonic crystal nanolaser," Optics Express 15, 7506 (2007).

[29] Y. Gong, B. Ellis, G. Shambat, T. Sarmiento, J. S. Harris, and J. Vučković: "Nanobeam photonic crystal cavity quantum dot laser," Optics Express 18, 8781 (2010).

[30] M. Morifuji and Y. Nakaya: "Numerical Design of Photonic Crystal Cavity Structure with AlAs/AlO$_x$ Cladding Layers for Current-Driven Laser Diodes," Japanese Journal of Applied Physics 48, 112001 (2009).

[31] M. Morifuji, Y. Nakaya, T. Mitamura, and M. Kondow: "Novel Design of Current Driven Photonic Crystal Laser Diode," IEEE Photonics Technology Letters 21, 513, (2009).

[32] X. Zhang, T. Hino, S. Kasamatsu, S. Suga, E. He, Y. Xiong, M. Morifuji, H. Kajii, A. Maruta, M. Kondow: "1.3 μm lasing of circular defect cavity photonic crystal laser with an AlOx cladding layer," IEICE Electronics Express 14, 20170664 (2017).

[33] A. Nakagawa, S. Ishii, and T. Baba: "Photonic molecule laser composed of GaInAsP microdisks," Applied Physics Letters 86, 041112 (2005).

[34] T. Okabe, M. Morifuji, and M. Kondow: "Role of aluminum oxide cladding layers in heat transfer in a semiconductor slab with Photonic crystal," Japanese Journal of Applied Physics 53, 022701 (2014).

[35] Y. Xiong, T. Okada, X. Zhang, M. Morifuji, and M. Kondow: "Numerical Demonstration of the Feasibility of the Current Driven Photonic Crystal Laser Diode Used for Wavelength Division Multiplexing," the 43rd International Symposium on Compound Semiconductors, MoP-ISCS-030, Toyama, (2016).

[36] K. Takeda, T. Sato, T. Fujii, E. Kuramochi, M. Notomi, K. Hasebe, T. Kakitsuka, and S. Matsuo: "Heterogeneously integrated photonic-crystal lasers on silicon for on/off chip optical interconnects," Optics Express 22, 702 (2015).

[37] L. Dou, and A. R. Sebak: “3D FDTD method for arbitrary anisotropic materials,” Microwave and Optical Technology Letters 48, 2083 (2006).

[38] S. Lin, E. Schonbrun, and K. Crozier: “Optical manipulation with planar silicon microring resonators,” Nano letters 10, 2408 (2010).

[39] Q. Xu, D. Fattal, R. G. Beausoleil: “Silicon microring resonators with 1.5-μm radius,” Optics Express 16, 4309 (2008).

[40] J. Bai., J.Q. Wang, X.Y. Chen, J.Z. Jiang, H. Li, Y.S. Qiu, and Z.X. Qiang: “Characteristics of 45° photonic crystal ring resonators based on square-lattice silicon rods,” Optoelectronics Letters 6, 203 (2010).

[41] H. Ryu, M. Notomi, G. Kim and Y. Lee, “High quality-factor whispering-gallery mode in the photonic crystal hexagonal disk cavity”, Optics Express 12, 1708 (2004).

[42] C.J. Chang-Hasnain, J.P. Harbison, C.E. Zah, L.T. Florez, and N.C. Andreadakis: “Continuous wavelength tuning of two-electrode vertical cavity surface emitting lasers,” Electronics Letters 27, 1002 (1991).

[43] O. Dier, C. Reindl, A. Bachmann, C. Lauer, T. Lim, K. Kashani-Shirazi and M.-C. Amann: “Reduction of hetero-interface resistivity in n-type AlAsSb/GaSb distributed Bragg reflectors,” Semiconductor Science and Technology 23, 025018 (2008).

[44] M. Kneissl, M. Teepe, N. Miyashita, and N. M. Johnson: “Current-injection spiral-shaped microcavity disk laser diodes with unidirectional emission,” Applied Physics Letters 84, 2485 (2004).

[45] N. C. Frateschi and A. F. J. Levi: "Resonant modes and laser spectrum of microdisk lasers," Applied Physics Letters 66, 2932 (1995).

[46] S. L. McCall, A. F. J. Levi, R. E. Slusher, S. J. Pearton, and R. A. Logan: "Whispering-gallery mode microdisk lasers," Applied Physics Letters 60, 289 (1992).

[47] M. Chin, D. Y. Chu, and S. Ho: "Estimation of the spontaneous emission factor for microdisk lasers via the approximation of whispering gallery modes," Journal of Applied Physics 75, 3302 (1994).

[48] T. Nishimura, M. Morifuji, Kajii, M. Kondow: "Characteristic analysis of circular defect Photonic crystal laser using rate equation considering carrier diusion," The 64th JSAP Spring Meeting 15a-E205-4, Yokohama, (2017).

Chapter 2

Introduction of Fabrication Techniques

2.1 Introduction

For fabricating electrically driven CirD laser, 2D PhC structure is an essential part which should be fabricated on an epi-wafer with heterostructure. For obtaining 2D PhC structures on epi-wafers or substrates, several techniques are used. For example, the electron beam (EB) lithography process is used to draw the patterns on the resist [1-3]. The ICP dry etching process can etching air holes on the samples [4-6], and the scanning electron microscope (SEM) was used to take images of the morphology and profile of the etched air holes which is used to evaluate the quality of the air holes. These techniques are introduced as follows.

2.2 Electron beam lithography

Lithography is a technique used for forming a pattern on various substrates. Firstly, a film of photosensitive material (resist) is formed on the surface of a substrate. Then, the film is irradiated with energy rays such as ultraviolet (UV) light, X rays, and electron beams, to form a latent image with the designed pattern in the film. Finally, the latent image is developed using a developing solution to form patterns in the film. Lithography can be classified into two types. One type is that using light for transferring a geometric pattern from a photomask to the resist on the substrate. This is called as optical lithography or UV lithography. Another is that a focused beam of electrons is used to draw designed patterns on this resist by scanning. This is called as EB lithography. The procedures of lithography is illustrated in Fig. 2.1. The advantage of EB lithography is that it can draw designed patterns with high resolution. Because the diameters of the air holes in the PhC pattern used in this study is as small as ~200 nm, EB lithography is an effective tool used to form PhC patterns on the substrates.

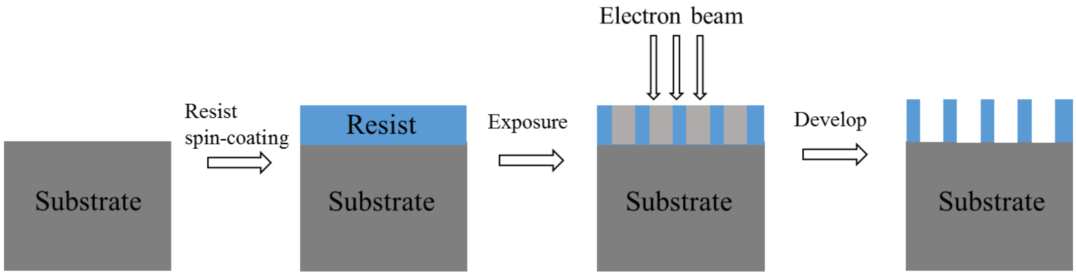

Fig. 2.1 The procedures of EB lithography. The PhC patterns are formed by irradiating electron beam on the resist.

The thickness of the photoresist affects the EB lithography, so the photoresist should be deposited on the film uniformly. Spin-coating is usually used to obtain the film of photoresist with uniform thickness on the wafers before EB lithography. The apparatus used to coat photoresist is called as spin coater. The device can rotate the substrate on a rotary table. The resist in a liquid state is dripped on the substrate firstly. Then a proper rotation speed is applied on the substrate. The resist liquid spreads to a film with uniform thickness by the centrifugal force. The thickness of the photoresist is dependent on the resist type and rotation speed. It is possible to obtain films of photoresist with similar thickness by using the same photoresist and rotation speed every time. In this study, ZEP520A was used as the photoresist [7,8], and Opticoat Spin Coater MIKASA MS-A 100 was used for forming resist films. The rotation speed is increased to 1000 rpm for 2s and rotated for 10s in the first step. Then, the rotation speed was increased to 6000 rpm for 5s and kept for 120s in sequence. The rotation stops in the last 5 seconds. The thickness of the photoresist using this procedure was about 350 nm.

After the spin coating process, baking is carried out for vaporizing the solvent of the resist immediately. It is performed on a hot plate at 180°C for 180s. After that, the sample is cooled on the metal plate to lower the temperature of the substrate.

The photoresist-coated samples were then placed in the EB lithography system to perform the EB lithography process. The patterns drawn in the EB lithography process is designed by CAD formerly. Then the patterns were drawn by the electron beams after setting the irradiation time and dose amount. The EB lithography process was carried out using an ELIONIX ELS-3700S system.

The dose amount is defined as the electron beam irradiation per unit area. The dose amount should be set to a value that no residual resist exists on the area irradiated by the electron beams after developing. The unit of dose amount is C/cm^2 or $\mu C/cm^2$. During the experiments, the pattern was drawn on a unit size of 100 μm × 100 μm. The scanning steps had 20000 dots ×20000 dots in this unit size, so the resolution of the EB irradiation was as small as 5 nm. The dose amount *D* of the system can be defined by the beam current *I*, irradiation time *T* per dot, and the area *A* using the equation as follows [9].

$$D = \frac{I \times T}{A}, \tag{2.1}$$

In this study, the beam current *I* was set as 25 pA, the dose time *T* was set as 1.1 μs/dot and the area *A* was set as 25 μm^2, obtaining the dose amount of 110 $\mu C/cm^2$ at the acceleration voltage of 30 kV.

The portion of the photoresist irradiated by electron beams can be dissolved (positive type) or solidified (negative type) by dipping in a developing solution. The positive type photoresist utilizes the mechanism that the molecular weight decreased by cleaving the main chain of the polymer and it becomes easy to dissolve in the developing solution. Since it is a reaction to decompose polymers, it has high sensitivity in EB lithography but low resistance in dry etching. On the contrary, the negative type photoresist is insoluble in the developing solution by bonding the polymers with each other after irradiated with electron beams. Even though the negative type has high resistance in dry etching process, the resolution deteriorates due to swelling during development. After immersing in the developing solution for a certain period of time, the developing solution should be washed away by dipping the samples in the rinse solution. Finally, the samples should be dried.

Positive type photoresist ZEP520A is used as mentioned previously, so ZED-N50 is used for the developer and ZMD-B for the rinse (both manufactured by ZEON Corporation). For dipping in the developer and rinse solutions, the samples are kept at 24°C in a thermostat. The photoresist was developed for 1 min and rinsed for 20s. Finally, the rinse liquid is vaporized by blowing nitrogen gas after rinsing.

2.3 Dry etching process

The etching methods roughly belonging to wet etching method using chemicals or dry etching method using gases [10]. Wet etching is performed by immersing the target sample in an etching solution according to the sample's characteristics [11-13]. This method has the advantage that the apparatus is inexpensive. A large amount of samples can be etched at once, and the productivity is high. However, when a micro-scale fabrication is demanded, it is very difficult to obtain isotropic etching because the etching rate for each direction is the same and it is impossible to control the etching rate for certain directions. Thus, the wet etching cannot be applied to fabricate fine features with size of micrometers or smaller dimensions. Therefore, application of a plasma process has been studied as an approach for etching features in small dimensions as an alternative to wet etching. Actually the dry etching process began to be introduced into the manufacture of integrated circuits from the early 1970s, and the effectiveness was confirmed. Etching process using such plasma is called as dry etching because plasma is not any liquid to be used in a conventional wet etching.

Dry etching [14-16] refers to the removal of material, typically a masked pattern of semiconductor material, by exposing the material to a bombardment of ions which are generated in the plasma. Plasma is a state of matter in which positive and negative charged particles that freely move and become electrically neutral. Positive and negative charged particles are mainly positive ions and electrons, respectively. They serve as reactive radicals used for etching.

Plasma is generated by applying an electric field on the etching gases. If a high frequency power supply is used instead of a direct current power supply, discharge can also be realized even if there is an insulator on the electrode, which is an important discharge mode in the plasma process. Radio Frequency (RF) discharge using frequencies of the radio wave band is widely used for generating plasma. The mainly used electro-magnetic wave of discharge modes are capacitively coupled plasma (CCP) and inductively coupled plasma (ICP). The formation of active species which is important for plasma process will be explained firstly, and the heating mechanism of the electrons, two discharge modes will be explained in sequence.

2.3.1 Chamber structure and etching principle

For obtaining the stable plasma source in the etching process, both RF-excited CCP and ICP have been widely used in many industrial applications [17], because it is relatively simple to construct instruments employed for these mothods. The ICP processing chamber was used in this study due to its ability of providing high plasma density and independent control of ion flux and ion energy [18,19]. The samples in this study are etched by ICP etching process using an ULVAC CE-300I system.

ICP

The structure of a typical chamber generating ICP is shown in Fig. 2.2. There are mainly two types of ICP coil shape. One is a cylindrical type which is wound along the outside the sidewall surface of a dielectric chamber. Another is a planar type which is spirally wound around the top or bottom surface of a chamber as shown in Fig. 2.2. The planar type is often used due to the simplicity to the apparatus, and the ICP etching instrument used in this study also adopts this construction. In addition, C_B is a blocking capacitor which can suppress the voltage fluctuation of the bulk plasma part and keep the electrode potential being stable. By applying an RF current through a coil convolved outside a dielectric chamber filled with low pressure gases, a temporally change of magnetic field is generated in the chamber. Then, an immediate induced electric field is then generated in the chamber. Finally, ionization collision occurs when the electric field becomes sufficiently strong. In this way, the number of electrons generated by ionization multiplies sufficiently, dielectric breakdown occurs and discharge occurs. This is the mechanism of generating ICP.

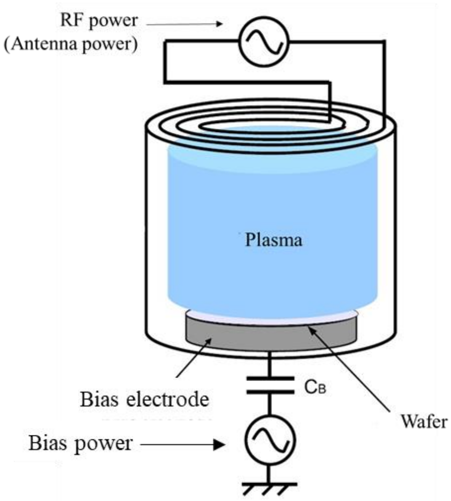

Fig. 2.2 A typical example apparatus of realizing ICP discharge mode. Two independent RF power sources are used and C_B is a blocking capacitor used to keep the electrode potential being stable. The antenna power adjusts the plasma density, and bias power accelerates the ions.

Dry etching is performed by irradiating the sample with plasma. The sample surface is exposed to the bombardment of various particles and then etched. The mechanism of etching can roughly be classified into physical etching and chemical etching [20]. The mechanisms of both etching types will be explained in the following context. The formation of self-bias, ion assist effect and side wall passivation, which are important for realizing the anisotropy etching, are also explained.

Active species

Various collisional reactions between electrons, ions, and source gas molecules occur in the generated plasma. The generation of active species is very important among these reactions in the plasma process. Active species refers to free radicals, ions, and so on. The process of generating active species is called as activation. The important activation in the plasma process is listed below. X and Y are neutral atoms in the following reaction equations. XY is a molecule, e is an electron, superscripts “*” and “+” represent an excited state, and a positive ion, respectively.

$$X + e \rightarrow X^* + e \text{ (Excitation reaction)}$$

$$X + e \rightarrow X^+ + 2e \text{ (Ionization reaction)}$$

$$XY + e \rightarrow XY^* + e \text{ (Excitation reaction)}$$

$$XY + e \rightarrow XY^+ + 2e \text{ (Ionization reaction)}$$

$$XY + e \rightarrow X + Y + e \text{ (Dissociation reaction)}$$

$$XY + e \rightarrow X^+ + Y + 2e \text{ (Ionization reaction and dissociation reaction)}$$

In this way, excitation, ionization, or dissociation reactions occurs because electrons with high energy (high temperature, high speed) colliding with atoms and molecules. Luminescence can be observed when the electrons on the outermost shell in the excited atoms (molecules) fall to the lower level, which causes plasma emission. In addition, when excited electrons do not fall to the lower level, atoms (molecules) become metastable. Because they can only lose their energy by collision with other particles, these atoms (molecules) act as an important role in the collision reactions.

Heating mechanism of the electrons

Within the frequency band of commonly used RF discharge, electrons can follow up the changes in the electric field, but ions cannot follow up. Therefore, only electrons follow the frequency and move intensely, while the ions move with respect to the average electric field. Furthermore, since the mass of electrons is much smaller than that of ions and neutral particles, the electron temperature is overwhelmingly higher than the temperature of ions and neutral particles. The electrons are accelerated by the RF electric field and the discharge is maintained by repeating collision with other particles and their ionization. Such a plasma is particularly called as a non-equilibrium plasma.

Chemical etching

In the plasma, atoms or molecules (radicals) which are electrically neutral and have high excited states are also generated. Most neutral particles adsorbed by the surface of the material cause a chemical reaction. Particularly, radicals containing halogen elements (F, Cl, Br, etc.) are remarkable in the reactions. If appropriate gases are selected, they react with the sample and then form volatile materials. When atoms are taken away from the sample, the sample is etched as a result. Since it is a chemical reaction process, the etching rate can be higher than the physical etching dominated by ions [21]. Most of the chemical etching is isotropic one although a high selectivity can be obtained in a limited case by utilizing chemical reactions.

Physical etching

Electrons can ionize neutrals and ions are generated in the plasma. When an electric field is applied, the ions having a high speed are irradiated to the sample surface. The atoms on the sample surface are knocked out due to the bombardment, and the sample is etched. Anisotropic etching can be realized when ions can be incident roughly vertically on the sample surface by the electric field. Especially, ions of a rare gas, such as Ar, have remarkable effects [22,23]. However, there is almost no difference of etching rate for different materials. The mask and the sample are etched in the same manner in physical etching. The etching rate is quite low, and damages appear easily on the surface due to physical collision. The interaction between the physical etching and the chemical etching also greatly affects the etching result concerned.

Formation of self-bias

The parameter known as DC self-bias voltage is an important “control knob” for the ion energy in the dry etching process [24]. Figure 2.3 shows a distribution of the average voltage induced for a typical ICP processing chamber. For ICP discharge, a dark area called as ion sheath is formed near the electrode and the light emitting area where the bulk plasma generates. In the bulk plasma region, the average potential is almost constant, but in the sheath the potential decreases as it approaches the electrode. The average potential on the ground electrode side is 0, which is different from the RF electrode side due to the presence of the blocking capacitor. Numbers of electrons reaching the electrode are overwhelmingly larger than ions because the electron temperature is higher than the ions. The reason has been explained in the section of heating mechanism. Then, electrons are accumulated on the electrode, and the potential abruptly drops near the RF electrode when the blocking capacitor is connected. Ions in the plasma have positive charge due to the active species. They are accelerated by this potential difference between the electrode and the bulk plasma. This potential difference V_{pp} is called a self-bias voltage. Because the ions are accelerated by the self-bias voltage, the higher the self-bias voltage is, the higher the proportion of ions in the plasma contributing to the etching process.

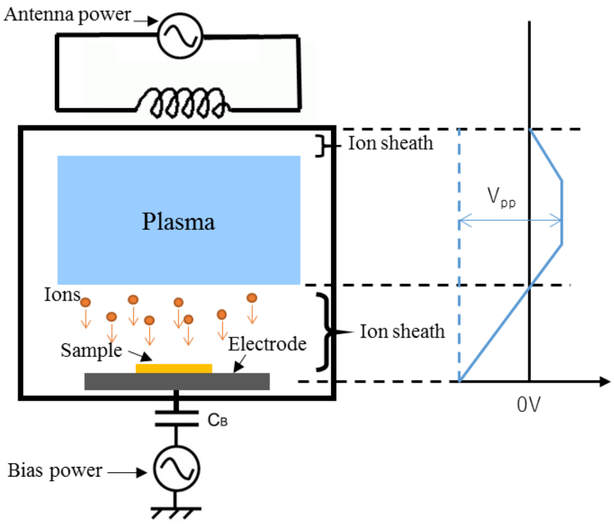

Fig. 2.3 Illustration of plasma location and electrical potential in a typical ICP chamber.

Ion assist effect

Chemical etching is dominated by chemical reactions, so it is necessary to provide an sufficient energy to disconnect the bond of the molecules and atoms in the sample. By providing ions with high energy, it is possible to dramatically increase the reaction rate of the sample and the radicals. In addition, with the collision of ions, possible evaporation of the reaction product from the sample can also be accelerated. Substantial anisotropic etching can be expected by applying these approaches. This is called ion assist effect. Etching utilizing this effect is called Reactive Ion Etching (RIE) dry etching process.

Side wall passivation

By using the ion assist effect, it is also possible to relatively suppress the etching rate in the lateral direction relatively. Etching in the lateral direction cannot be ignored because deep etching is one of the research objectives. The lateral etching is also called side etching. In order to realize anisotropic etching, the side wall passivation is important. The side wall passivation can be realized by forming a polymer film with etch products having low voltality as shown in Fig. 2.4 [25,26]. The formed polymer film can protect the side wall from being over etched.

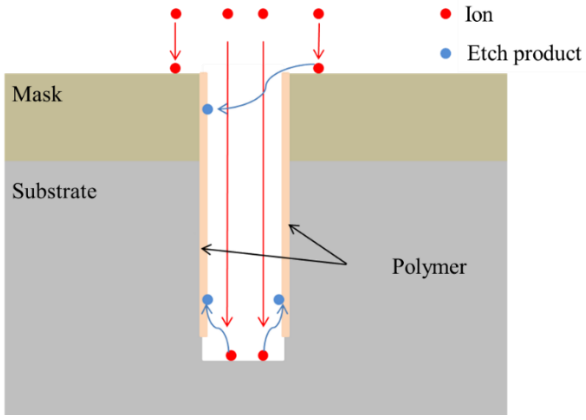

Fig. 2.4 Schematic illustration of side wall passivation effect. Etch products can form polymers on the side wall of the air holes.

2.3.2 Reactions in dry etching process

The generated plasma as described above undergoes various reactions in the etching chamber. The reactions related to the etching process concerned are listed below.

Reactions in the plasma

As mentioned above, in the plasma, active neutral atoms, molecular radicals and ions are generated, and an ion sheath is formed above the substrate. Plasma is kept in an electrically neutral state because the density of electrons and ions is almost equal, but ion sheath is formed on solid surfaces such as the substrate, the electrode or the chamber wall. As a result, although electrons are decelerated or repelled, the ions are accelerated, and the ions are excessive in the ion sheath and the electrically neutral state is broken.

Electrically neutral particles such as gas molecules, atoms or molecular radicals, near the surface are not affected by the ion sheath, so that they are isotropically incident to the surface while maintaining the thermal velocity. On the other hand, the ions are accelerated by the electric field in the ion sheath. The accumulated kinetic energy on the ions is obtained by the potential difference in the ion sheath. Because the pressure in the ion sheath is very low, so the incident ions have few collisions with the gas molecules. Therefore, ions are incident almost vertically to the surface. Atoms, molecular radicals and ions disappear mainly due to recombination at the chamber wall, recombination on the electrode surface and etching reaction at the substrate surface. Meanwhile, negative ions are trapped back and confined in the chamber due to the ion sheath on the substrate surface, on the electrode and chamber wall. Eventually, recombination with positive ions in the plasma and the detachment of electrons caused by collision with high-speed electrons are the main annihilation processes. The role of the reaction products is also important. The reaction products can deposit accumulates on the substrate surface, the bottom and side wall of the features. This process can also affect the etching rate and shape of the etched features.

Reactions on the chamber wall and the electrode surface

The chamber wall and the electrode surface under low pressure are the main fields where the annihilation of atoms, molecular radicals and ions in the plasma happen. Recombination and deposition of radicals on the surface, ion neutralization reactions, have a great influence on the composition and density of reactive species in the plasma. In a low-pressure/high-density plasma source, since the high frequency is electromagnetically coupled with the plasma through a dielectric such as quartz (SiO_2) or alumina (Al_2O_3) from the outside of the chamber, ions are accelerated to the walls, and generation of impurities by sputtering of the inner wall of the dielectric is also substantial.

Reaction on the surface of the substrate to be etched

On the surface of the substrate, various interactions of incident neutral atoms, molecular radicals, reactive gas molecules, ions and substrate atoms happen. Then substrate atoms are detached from the surface and etching progresses. The reactions of dry etching progress on the surface are (1) chemical etching with neutral reactive active species, (2) physical etching by ions, (3) ion assisted reaction by ions and neutral active species, (4) passivation progress on the side wall. The reactions (1) to (4) have been explained above.

Various materials involved in the dry etching processes in this study. For example, when the SiN_x masks are etched, C_3F_8 gas is used to provide the plasma chemistry. Table 2.1 shows the main reactions during the dry etching of SiN_x masks. These reactions are written by referring the reactions of SiO_2 and C_3F_8 gas in the dry etching process described in Ref. 28.

Table 2.1 The main reactions between SiN_x and C_3F_8 plasma chemistry [27]

Reactions	Incident species	Surface	Process
(1) $Si_3\text{-}N_4 \rightarrow 3Si(g)+4N(g)+Si_3N_4$	CF_x^+	Si_3N_4	Physical sputtering
(2) $4F(g)+Si_3N_4(s)$ $\rightarrow Si\text{-}F_4(g)+N_2(g)+Si_3N_4$	F	Si_3N_4	Chemical etching
(3) $CF_x^+(g) \rightarrow$ polymer(s)	CF_x^+	Si_3N_4	Polymer deposition
(4) $CF_x \rightarrow$ polymer	CF_x	Si_3N_4	Polymer deposition
(5) polymer $\rightarrow$ sputtering of polymer	CF_x^+	Polymer	Physical sputtering
(6) F(g)+polymer(s) $\rightarrow$ etching of polymer	F	Polymer	Chemical etching

g: gas phase, s: solid phase

The etching reactions of SiN_x is mainly induced by chemical etching with F and physical sputtering by CF_x^+. The etch products of CF_x^+ and polymers can also deposit on the side wall of the micropatterns.

When fabricating the CirD laser, dry etching of GaAs/AlGaAs-based heterostrucutre is an essential step. For etching GaAs or AlGaAs-based materials, a $Cl_2/BCl_3/CH_4$ gas mixture was used to provide the plasma chemistry for obtaining anisotropically etching with high aspect ratio. Cl_2 is the main etching agent and BCl_3 and react with the etch product AlO_x. The combination of Cl_2 and BCl_3 is widely used to etch GaAs or AlGaAs based materials. The effect of reducing AlO_x which is caused by BCl_3 make the etching process being fast. CH_4 can deposit polymer on the side wall of the micropatterns with etch product. The main reactions are shown in Table 2.2.

Table 2.2 The main reactions for GaAs or AlGaAs based materials [29].

Reactions	Incident species	Surface	Process
(1) Al-Ga-As → Al(g)+Ga(g)+As(g)+Al-Ga-As	Cl_x^+, B_x^+, BCl_x^+, C_x^+, CH_x^+	AlGaAs	Physical sputtering
(2) Al-Ga-As+Cl(g) → $AlCl_3$(g)+$GaCl_3$(g)+$AsCl_3$(g)+Al-Ga-As	Cl	AlGaAs	Chemical etching
(3) BCl_x^+(g) → polymer(s)	BCl_x	AlGaAs or polymer	Deposition
(4) BCl_x → polymer	BCl_x	AlGaAs or polymer	Deposition
(5) polymer → sputtering of polymer	Cl_x^+, B_x^+, BCl_x^+, C_x^+, CH_x^+	Polymer	Physical sputtering
(6) Cl(g)+polymer(s) → etching of polymer	Cl	Polymer	Chemical etching
(7) Al_2O_3 → Al(g)+O(g)+Al_2O_3	Cl_x^+, B_x^+, BCl_x^+, C_x^+, CH_x^+	Al_2O_3	Physical sputtering
(8) Al_2O_3 + BCl_x → BOCl+Al(g)+Al_2O_3	BCl_x	Al_2O_3	Chemical etching

g: gas phase, s: solid phase

Transportation and reactions of particles in fine features

Ions and neutral reactive species enter the bottom of the micro-patterned hole etched through the surface of the substrate. The etching progresses are induced by the ion assist reaction have been described above. Neutral active species are incident mainly to the sidewalls. The reaction on the bulk surface is basically based on reactions mentioned above, but the flux of ions and neutral active species incident to the bottom and sidewalls in the pattern are greatly different from the bulk surface for etching the micropatterns. First, the flux of incident particles to the substrate surface or the bottom of the micropatterns or side wall from the plasma is generally smaller as compared with the flux incident to the bulk surface. The transportation of the particles in the micropatterns is related to the microscopic uniformity of the etching.

2.3.3 Parameters in dry etching process

Important parameters used to control the dry etching process are listed below.

Discharge power

Discharge power affects the density of plasma (i.e. electrons or ions). Since the generation rate of radicals increases in proportion to the electron density, the density of the radical also increases with the antenna power. The discharge powers are supplied from the RF power for CCP and the Antenna power for ICP.

Process pressure

The process pressure is the pressure during discharge, which greatly affects the mean free path of ions and the plasma density. It is an important parameter especially when anisotropic etching is performed. Ions are accelerated by the electric field in the sheath area having a thickness of about several millimeters. If the ions collide with the neutral molecules during the acceleration, then scattering occurs. In such a case, the ideally vertical injection cannot be obtained. For this reason, it is necessary to set the mean free path close to the sheath thickness, which requires a process pressure of about 1 Pa or less. Since the number of molecules decreases when the pressure is lower, the plasma density also decreases. On the other hand, when the process pressure is increased, the plasma density increases even if the discharge power is constant. If the process pressure is raised too much, then the energy required to maintain the discharge significantly decreases, the electron temperature decreases and the plasma density decreases.

Gas composition

The gas composition is an important parameter which determines etching characteristics. Basically, a gas that produces a reaction product having a high vapor pressure is selected as the main etching gas. In this study, a fluorocarbon-based gas, C_3F_8 is used for etching of Si-based materials. This is because the vapor pressure of SiF_x as a reaction product is relatively high. For etching GaAs, Cl-based gases are used, such as Cl_2 and BCl_3. This is because the vapor pressure of $GaCl_x$ which is a reaction product is substantially high. In addition, various gases are used for various purposes. For example, the addition of CH_4 can improve the physical etching effect, promoting ionization, and stabilizing the plasma.

Bias power

It is also an important parameter to control the ion assist amount and the damage of the etched surface in anisotropic etching by changing the energy of ions. For the CCP case, RF power directly affects the bias power and cannot be controlled independently. In a high density plasma etching apparatus using a discharge method of ICP, it is possible to adjust the V_{pp} by changing the bias power.

2.4 Scanning electron microscope (SEM)

SEM with a high resolution is used to observe the surface morphology and depth profile of the fabricated air holes. It is important to evaluate the quality of the etched air holes. SEM is a type of electron microscope that produces images of a sample by scanning the surface with a focused beam of electrons. When the electron beam scans the surface of the samples, secondary electrons emitted by atoms generate which is excited by the electron beam. By amplifying the detected secondary electrons and sending the signals to the monitor, an enlarged image of the scanned area is obtained. The contrast of the obtained SEM image corresponds to the amount of secondary electrons entering the secondary electron detector. Factors affecting the amount of generated secondary electrons include gradient effect, edge effect, acceleration voltage effect, atomic number effect, and charging effect. The SEM used in this study was a Hitachi S-4300 at Katayama Laboratory.

References

[1] M. Kondow, T. Kawano, and H. Momose: “Selective Oxidation of AlGaAs for Photonic Crystal Laser,” Japanese Journal of Applied Physics 48, 050202 (2009).

[2] M. A.McCord, J. R. Michael: “SPIE Handbook of Microlithography, Micromachining and Microfabrication,” SPIE Press, Washington (2000).

[3] G. Wiederrecht: “Handbook of Nanofabrication,” Academic Press, Amsterdam (2009).

[4] K. Michael: “Etching in Microsystem Technology,” John Wiley & Son Ltd., New York (1999).

[5] S. Inoue, K. Kajikawa, and Y. Aoyagi: “Dry-etching method for fabricating photonic-crystal waveguides in nonlinear-optical polymers,” Applied Physics Letters 82, 2966 (2003)

[6] K. Inoshita and T. Baba: “Fabrication of GaInAsP/InP Photonic Crystal Lasers by ICP Etching and Control of Resonant Mode in Point and Line Composite Defects,” IEEE Journal of Selected Topics in Quantum Electronics 9,1347 (2003).

[7] B. P. Downey, D. J. Meyer, R. Bass, D. S. Katzer, and S. C. Binari: “Thermally reflowed ZEP 520A for gate length reduction and profile rounding in T-gate fabrication,” Journal of Vacuum Science & Technology B, Nanotechnology and Microelectronics:

Materials, Processing, Measurement, and Phenomena 30, 051603 (2012).

[8] R. Kirchner, V.A. Guzenko, I. Vartiainen, N. Chidambaram, and H.Schift: "ZEP520A -- A resist for electron-beam grayscale lithography and thermal reflow, " Microelectronic Engineering 156, 71 (2016).

[9] N. W. Parker; A. D. Brodie; J. H. McCoy: "High-throughput NGL electron-beam direct-write lithography system," SPIE Proceedings 3997, 713 (2000).

[10] S. J. Pearton, C. R. Abernathy, F. Ren, J. R. Lothian, P. W. Wisk, and A. Katz: "Dry and wet etching characteristics of InN, AlN, and GaN deposited by electron cyclotron resonance metalorganic molecular beam epitaxy," Journal of Vacuum Science & Technology A: Vacuum, Surfaces, and Films 11, 1772 (1993).

[11] B. Gayral, J. M. Gérard, A. Lemaître, C. Dupuis, L. Manin, and J. L. Pelouard: "High-Q wet-etched GaAs microdisks containing InAs quantum boxes," Applied Physics Letters 75, 1908 (1999).

[12] M. S. Minsky, M. White, and E. L. Hu: "Room-temperature photoenhanced wet etching of GaN," Applied Physics Letters 68, 1531 (1996).

[13] D. V. Podlesnik, H. H. Gilgen, and R. M. Osgood Jr.: "Deep-ultraviolet induced wet etching of GaAs," Applied Physics Letters 45, 563 (1984).

[14] M. W. Geis, G. A. Lincoln, N. Efremow, and W. J. Piacentini: "A novel anisotropic dry etching technique," Journal of Vacuum Science and Technology 19, 1390 (1981).

[15] K. Hikosaka, T. Mimura and K. Joshin: "Selective Dry Etching of AlGaAs-GaAs

Heterojunction," Japanese Journal of Applied Physics 20 (1981).

[16] P. Brewer, S. Halle, and R. M. Osgood Jr.: "Photon-assisted dry etching of GaAs," Applied Physics Letters 45, 475 (1984).

[17] Y. Sakamoto, S. Maeno, N. Tsubouchi, T. Kasuya and M. Wada: "Comparison of Plasma Parameters in CCP and ICP Processes Appropriate for Carbon Nanotube Growth," Journal of Plasma and Fusion Research 8, 587 (2009).

[18] J. W. Lee, M. W. Devre, B. H. Reelfs, D. Johnson, and J. N. Sasserath: "Advanced selective dry etching of GaAs/AlGaAs in high density inductively coupled plasmas," Journal of Vacuum Science & Technology A: Vacuum, Surfaces, and Films 18, 1220 (2000).

[19] R. J. Shul, G. B. McClellan, R. D. Briggs, and D. J. Rieger: "High-density plasma etching of compound semiconductors," Journal of Vacuum Science & Technology A: Vacuum, Surfaces, and Films 15, 633 (1997).

[20] C. Steinbrüchel: "Universal energy dependence of physical and ion-enhanced chemical etch yields at low ion energy," Applied Physics Letters 55, 1960 (1989).

[21] S. A. Smith, C. A. Wolden, M. D. Bremser, A. D. Hanser, and R. F. Davis: "High rate and selective etching of GaN, AlGaN, and AlN using an inductively coupled plasma," Applied Physics Letters 71, 3631 (1997).

[22] Y. B. Hahn, J. W. Lee, G. A. Vawter, R. J. Shul, C. R. Abernathy, D. C. Hays, E. S. Lambers, and S. J. Pearton: "Reactive ion beam etching of GaAs and related compounds in an inductively coupled plasma of Cl_2–$ArCl_2$–Ar mixture," Journal of Vacuum Science

& Technology B 17, 366 (1999).

[23] H. Lee, D. B. Oberman, and J. S. Harris Jr.: "Reactive ion etching of GaN using CHF_3/Ar and C_2ClF_5/Ar plasmas," Applied Physics Letters 67, 1754 (1995).

[24] A. J. van Roosmalen, W. G. M. van den Hoek, and H. Kalter: "Electrical properties of planar rf discharges for dry etching," Journal of Applied Physics 58, 653 (1985).

[25] M. Volatier, D. Duchesne, R. Morandotti, R. Ares, and V. Aimez: "Extremely high aspect ratio GaAs and GaAs/AlGaAs nanowaveguides fabricated using chlorine ICP etching with N_2-promoted passivation," Nanotechnology 21, 134014 (2010).

[26] M. A. Blauw, T. Zijlstra, and E. van der Drift: "Balancing the etching and passivation in time-multiplexed deep dry etching of silicon," Journal of Vacuum Science & Technology B, Nanotechnology and Microelectronics: Materials, Processing, Measurement, and Phenomena 19, 2930 (2001).

[27] Y. Imada, Master's Thesis, Kondow Laboratory, Graduate School of Engineering, Osaka University (2015).

[28] H. Fukumoto, K. Eriguchi, and K. Ono: "Effects of Mask Pattern Geometry on Plasma Etching Profiles," Japanese Journal of Applied Physics 48, 096001 (2009).

[29] M. Mochiduki, Master's Thesis, Kondow Laboratory, Graduate School of Engineering, Osaka University (2012).

Chapter 3

Dry Etching of AlGaAs and GaAs

3.1 Dry etching of AlGaAs

AlGaAs/GaAs systems have been studied for the fabrication of PhC structures, since Al-rich AlGaAs, typically with an Al concentration greater 80%, offers extensive choices for device fabrication [1]. Al-rich AlGaAs itself has a certain refractive-index contrast to GaAs. In addition, selective etching or oxidation enables a much greater contrast, and also provides an insulating property, while preserving the mechanical strength [2-4]. The previous researches in Kondow Laboratory reported a PhC structure with air holes deeper than 1.5 μm and a diameter of 120 nm fabricated using SiO_2 as the mask layer [5]. In this case, the gas flow rate and process pressure were carefully adjusted to achieve greater etching depth. However, the air hole arrays we achieved had a diameter smaller than the nominal 200 nm and a shape approximately like a reverse cone, that's mainly because of mask retardation [6]. The strong contribution of physical etching induced sharpening of the air hole bottom. On the basis of the above, SiN_x was substituted with SiO_2 for the mask layer in this study. The ICP deep dry etching of Al-rich $Al_{0.8}Ga_{0.2}As$ was investigated to expand the air-hole diameter and improving the air-hole shape of the fabricated PhC structure.

3.1.1 Experimental procedure

Figure 3.1 shows the layer structure of the sample studied in this chapter. Etching of the 3-μm-thick $Al_{0.8}Ga_{0.2}As$ samples was carried out. A GaAs cap layer with thickness of 30 nm was used to cover and protect $Al_{0.8}Ga_{0.2}As$. They were grown on a GaAs substrate by molecular beam epitaxy.

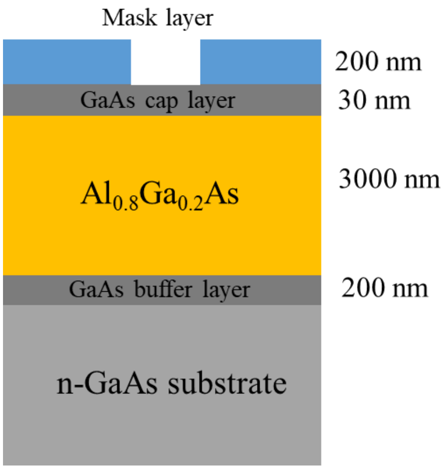

Fig. 3.1 Layer structure of the sample studied. The 3-μm-thick $Al_{0.8}Ga_{0.2}As$ layer was epitaxially grown on a GaAs substrate. A GaAs cap layer with thickness of 30 nm was used to cover and protect $Al_{0.8}Ga_{0.2}As$.

The fabricating procedures is illustrated in Fig. 3.2. On the samples, 200-nm-thick SiO_2 or SiN_x was deposited by sputtering. Then, a 350-nm-thick resist was spin-coated. The mask layer was etched with C_3F_8 gas at a flow rate of 17 sccm [7]. The bias power was 100W for both two kinds of mask layers. The antenna power during the mask etching process was 0 W for SiO_2 and 350 W for SiN_x. The mask layer was used as the rigid mask for the subsequent etching of the PhC structure. The air holes were arranged into a triangular pattern with a lattice constant of 300 nm and nominal diameter of 200 nm. A $Cl_2/BCl_3/CH_4$ gas mixture at fixed flow rates at 12, 18 and 3 sccm was used. The process pressure was controlled with a variable valve introduced between the etching chamber and the vacuum pump of the system. The antenna power of 300 W and a constant self-bias voltage of 240 V were used for the realization of a highly regular PhC structure. Finally, the samples underwent the RIE process again with C_3F_8 gas at a flow rate of 15 sccm to remove the mask layer completely. The fabricated etched structure was investigated by SEM.

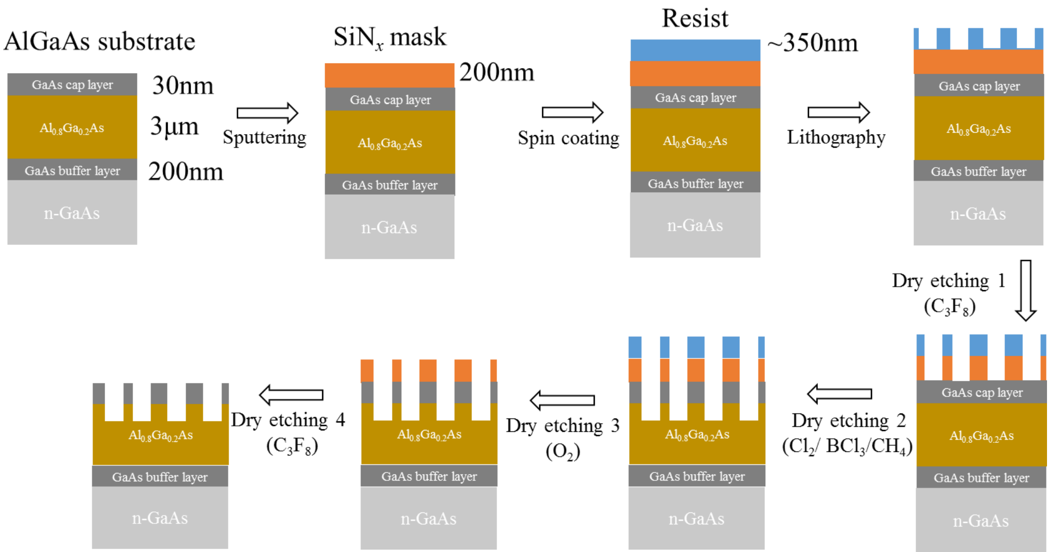

Fig. 3.2 Fabricating procedures for etching AlGaAs substrate.

3.1.2 The effect of using SiN_x and SiO_2 masks

To overcome the degradation of the mask verticality, antenna power was applied on the samples during the mask etching process. Figure 3.3 shows the (a) cross-sectional and (b) plan view SEM images of the sample with a SiN_x mask layer after mask etching with antenna power. The inset of Fig. 3.3(a) shows the cross sectional SEM image of the sample etched without antenna power. As shown in Fig. 3.3(a) and the inset, the air holes in the mask layer have bottoms with the diameter of 180 nm when antenna power was applied. Meanwhile, the diameter shrank to 160 nm when antenna power was not applied. It is obvious that the bottom of the air holes in the mask layer was expanded when antenna power was applied. The improvement of the mask verticality should be attributed to the isotropic etching caused by the high plasma density resulting from the antenna power [8,9].

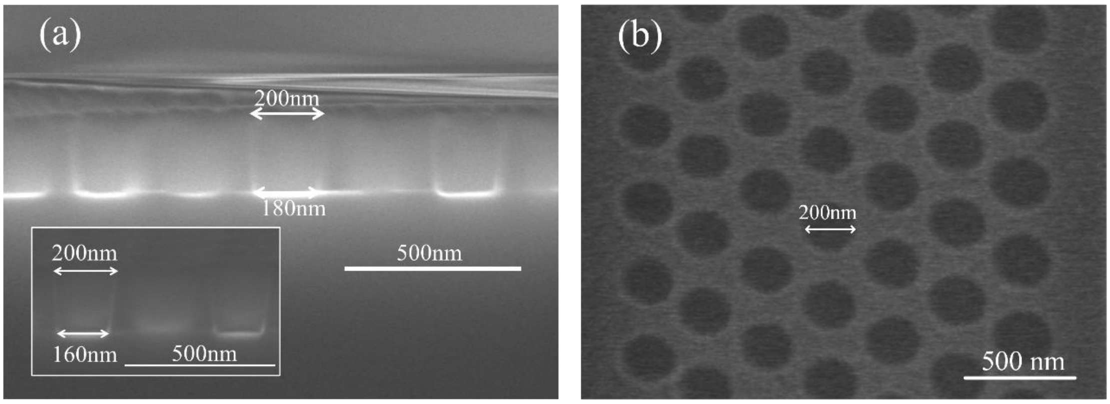

Fig. 3.3 (a) Cross-sectional and (b) plan-view SEM images of the sample using SiN_x mask etched by 350 W antenna power. The inset shows the cross-sectional SEM image of the sample etched without antenna power. [10]

As shown in Fig. 3.4, the physical etching effect, which can be modified by varying the bias power and process pressure, is based on physical bombardment with ions during the dry etching process. However, too great of a physical etching effect during the whole etching process may sharpen the bottom of the air holes and limit further deep etching. On the other hand, antenna power plays an important role in dissociating mixed gas molecules into reactive radicals and ionic species, and thus in increasing the plasma density and chemical etching effect. The chemical etching effect causes the etching process to be isotropic and the vertical profile of the air holes to be round. To achieve the air hole arrays with high verticality, the correct balance between physical etching effect and chemical etching effects is necessary.

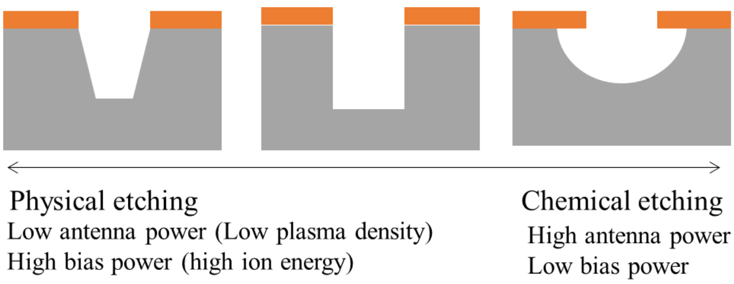

Fig. 3.4 Schematic diagrams of a variety of profiles influenced by physical etching and chemical etching effect.

Figures 3.5(a)-(d) show the SEM images of vertical profiles of the samples after ICP deep dry etching. The material of the mask layer and parameters used in the deep dry etching process of the samples shown in Fig. 3.5 are listed in Table 3.1. The self-bias voltage can be treated as being constant because it varies less than 5%, especially under the higher process pressure condition. This result implies that the mechanism of ICP etching differs when different mask layers are used. The variation of the etching mechanism should be attributed to the charge up on the sidewall surface of the mask layer.

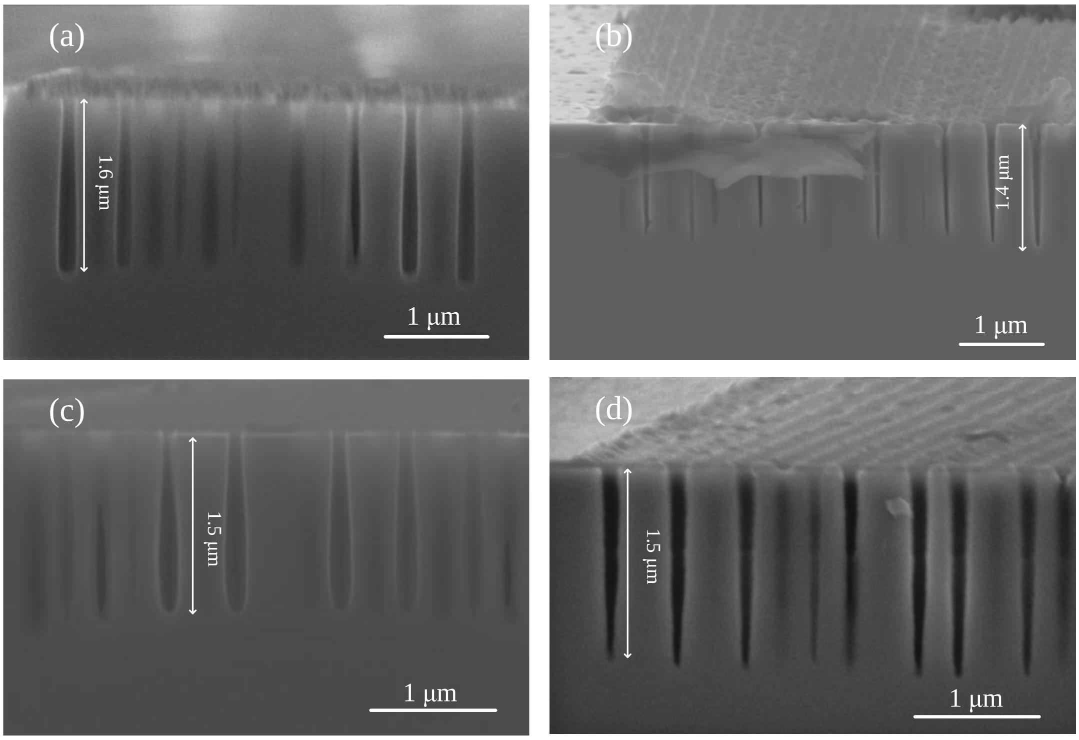

Fig. 3.5 SEM images of vertical profiles for the PhC structure with air holes fabricated using various mask layers. (a) and (c) samples using SiN_x as the mask layer, (b) (d) samples using SiO_2 as the mask layer. [10]

Insulators, such as SiO_2 and SiN_x, can immobilize the charge up on the surface of the material. The surface of the mask layer containing a lot of charge up becomes essential because there exists a high density plasma during the ICP etching process [9]. Furthermore, SiN_x can be charged more easily than the case of SiO_2 owing to its higher dielectric constant. As shown in Fig. 3.6, when SiN_x was used as the mask layer, the trajectories of the incident positive ions were bent owing to the influence of the electric field arising from the high-density charge up. To overcome the effect of charge up, one of the solutions is to increase the ion energy. The bias power may need to be increased to raise the ion energy so that the bending of the trajectories can be ignored.

Table 3.1 Parameters of ICP etching process for the samples shown in Fig. 3.13. [10]

Figure label	Mask layer	Antenna power (W)	Process-pressure (Pa)	Bias power (W)	Self-bias Voltage (V)
a	SiN_x	300	0.4	22	240
b	SiO_2	300	0.6	20	245
c	SiN_x	300	0.4	23	241
d	SiO_2	300	0.6	20	243

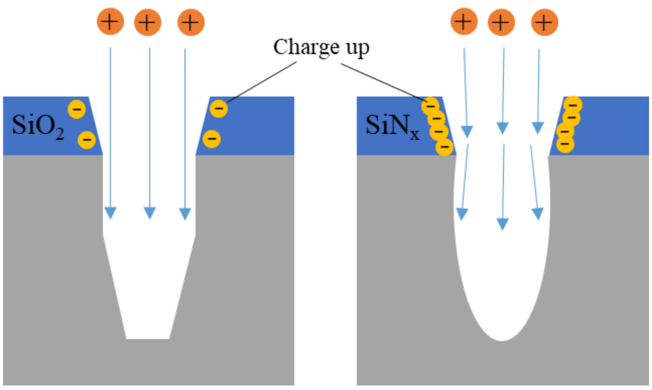

Fig. 3.6 Schematic illustration of the effect of charge up, which alters the trajectories of the incident positive ions.

To alleviate the effect caused by mask retardation, the thickness of the SiN_x mask layer was then reduced to 80 nm, as shown in Fig. 3.7, so that the diameter of the air holes can be further expanded. Furthermore, decreasing the thickness of the SiN_x mask layer also simultaneously reduced the charge up and thus eliminated the effect on the trajectories of the incident ions.

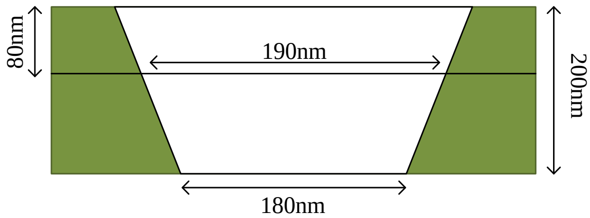

Fig. 3.7 Schematic illustration of effect of reducing the thickness of the SiN_x mask layer. [10]

Figure. 3.8 shows the resulting PhC structure when using the thin mask layer under the optimized parameters listed in Table 3.2. The fabricated PhC structure has air holes with a depth of 1.7 μm and a diameter of 190 nm. The improvement of the round shape at the bottom of the air hole and increased etching depth can be observed. As a result of using the thin mask layer with the thickness of 80 nm, a PhC structure having air holes of highly regular shape was successfully fabricated.

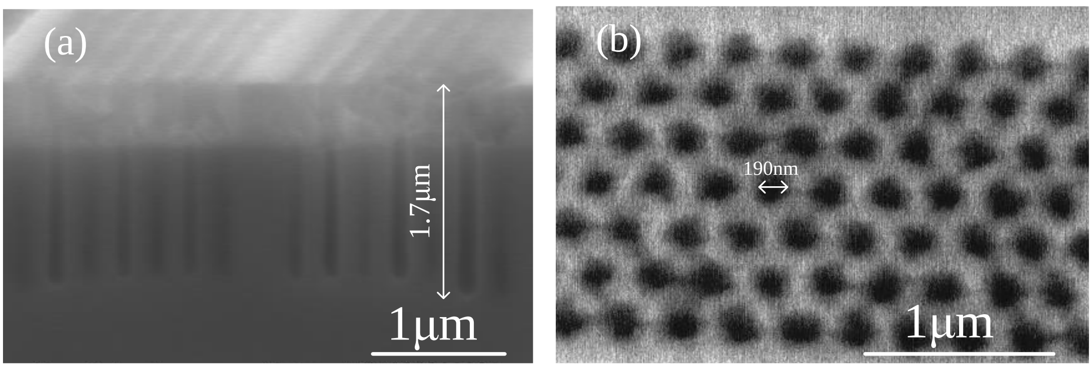

Fig. 3.8 (a) Cross-sectional and (b) plan-view SEM images of PhC structure formed with $Al_{0.8}Ga_{0.2}As$. The air-hole depth is 1.7 μm and the diameter is 190 nm. [10]

3.2 Dry etching of GaAs

In Section 3.1, the optimization of the etching process for AlGaAs is mainly focused on the influence of different mask materials on the etching profiles. From this section, the dry etching process of GaAs substrate is discussed. These experiments not only concern about the profile and the depth of the air holes, but also concern about the radius of the air holes. For confining the cavity resonant modes around 1.3 μm, the parameters of PhC structure, such as lattice constant *a* and radius of air holes *r*, should be well designed and precisely controlled, because PBG is related to the filling ratio expressed as *r/a* [11]. As discussed in Section 1.2.3, the *r/a* should be larger than 0.27 when *a* is 340 nm. For tolerating fabricating errors during the fabrication processes, the target *r/a* is set to be higher than 0.3 in these experiments in this section.

Table 3.2 Parameters used in the fabrication of the sample shown in Fig. 2.16 for different process durations. [10]

	SiN_x mask etching	ICP dry etching	Remove mask etching
Process pressure (Pa)	0.5	0.4	2.00
Antenna power (W)	350	300	0
Bias power (W)	200	22	20
Etching time (s)	30	900	1500

During the EB lithography process, electron scattering happened as shown in Fig. 3.9. Forward scattering broadened the beam when the electrons entered the resist. Some fraction of those electrons would eventually undergo enough large angle collisions to re-emerge into the resist when they reach the surface of SiN_x mask. Then backscattering was generated. Thus, real radius of the air holes r_r became larger than the set value in computer-aided design (CAD) software r_c. Furthermore, if the required *r/a* is quite high, large *r* compresses the space between each air holes. Finally, the PhC patterns might be destroyed because the air holes would merge together. So optimization of r_c is necessary for achieving the required *r/a*. In this section, GaAs substrate was used to study the EB lithography process, and the profiles of the air holes in the GaAs substrate were also optimized by adjusting the parameters of the dry etching process.

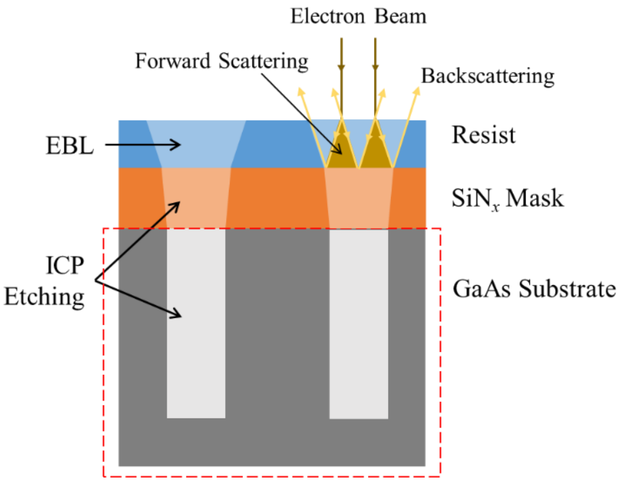

Fig. 3.9 Forward and backscattering of electrons in the resist and SiN_x mask leading to beam broadening and proximity effects.

3.2.1 EB lithography and mask etching

Figure 3.10 shows the SEM images of the patterns drawn on the resist after EB lithography process. *a* observed from the images is 332 nm. The radius of the air holes on the surface of the resist are 112 and 116 nm when r_c were set as 75 and 80 nm; and the space left between the air holes are 106 nm and 96 nm, respectively. As expected, r_r of both samples are much larger than r_c. This is attributed to electron scattering in EB lithography process, and leading *r/a* on the resist to be 0.337 and 0.349 when r_c were set as 75 and 80 nm, respectively. Regular circles separating with each other well were both achieve as shown in Fig. 3.10 even though the space left between the air holes are only about 100 nm. It means that EB lithography process was still successful under such severe conditions. On the other hand, if r_c is larger than 80 nm and used in the EB lithography process, the resist mask after developing is easily deformed due to the narrow space between the air holes according previous experimental experiences.

Furthermore, due to the forward and backscattering of electrons, the features where are dense, such as the area marked in Fig. 3.10(a) and 3.10(b), receive more accumulated energy from the electrons, while the features where are sparse receive less energy. This is so called proximity effect [12] and that’s why the air holes in the central part in PhC structures have bigger diameter while the air holes at the outer edges have smaller diameter as shown in Fig. 3.10(a) and 3.10(b).

However, proximity effect doesn't affect the lattice constant *a* which is stable in the whole PhC structures for both samples.

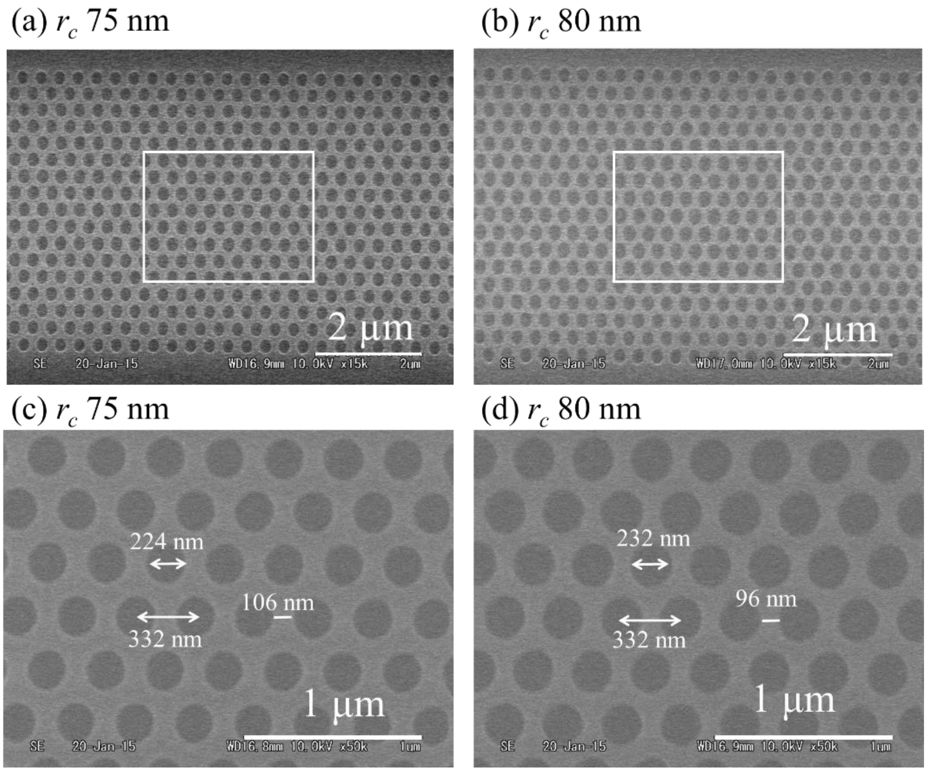

Fig. 3.10 SEM images of the surface of the resist for the PhC structures with different diameters after EBL process. (a) (b) r_c was set as 75 nm and 80 nm respectively. (c) (d) Enlarged SEM images of the marked area in (a) and (b).

Figure 3.11 shows the plan-view SEM images of the samples after mask removing process and the row number is marked left side. It is obvious that, due to proximity effect, the diameter of the air holes is larger in the central area in both samples which is corresponding to the experiment results after EBL process. When the r_c was set as 75 nm in the EBL process, the surface of the PhC structure is very neat without any damage as shown in Fig. 3.11(a), while the central area ranging from 6th row to 12th row in the PhC structure using 80 nm as the radius in EBL process cracked as shown in Fig. 3.11(b). Most cracks in Fig. 3.11(b) generated between the air holes at the central area and broke the PhC structure. These cracks were brought from the ICP deep etching process for GaAs substrate. Due to the big diameter of the air holes, the space and the side walls left for isolating the air holes become thinner. The thin side walls cannot resist the corrosion of Cl^+ ions and plasma generated in ICP deep etching process, so that the PhC structure with large diameter of air holes was easily broken.

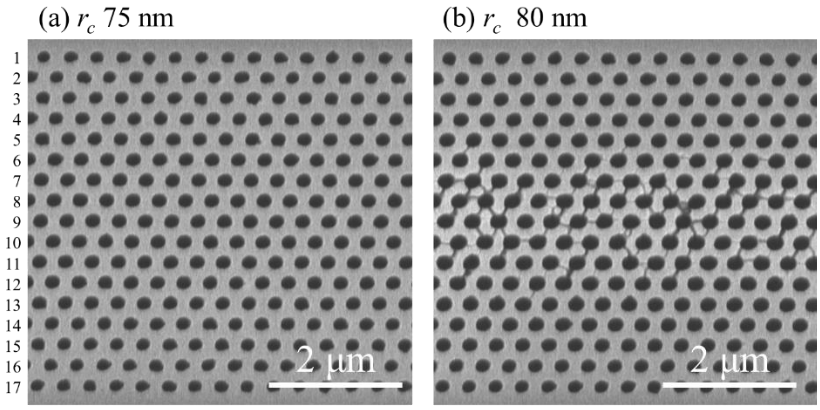

Fig. 3.11 Plan-view SEM images of the fabricated GaAs based PhC structures using (a) 75 nm and (b) 80 nm as the set value of r_c in EBL process. The numbers marked on the left side are the row number of the PhC structure.

Figure 3.12 shows the filling ratio *r/a* of each row in the PhC structures. For the sample using 75 nm, even though the overexposure and proximity effect can expand the final diameter of the air holes in the PhC structure, the highest *r/a* is still smaller than 0.3. On the other hand, for the sample using r_c as 80 nm, the filling ratio is larger than 0.3 where the PhC structure ranging from 5^{th} to 13^{th} row and saturated from 7^{th} to 11^{th} row. However, within the saturation region, the PhC structure was broken due to the thin side walls. For achieving a PhC structure having filling ratio higher than 0.3 without any damage, enough space left between the air holes and big diameter of the air holes are both necessary for fabricating the PhC structures. Therefore, a and r_c were set as 340nm and 80 nm respectively in EBL process in the following experiments. The increase of the lattice constant might leave enough space for isolating the air holes and reduce the filling ratio. It is hope that the filling ratio can still maintain higher than 0.3 by using these parameters even though the lattice constant is increased.

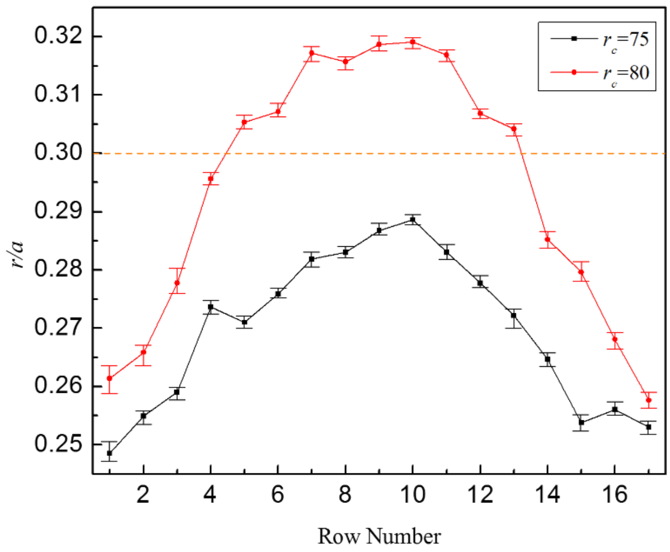

Fig. 3.12 The variations of the filling ratio *r/a* for the two PhC structures shown in Fig. 3.11 depending on the row number.

For investigating the influence induced from mask retardation, three samples with different mask thicknesses was fabricated. Figure 3.13 shows the SEM images of surface of SiN_x masks with thickness of 150 nm, 200 nm, and 250 nm, respectively. These three samples were obtained by setting a_c (value of lattice constant set in CAD) as 340 nm and r_c as 80 nm. It is observed that when the mask is 250 nm-thick, the space between the air hole generates cracks. The mask with cracks will lose the protecting function, and let the deep dry etching process of GaAs substrate fail.

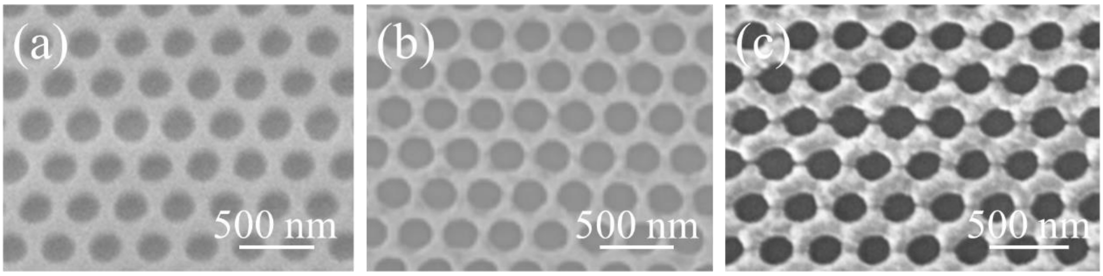

Fig. 3.13 SEM images of the surface of SiN_x masks. The thicknesses of the masks are (a) 150 nm, (b) 200 nm, and (c) 250 nm, respectively.

On the other hand, during the ICP mask etching process, mask retardation as shown in Fig. 3.14 cannot be ignored. Because of the strong physical etching effect, the sidewall of the air holes is no longer vertical. The sloping sidewall reduces the radius of the air holes at the bottom of the air holes, which determines filling ratio of the final fabricated PhC structure. Furthermore, thicker masks need longer time to do mask etching. So when ICP etching process lasted longer, more corrosions were happened on the sidewalls and the space between the air holes. It makes the mask fragile and finally crack due to the strain between the GaAs substrate and the mask. Therefore, 150 nm was adopted as the thickness of the mask layer in the following experiments, not only for achieving a higher filling ratio on the final fabricated PhC structure, but also for getting a perfect mask layer without any crack.

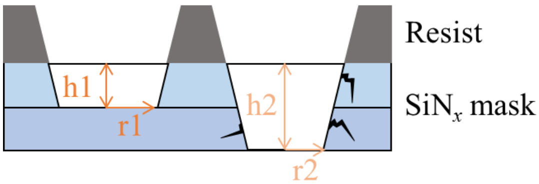

Fig. 3.14 Schematic illustration of the influence of using a thicker mask caused by mask retardation.

3.2.3 Dry etching of GaAs

Figure 3.15 shows the SEM images of GaAs PhC structures using the SiN_x mask of 150 nm which were etched for different time. The etching parameters used are list in Table 3.3 which is based on the optimized etching condition for AlGaAs. From the profiles, it can be observed that the depth of the air holes has the largest value when the air holes is in the central area. The reason is that the incident direction of ions and atoms is not vertical which is caused by the collisions in the plasma as shown in Fig. 3.15(d). The flux for the active radicals is dependent on the diameter of the air holes because the incident radicals is not perfect normal to the surface of the samples [13]. When the diameter of the air holes is larger, the flux is larger. More active radicals are incident to the air holes, so the air holes with larger diameter have larger etching rate. Due to the proximity effect in the EB lithography process, the diameter of the air holes is larger at the central area. Therefore, the air holes in the central part has the largest depth value. For evaluating the etching rate, the largest depth value for each sample was used. The etching depth for the three samples is linearly increases with the etching time.

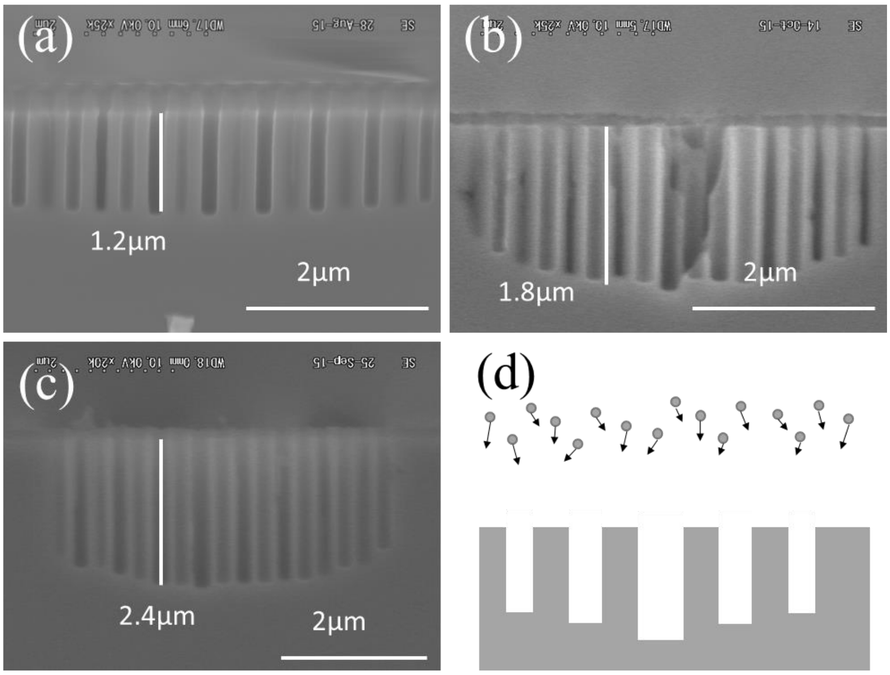

Figure 3.15 GaAs substrate etched for (a) 200s, (b) 250s, (c) 300s. (d) Illustration of the flux of incident radicals dependent on the diameter of the air holes.

Figure 3.16 shows the SEM images of the surface of the GaAs PhC structure using the SiN_x mask of 150 nm. The etching time was set as 220s. The mask layer has already been removed by etching process with C_3F_8 gas. According to this image, the lattice constant is 347 nm which is different from the value in Fig. 3.10. The error is caused by using the SEM method to measure the length. Because the radius observed by SEM images are 230 and 236 nm, *r/a* of these two samples are 0.333 and 0.339 when r_c were set as 75 and 80 nm, respectively. The filling ratio is a bit smaller than that on the resist due to mask retardation. Both the samples achieved the goal of *r/a*>0.3. Furthermore, due to the fully protection of 150 nm SiN_x mask, the surface of the PhC structure finally obtained is flat and neat.

Table 3.3 The etching conditions used to etch GaAs substrate for a different time.

	(a)	(b)	(c)
Cl_2 flow rate (sccm)	12	12	12
BCl_3 flow rate (sccm)	18	18	18
CH_4 flow rate (sccm)	3	3	3
Pressure (Pa)	0.6	0.6	0.6
Antenna power (W)	300	300	300
Bias power (W)	23	23	23
Time (s)	200	250	300

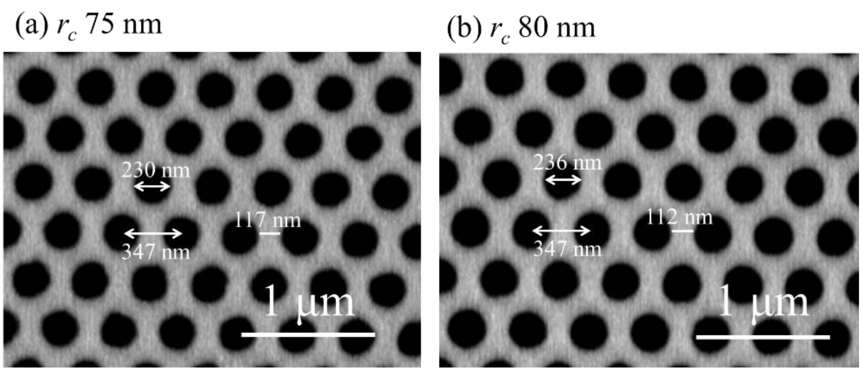

Fig. 3.16 (a), (b): SEM images of the surface of GaAs PhC etched for 220s.

The depth of the air holes was about 1.4 µm for the sample with r_c of 80 nm which is shown in Fig. 3.17. This value is enough to fabricate the proposed PhC cavity lasers. The profile of the air holes was shown in Fig. 3.17(b). It is obvious that the air holes are vertically etched. Furthermore, for avoiding the proximity effect, a PhC structure with 35 lines of air holes was fabricated. The diameter of the air holes in the central 20 lines has uniform value, because the accumulated energy saturates in this area during EB lithography.

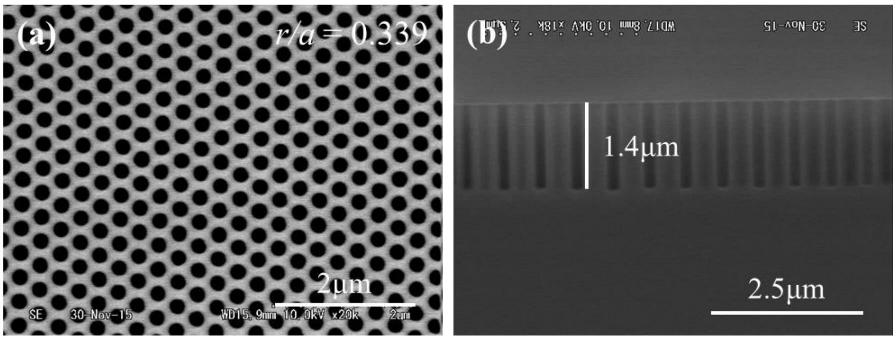

Fig. 3.17 The optimized dry etching of GaAs using SiN_x mask with thickness of 150 nm. (a) The surface of the fabricated GaAs-based PhC structure. (b) The profile of the air holes.

3.3 Summary

The ICP deep dry etching of $Al_{0.8}Ga_{0.2}As$ for the fabrication of a PhC structure has been investigated. By applying antenna power during the SiN_x mask etching process, the verticality of the air holes in the mask layer was improved owing to the contribution of chemical etching effect. Furthermore, when SiN_x was used as the mask layer, the vertical profile of the air holes fabricated by ICP dry etching was round because the charge up on the sidewall of the SiN_x mask layer bends the trajectories of the incident positive ions. Then, a thinner SiN_x mask layer was used to suppress the mask retardation and the effect caused by charge up. As a result, a PhC structure having air holes with a depth of 1.7 μm and a diameter of 190 nm was obtained.

For realizing WDM by using the designed PhC cavity laser with circular resonators operating at 1.3-μm range, the target filling ratio *r/a* of the PhC structure was set to be larger than 0.3 when *a* is 340 nm. Due to the electron scattering in EB lithography process and mask retardation in mask etching process, the setting value in the EB lithography process and the thickness of the

SiN_x mask layer were both optimized. Firstly, regular PhC patterns can be achieved on the resist when a_c was set as 340 nm and r_c was 75 and 80 nm in EB lithography process. Secondly, the thickness of SiN_x mask was optimized as 150 nm for protecting the substrate when etching the GaAs substrate. Finally, a GaAs PhC structure with r/a>0.3 was successfully fabricated after mask removing process.

References

[1] K. Avary, J. P. Reithmaier, F. Klopf, T. Happ, M. Kamp, and A. Forchel: “Deeply etched two-dimensional Photonic crystals fabricated on GaAs/AlGaAs slab waveguides by using chemically assisted ion beam etching,” Microelectronic Engineering 875, 61 (2002).

[2] R. Braive, L. Le Gratiet, S. Guilet, G. Patriarche, A. Lemaıˆtre, A. Beveratos, I. Robert-Philip, and I. Sagnes: “Inductively coupled plasma etching of GaAs suspended Photonic crystal cavities,” Journal of Vacuum Science & Technology B 27, 1909 (2009).

[3] M. T. Todaro, T. Stomeo, V. Vitale, M. DeVittorio, A. Passaseo, R. Cingolani, F. Romanato, L. Businaro, and E. Di Fabrizio: “Nanofabrication of high refractive index contrast two-dimensional Photonic crystal waveguides,” Microelectronic Engineering 670, 67 (2003).

[4] S. Chakravarty, P. Bhattacharya, and Z. Mi: “Electrically Injected Quantum-Dot Photonic Crystal Microcavity Light-Emitting Arrays with Air-Bridge Contacts,” IEEE Photonics Technology Letters 18, 2665 (2006).

[5] Y. Kitabayashi, M. Mochizuki, F. Ishikawa, and M. Kondow: “Over 1.5 μm Deep Dry Etching of Al-Rich AlGaAs for Photonic Crystal Fabrication,” Japanese Journal of Applied Physics 52, 04CG07 (2013).

[6] N. Ikeda, Y. Sugimoto, Y. Watanabe, N. Ozaki, Y. Takata, Y. Tanaka, K. Inoue, and K.

Asakawa: “Precise control of dry etching for nanometer scale air-hole arrays in two-dimensional GaAs/AlGaAs Photonic crystal slabs,” Optics Communications 275, 223 (2007).

[7] W. R. Entley, W. J. Hennessy, and J. G. Langan: “C_2F_6/O_2 and C_3F_8/O_2 Plasmas SiO_2 Etch Rates, Impedance Analysis, and Discharge Emissions,” Electrochemical and Solid-State Letters 3, 99 (2000).

[8] B. Schuppert, E. Brose, K. Petermann, and R. Moosburger: “Anisotropic plasma etching of polymers using a cryo-cooled resist mask,” Journal of Vacuum Science & Technology A 18, 385 (2000).

[9] R. A. Gottscho, C. W. Jurgensen, and D. J. Vitkavage: “Microscopic uniformity in plasma etching,” Journal of Vacuum Science & Technology B 10, 2133 (1992).

[10] X. Zhang, Y. Togano, K. Hashimura, M. Morifuji, and M. Kondow: “Dry etching of Al-rich AlGaAs with silicon nitride masks for Photonic crystal fabrication,” Japanese Journal of Applied Physics 54, 042003 (2015).

[11] Y. Kalra and R. Sinha, Pramana.: “Photonic band gap engineering in 2D Photonic crystals,” Pramana 67, 1155 (2006).

[12] T. H. P. Chang: “Proximity effect in electron-beam lithography”, Journal of Vacuum Science and Technology 12, 1271 (1975).

[13] J. Tonotani, T. Iwamoto, F. Sato, K. Hattori, S. Ohmi, and H. Iwai: “Dry etching characteristics of TiN film using Ar/CHF_3,Ar/CHF_3, Ar/Cl_2,Ar/Cl_2, and Ar/BCl_3Ar/BCl_3 gas chemistries in an inductively coupled plasma”, Journal of Vacuum Science &

Technology B, Nanotechnology and Microelectronics: Materials, Processing, Measurement, and Phenomena 21, 2163 (2003).

Chapter 4

Dry Etching of GaAs/AlGaAs-Based Epi-wafer

4.1 Introduction

This chapter is mainly focused on the dry etching of GaAs/AlGaAs-based epi-wafers. Due to the vertical current injection structure, CirD laser is expected to have smaller electrical resistance than the devices which use membrane and lateral current injection structure. Therefore, higher output power and better performance can be expected on CirD lasers. For obtaining PhC structures, periodically arranged air holes with highly regular shape and excellent deep profile should be fabricated on epi-wafers. The shape and profile of the air holes affect the optical performance of the devices greatly. Therefore, it is important to obtain air holes with perfect shape on the epi-wafers.

InAs QDs are often chosen as the gain material for fabricating PhC lasers, because InAs QDs have the ability of carrier confinement and suppress the surface recombination on the side walls of the air holes [1,2]. For fabricating CirD laser, InAs QDs are also considered as the gain material. Some reports discussed the dry etching of GaAs/AlGaAs-based waveguide, PhC slab or mesa structure [3-6]. Dry etching of GaAs layer implanted with InAs QDs has also been presented in Ref. 1 and 7 for achieving a membrane PhC structure. Table 4.1 summarized the details of the reports discussing on the etched GaAs/AlGaAs-based structure. In this study, the PhC structure having deep air holes should be fabricated in the epi-wafer with GaAs/AlGaAs heterostructure, so that it's different from the reports discussing on fabricating membrane structure. Note that membrane structure only needs shallow dry etching process. Furthermore, there are few report on discussing the influence of InAs QDs on etching process for fabricating PhC structures in an epi-wafer with heterostructure. The epi-wafer used in this study has 5-stacked layers of InAs QDs with a density as much as 6×10^{10} cm^{-2}, which is about 3 times of the density used in Ref. 1. The InAs QDs with multi stacked layers and high density are used for expecting higher gain and output on CirD laser. However, in this study, it is found that InAs QDs in the epi-wafer impede vertical etching of the air holes, and contractions of the diameter of the air holes appear in the core layer (see Fig. 4.1(a)). The target that how much contraction is acceptable for fabricating CirD lasers is determined by simulations. For reducing the contractions in the core layer, the dry etching process was studied. Another epi-wafer with 3-stacked layers of InAs QDs was also etched for investigating the influence of the stacked layer numbers.

In this chapter, the dry etching process for obtaining air holes penetrating multi layers with various materials, such as GaAs, AlGaAs, and InAs QDs, was optimized.

Table 4.1. Reports about various GaAs/AlGaAs-based structures obtained by dry etching process. [11]

Authors	Etched structure	QDs	Sample structure	Dry etching gas
Zhang *et al*. [3]	PhC	No	Heterostructure	$Cl_2/BCl_3/CH_4$
Nomura *et al*. [2]	PhC	5 stacked layers	Membrane	Cl_2/Ar
Ikeda *et al*. [4]	PhC	No	Heterostructure	Cl_2/Ar
Volatier *et al*. [7]	Waveguide	No	Heterostructure	$Cl_2/BCl_3/Ar/N_2$
Braive *et al*. [8]	PhC	No	Heterostructure	Cl_2/N_2
Kim *et al*. [9]	Mesa	No	Heterostructure	BCl_3/N_2
Shokouhi *et al*. [10]	PhC	Single layer	Membrane	$Cl_2/BCl_3/Ar$

4.2 Experiments

For optimizing the dry etching process of the epi-wafer, four kinds of epi-wafer are used in this chapter. The structures of the used samples are illustrated in Fig. 4.1. The epi-wafer of Fig. 4.1(a) shows a typical construction used for fabricating the electrically driven CirD lasers [8,9]. This epi-wafer is denoted as Epi1. Epi1 has two 300 nm thick $Al_{0.95}Ga_{0.05}As$ layers, a 100 nm thick GaAs cap layer, and a 320 nm thick core layer epitaxially grown on a (001) GaAs substrate. For investigating the dry etching process on the core layer more conveniently, the upper 2 layers (GaAs cap layer and upper $Al_{0.95}Ga_{0.05}As$ layer) of Epi1 were removed. The modified epi-wafer is denoted as Epi2 as shown in Fig. 4.1(b). Furthermore, for investigating the influence of QDs during the etching process, reference samples were used as shown in Fig. 4.1(c) and Fig. 4.1(d). The reference samples have the structures similar to Epi2. The reference sample shown in Fig. 4.2(c) which is denoted as Epi3 has no QD in the undoped GaAs epi-layer. Another reference sample shown in Fig. 4.1(d) which is denoted as Epi4 has 3-stacked layers of InAs QDs in GaAs epi-layer. The thickness of the core layer is 220 nm because Epi4 was designed for optically pumped CirD laser. The density of the InAs QDs in each stacked layers for Epi1, Epi2, and Epi4 is the same value of 6×10^{10} cm^{-2}.

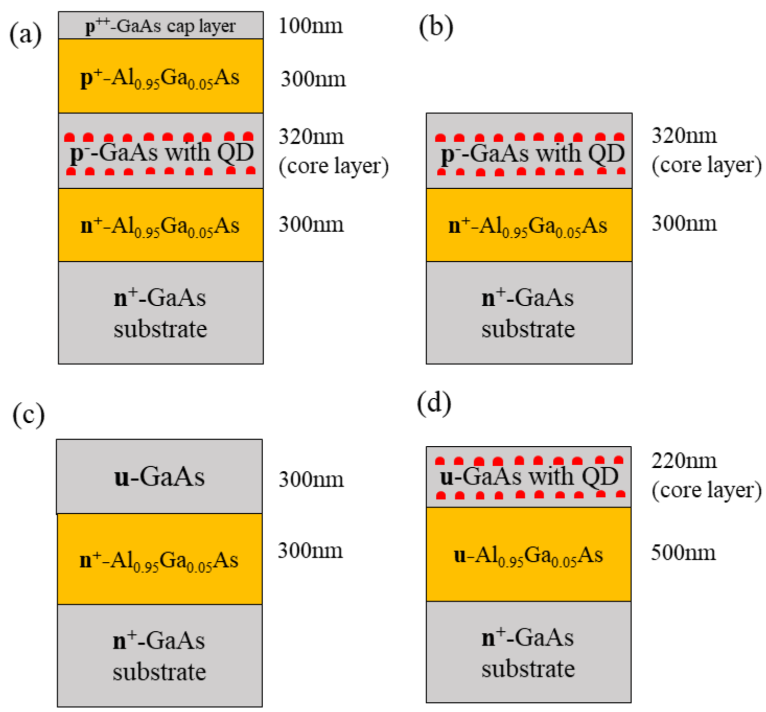

Fig. 4.1 The structures of the epi-wafers used in this study are denoted as (a) Epi1, (b) Epi2, (c) Epi3, and (d) Epi4, respectively. [11]

The experimental procedures for optimizing the dry etching process of the epi-wafer are illustrated in Fig. 4.2. Firstly, the samples were prepared from cutting the epi-wafers to small square pieces with the size of 8×8mm. Then the samples were cleaned by acetone and ethyl alcohol in sequence for removing organic impurities. Secondly, a resist layer with the thickness of ~350 nm was spin-coated on the samples. PhC structures were drawn on the resist by EB lithography process. As the resist, ZEP520A is adopted due to its high sensitivity as mentioned in Chapter 2 [7,10] and dose amount was set as 110 $\mu C/cm^2$ at 30 kV. The lattice constant *a* of the PhC structures were set as 340 nm to realize 1.3-μm lasing, and the radius of the air holes are adjust to be about 110 nm after developing. Thirdly, the samples were etched by ICP etching processes. The $Cl_2/BCl_3/CH_4$ gas mixture was employed for providing the plasma chemistry. Chlorine is the main etching agent which is the same as the etching process in Chapter 3. BCl_3 can remove aluminum oxide and thus obtain deeper and faster etching [12,13]. CH_4 can passivate side-wall by forming polymers with etch products [14,15]. The antenna power which is used to adjust the ICP density was set to 150W~400 W, and the bias power used to form DC bias on the electrode was set as 23W. After the ICP dry etching process, the samples was soaked in the N,N-dimethylacetamide (ZDMAC) for 10 minutes to remove the residual resist. The fabricated etched structure was investigated by SEM.

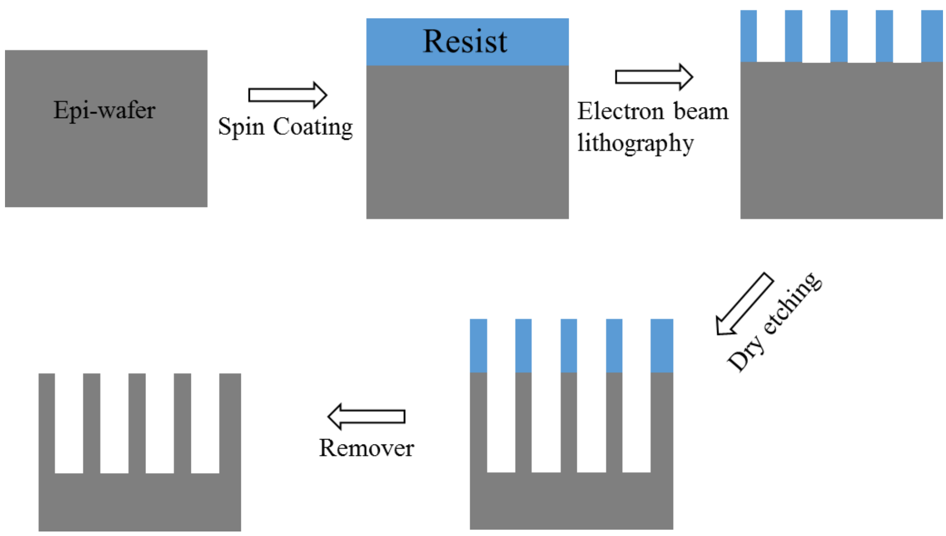

Fig. 4.2 Simplified fabricating procedures using photoresist as the mask.

Contractions of the diameter in the air holes often appear in the experimental results as shown in Fig. 4.3(a), the shrinkage rate S which is obtained by Eq. (4.1) was used to evaluate the quality of the etched air holes.

$$S = 1 - \frac{d_2}{d_1} \tag{4.1}$$

where d_1 is the largest diameter in the air hole and d_2 is the smallest one. The errors induced by measuring the absolute lengths on the SEM images can also be eliminated by using S as the evaluation parameter. Moreover, for acquiring accurate S, it is expected that the air holes should be cut along the diameter as shown in Fig. 4.3(b), and d_1 and d_2 were then measured. However, it is very difficult and almost impossible to ensure that the line of cut crosses the diameter of the air holes. The real line of cut usually has an angle with a small degree to perfect cutting line and runs through several lines of PhC structure as shown in Fig. 4.3(c). Therefore, the air holes with the biggest diameter among all the profiles in the SEM images for getting the approximate value of S were measured.

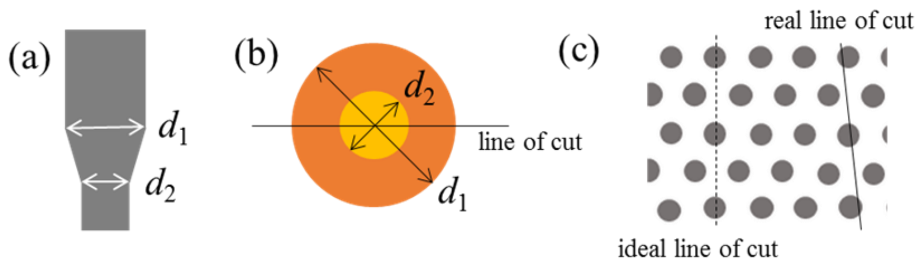

Fig. 4.3 (a) A typical profile of air holes obtained by using non-optimized dry etching recipe. (b) The platform of the air holes with contraction. (c) The illustration schematic of real cutting lines on the PhC structure. [11]

4.3 Results and discussion

4.3.1 Contractions in the core layers

Firstly, the dry etching process for the GaAs/AlGaAs-based epi-wafer was investigated based on the optimized condition used for etching $Al_{0.8}Ga_{0.2}As$ which has been introduced in

Chapter 3. The dry etching process should form air holes penetrating multi layers with various materials, such as GaAs, $Al_{0.95}Ga_{0.05}As$, and InAs QDs. The optimized ICP dry etching recipe for $Al_{0.8}Ga_{0.2}As$ was shown in Table 4.2. The same etching recipe was applied to etch GaAs substrate, Epi1, Epi2, and Epi3. Figure 4.4(a) and 4.4(b) show the air hole profiles for the GaAs substrate and Epi1 etched for 120 seconds. It is obvious that the GaAs substrate can also be vertically etched and obtain regular air holes using this recipe. For the air holes etched in Epi1, the profile in the GaAs cap layer and the upper $Al_{0.95}Ga_{0.05}As$ layer has good verticality. However, the diameter of the air holes contracts in the core layer. It is considered that there are two possible reasons for the contractive profile. One is the charge-up formed on the side walls in the upper two layers [16,17] or the built-in electric field caused by p-n junction, which may affect the trajectory of the incident ions. Another possible reason is that this recipe has selectivity among GaAs and InAs QDs in the core layer because InAs has generally lower etching rate than GaAs. In order to clarify the cause of contraction, Epi2 and Epi3 were etched for 80 seconds, and the results are shown in Fig. 4.4(c) and 4.4(d). The air holes in Epi2 also have contractions of diameter in the core layer which is similar with Epi1, while $Al_{0.95}Ga_{0.05}As$ layer got vertically etched. The *S* value shown in Fig. 4.4(b) and 4.4(c) are 37% and 33% respectively and they are almost the same. It means that the contraction was not caused by the charge-up on the side walls or the built-in electric field. Furthermore, regular air holes with good shape were also obtained on the epi-wafer without QDs as shown in Fig. 4.4(d). Because Epi3 has a similar heterostructure to that of Epi2, the contraction on Epi1 and Epi2 should be attributed to the influence induced by InAs QDs. Even though there is few report on discussing the mechanism of dry etching for InAs using $Cl_2/BCl_3/CH_4$ gas mixture, Fig. 4.4(c) and 4.4(d) may imply InAs QDs have lower etching rate than GaAs using this recipe. It is caused by the etch product of $InCl_3$ with low volatility compared to other group-III chlorides at room temperature [18]. $InCl_3$ tends to remain at the bottom and side wall of the air holes, acting as obstacles to keep the same diameter and hinder the air holes being vertically etched in the following etching process. This is also called as micro-masking effect [19]. Therefore, the high density of QDs and multi stacks may intensify the contraction.

Table 4.2. Parameters of ICP etching process used for the GaAs substrate, Epi1, 2, and 3. [11]

Chamber Pressure (Pa)	CH_4 flow rate (sccm)	Cl_2 flow rate (sccm)	BCl_3 flow rate (sccm)	Antenna power (W)	Bias power (W)
0.6	3	12	18	300	23

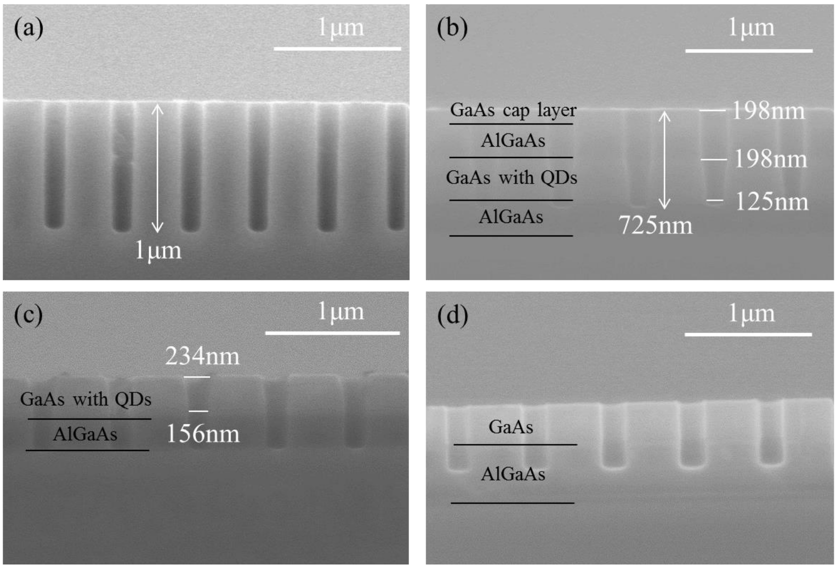

Fig. 4.4 The SEM images of the profiles for (a) GaAs substrate, (b) Epi1, (c) Epi2, and (d) Epi3 using the etching recipe optimized for etching of $Al_{0.8}Ga_{0.2}As$. [11]

4.3.2 Target value of *S*

For achieving better performance for the PhC devices, the air holes should be vertically etched and *S* should be 0 in ideal situation. However, the ideal value cannot be achieved sometimes due to the restrictions of the process conditions. According to the calculated curves of the threshold current density as a function of *Q* factor for a PhC cavity laser, [20] the *Q* factor of the cavity should be higher than 4000, so that the threshold current density is small enough for room temperature continues wave lasing. The variation of the *Q* factor of the WGM in a typical CirD laser dependent on *S* has also been simulated 3D FDTD method. The simulation model consists of a GaAs core layer of 320 nm which is sandwiched by two AlO_x cladding layers. The lattice constant *a* of the PhC structure is 340 nm. For obtaining lasing operation of the WGM in the 1.3 μm range, the radii of the air holes and circular cavity are set as $0.3a$ and $2.8a$, respectively. The results show that the highest Q factor 5300 of the WGM was achieved when S is 0. Then Q factor is consistently reduced down to 3900 along with the increasing of S up to 15%, and Q factor is 4100 when S is 10%. Therefore, S value in the etched epi-wafer should be smaller than 10% for ensuring the lasing operation of fabricated CirD laser. If smaller S is achieved, better performance of fabricated PhC devices can be expected. The following experiments are aiming to obtain S as small as possible in the core layer.

4.3.3 Reducing CH_4 flow rate

For reducing the effect induced by the QDs and getting smaller S, the dry etching process for Epi2 was optimized. The CH_4 flow rate was firstly reduced in order to suppress the side wall passivation effect, so that the GaAs on the side wall can react with the plasma chemistry more easily for improving the profile. Fig. 4.5(a) and 4.5(b) shows the profile of the air holes etched with the CH_4 flow rate of 1.5 sccm and 0.5 sccm. Both samples were etched for 80 seconds and other etching parameters are the same as the one listed in Table 4.3. S value for these two samples was reduced down to 20% and 14% respectively as expected, but still not achieve the target. It means that the influence induced by QDs cannot fully eliminated by simply reducing the passivation effect. The characteristics of the QDs affecting the dry etching process should be further investigated.

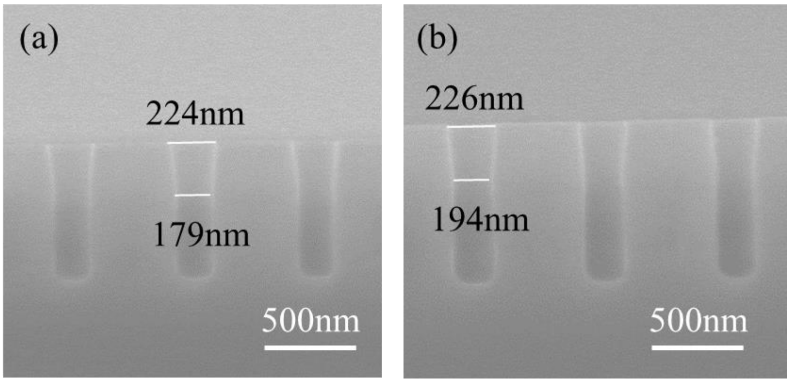

Fig. 4.5 Epi2 etched with CH_4 flow rate of (a) 1.5 sccm, and (b) 0.5 sccm. [11]

For investigating the influence of stacked numbers of the QDs, the epi-wafer having the core layer with 3-stacked layers of InAs QDs has also been etched. Figure 4.6(a) and 4.6(b) show the profiles of Epi4 samples etched with CH_4 flow rate of 1.5 and 0.5 sccm for 80 seconds, respectively. *S* value in the core layer for Epi4 is 15% when CH_4 flow rate is 1.5 sccm. The air holes can be vertically etched when CH_4 flow rate is reduced to 0.5 sccm without adjusting other etching parameters as shown in Fig. 4.6(b). *S* value for Epi4 can be reduced down to 0 by simply reducing the passivation effect. *S* value in the core layer of the epi-wafers etched by various CH_4 flow rate are listed in Table 4.3. Other etching parameters are the same as the one listed in Table 4.2. By reducing the CH_4 flow rate, the verticality of the air holes can be improved for all samples. Comparing the results of Epi4 samples with the experiments for Epi2, the contraction in the core layer is weaker when less stacks of QDs layers are used. On the other hand, vertical etched air holes were also obtained in Ref. 14 for a GaAs membrane having 5-stacked InAs QDs layer, but with lower density. It means that the contraction of the diameter of the air holes which is caused by the InAs QDs can be suppressed by reducing the stacked layers or the density.

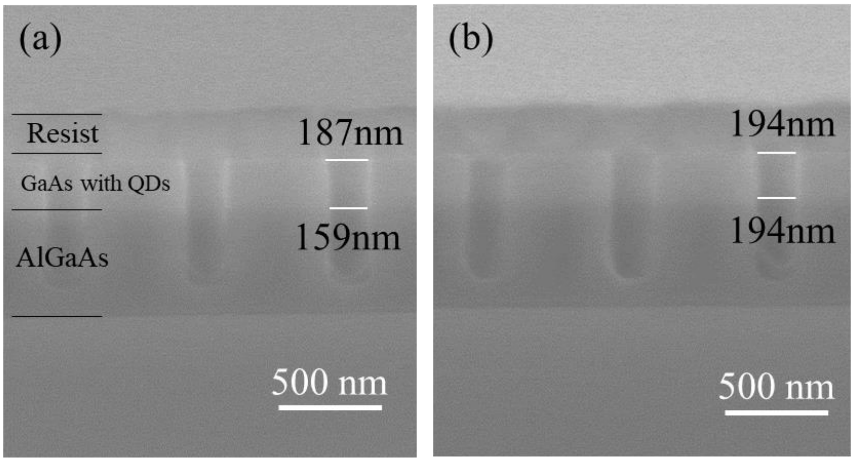

Fig. 4.6 Epi4 etched with CH_4 flow rate of (a) 1.5 sccm, and (b) 0.5 sccm. The residual photoresist was not removed after dry etching process for these two samples. [11]

Table 4.3. *S* value in the core layer of the samples etched by different conditions. [11]

Figure No.	Wafer	CH_4 flow rate (sccm)	Number of QDs layers	*S*
4.5(b)	Epi1	3	5	37%
4.5(c)	Epi2	3	5	33%
4.6(a)	Epi2	1.5	5	20%
4.6(b)	Epi2	0.5	5	6%
4.7(a)	Epi4	1.5	3	14%
4.7(b)	Epi4	0.5	3	0

4.3.4 Adjusting antenna power

Even though air holes with vertical profiles has been achieved on Epi4, the epi-wafers having 5-stacked layers of QDs is supposed to be used in practically fabricating electrically driven CirD laser for obtaining higher gain. It is still necessary to etch air holes with smaller *S* on Epi1 and Epi2. For achieving the target value of *S* on Epi2, the antenna power was adjusted to change plasma density for finding the best balance between physical etching effect and chemical etching effect. Figure 4.7(a) shows the *S* of the air holes versus the antenna power when the CH_4 flow rate was set as 0.5 sccm, and etching time is 80 seconds for all samples. The graph shows that *S* achieves the smallest value when the antenna power is 220 W. Figure 4.7(b) shows the profile of the air holes etched with the CH_4 flow rate of 0.5 sccm and antenna power of 220W. The *S* value was as small as 6%. The contraction becomes obvious when the antenna power is too high or too small. This result implies that the InAs QDs were mainly removed by physical etching which is close to physical sputtering process as shown in Fig. 4.8. When the antenna power is reduced, the physical etching effect was enhanced. More InAs QDs on the side wall are removed by the collisions with ions with higher energy and *S* becomes smaller. However, when the antenna power is smaller than 220W, *S* increases. It is because GaAs cannot be vertically etched due to too strong physical etching effect. In these conditions, the chemical reaction between the plasma chemistry and GaAs becomes insufficient due to the low plasma density.

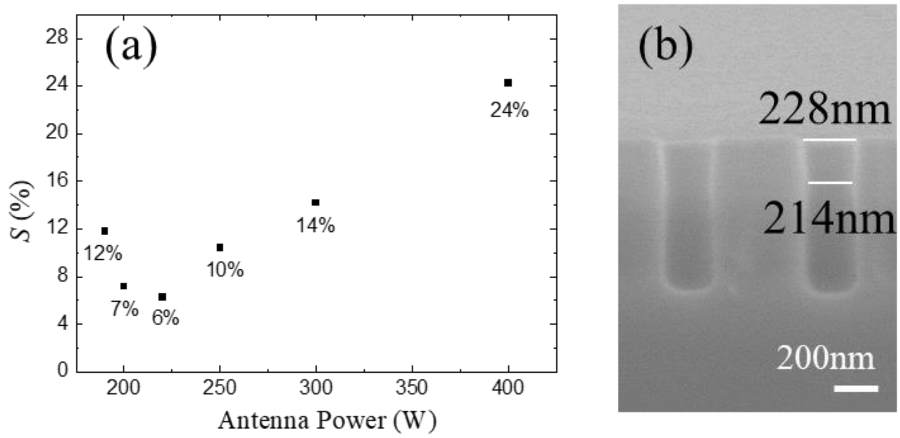

Fig. 4.7 (a) *S* value of the samples etched with various antenna power with CH_4 flow rate of 0.5sccm. (b) Epi2 etched with CH_4 flow rate of 0.5sccm and antenna power of 220W. [11]

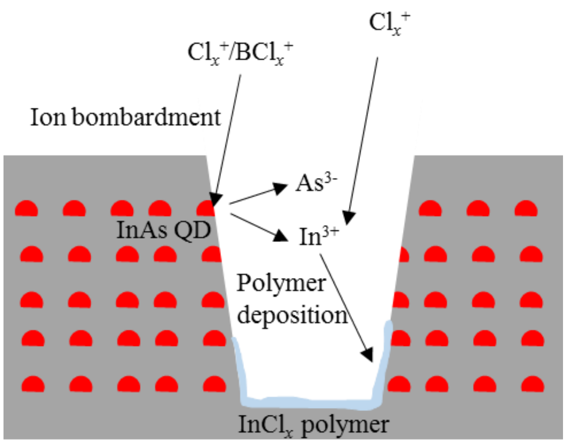

Fig. 4.8 The sputtering of the InAs QDs and the deposition of polymer occur when etching the core layer.

4.3.5 Etching by multi-step recipe

For obtaining air holes with better profile on Epi1, an etching recipe containing with several steps was used. For the GaAs cap layer and $Al_{0.95}Ga_{0.05}As$ layers, the etching recipe in Tab. II was used, and for the core layer with InAs QDs, the optimized dry etching recipe with CH_4 flow rate of 0.5sccm and antenna power of 220W was used. The etching time for each step was adjust for controlling the correspondence between the layers and etching recipe. The combined etching recipe having three steps is listed in Table 4.4. Figure 4.9 shows the SEM images of two Epi1 samples etched by the multi-step dry etching recipe. The profile shows minor contraction in the core layer, and other layers are vertically etched. The results show that the multi-step etching process don't affect the profile of the GaAs cap layer and $Al_{0.95}Ga_{0.05}As$ layers even though the plasma condition in the etching chamber changed during the whole etching process. The *S* values on the core layer are 7% and 5% for Fig. 4.9(a) and 4.9(b), which match with the smallest result for Epi2 of 6%. Comparing with the result shown in Fig. 4.4(b), the profile of the etched air holes was greatly improved. Figure 4.9(c) shows the surface of the PhC structure etched on Epi1. Air holes with regular circular shape can be observed and the fabricated PhC structure has a lattice constant of 342 nm. Thus, the air holes with minor bending on the profiles and regular circular shape on the surface was achieved on the Epi1 by using a multi-step etching recipe.

Table 4.4. The etching recipe with multi steps used for Epi1. [11]

	Step1	Step2	Step3
Chamber pressure (Pa)	0.6	0.6	0.6
CH_4 flow rate (sccm)	3	0.5	3
Cl_2 flow rate (sccm)	12	12	12
BCl_3 flow rate (sccm)	18	18	18
Antenna power (W)	300	220	300
Bias power (W)	23	23	23
Time (s)	65	50	50

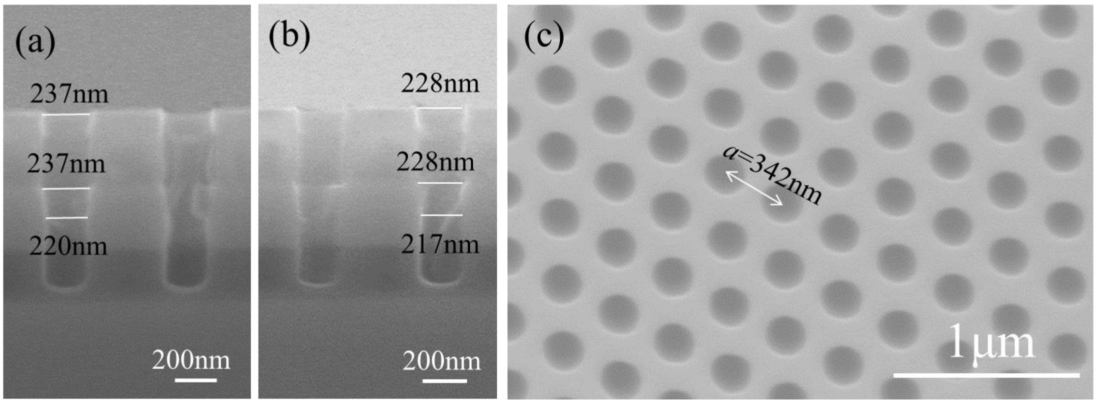

Fig. 4.9 (a) and (b) Cross section view of SEM images for two Epi1 samples etched by the multi-step etching recipe. (c) The surface of the etched Ep1 sample. [11]

4.4 Summary

The dry etching process for the GaAs/AlGaAs-based epi-wafer was optimized. The GaAs-based core layer with InAs QDs shows selectivity when the dry etching recipe optimized for GaAs and $Al_{0.95}Ga_{0.05}As$ was used. The contraction of the diameter in the air holes was preliminary suppressed by reducing the passivation effect. By reducing the antenna power, the contraction was further reduced, because good balance between the physical etching effect and chemical etching effect for core layer was achieved. Air holes with minor contraction were etched on the epi-wafer having 5-stacked InAs QDs layers by using a multi-step etching recipe. The shrinkage rate *S* of the etched air holes in the epi-wafer has achieved the target value.

References

[1] K. Takeda, T. Sato, A. Shinya, K. Nozaki, W. Kobayashi, H. Taniyama, M. Notomi, K. Hasebe, T. Kakitsuka and S. Matsuo: "Few-fJ/bit data transmissions using directly modulated lambda-scale embedded active region Photonic-crystal lasers," Nature Photonics **7**, 569 (2013).

[2] M. Nomura, S. Iwamoto, M. Nishioka, S. Ishida, and Y. Arakawa: "Highly efficient optical pumping of Photonic crystal nanocavity lasers using cavity resonant excitation," Optics Express, 89, 161111 (2006).

[3] M. Nomura, S. Iwamoto, T. Yang, S. Ishida, and Y. Arakawa: "Enhancement of light emission from single quantum dot in Photonic crystal nanocavity by using cavity resonant excitation," Applied Physics Letters 89, 241124 (2006).

[4] N. Ikeda, Y. Sugimoto, Y. Watanabe, N. Ozaki, Y. Takata, Y. Tanaka, Kuon Inoue, and K. Asakawa: "Precise control of dry etching for nanometer scale air-hole arrays in two-dimensional GaAs/AlGaAs Photonic crystal slabs," Optics Communications 275, 257 (2007).

[5] M. Volatier, D. Duchesne, R. Morandotti, R. Arès, and V. Aimez: "Extremely high aspect ratio GaAs and GaAs/AlGaAs nanowaveguides fabricated using chlorine ICP etching with N_2-promoted passivation," Nanotechnology 21, 134014 (2010).

[6] R. Braive, L. Le Gratiet, S. Guilet, G. Patriarche, A. Lemaître, A. Beveratos, I. Robert-

Philipa), and I. Sagnes: "Inductively coupled plasma etching of GaAs suspended Photonic crystal cavities," Journal of Vacuum Science & Technology B, Nanotechnology and Microelectronics: Materials, Processing, Measurement, and Phenomena 27, 1909 (2009).

[7] L Midolo, T Pregnolato, G Kiršanskė and S Stobbe: "Soft-mask fabrication of gallium arsenide nanomembranes for integrated quantum Photonics," Nanotechnology 26, 484002 (2015).

[8] M. Morifuji and Y. Nakaya: "Numerical Design of Photonic Crystal Cavity Structure with AlAs/AlOx Cladding Layers for Current-Driven Laser Diodes," Japanese Journal of Applied Physics 48 112001 (2009).

[9] M. Morifuji, Y. Nakaya, T. Mitamura, and M. Kondow: "Novel Design of Current Driven Photonic Crystal Laser Diode," IEEE Photonics Technology Letters 21, 513, (2009).

[10] B. Shokouhi, J. Zhang, B. Cui: "Very high sensitivity ZEP resist using MEK:MIBK developer," Micro & Nano Letters 6, 992 (2011).

[11] X. Zhang, K. Takeuchi, X. Cong, Y. Xiong, M. Morifuji, A. Maruta, H. Kajii, and M. Kondow: "Dry etching of deep air holes in GaAs/AlGaAs-based epi-wafer having InAs quantum dots for fabrication of photonic crystal laser," Japanese Journal of Applied Physics 56, 126501 (2017).

[12] R. J. Shul, M. L. Lovejoy, D. L. Hetherington, D. J. Rieger, and J. F. Klem: "Plasma-induced damage of GaAs pn-junction diodes using electron cyclotron resonance generated Cl_2/Ar, BCl_3/Ar, Cl_2/BCl_3/Ar, and $SiCl_4$/Ar plasmas," Journal of Vacuum Science & Technology B, Nanotechnology and Microelectronics: Materials, Processing, Measurement, and Phenomena 13, 27 (1995).

[13] S. W. Pang and K. K. Ko: "Comparison between etching in Cl_2 and BCl_3 for compound semiconductors using a multipolar electron cyclotron resonance source," Journal of Vacuum Science & Technology B, Nanotechnology and Microelectronics: Materials, Processing, Measurement, and Phenomena 10, 2703 (1992).

[14] T. Schwarzl, W Heiß, G K. Oberlehner and G. Springholz: "CH_4/H_2 plasma etching of IV-VI semiconductor nanostructuresm," Semiconductor Science and Technology 14, L11 (1999).

[15] T. R. Hayes, M. A. Dreisbach, P. M. Thomas, W. C. Smith, and L. A. Heimbrook: "Reactive ion etching of InP using CH_4/H_2 mixtures: Mechanisms of etching and anisotropy," Journal of Vacuum Science & Technology B, Nanotechnology and Microelectronics: Materials, Processing, Measurement, and Phenomena 7, 1130 (1989).

[16] C. Kim and Y. Kim, J. Micromech. Microeng: "Prevention method of a notching caused by surface charging in silicon reactive ion etching," Journal of Micromechanics and Microengineering 15, 358 (2005).

[17] H. Hoga, T. Orita, T. Yokoyama and T. Hayash: "Charge Build-Up in Magnetron-Enhanced Reactive Ion Etching," Japanese Journal of Applied Physics 30, 3169 (1991).

[18] S.J. Pearton: "Processing of Wide Band Gap Semiconductor," William & Andrew, New York (2000).

[19] J. Sun, and J. Kosel: "Room temperature inductively coupled plasma etching of InAs/InSb in $BCl_3/Cl_2/Ar$," Microelectronic Engineering 98, 222 (2012).

[20] M. Morifuji and Y. Nakaya: "Numerical Design of Photonic Crystal Cavity Structure

with AlAs/AlO$_x$ Cladding Layers for Current-Driven Laser Diodes," Japanese Journal of Applied Physics 48, 112001 (2009).

Chapter 5

Characteristics of Optical Properties of PhC Laser with a Circular Resonator

5.1 Introduction

The PhC cavity laser structure having the circular cavity has been proposed by Kondow labortary. It is called as CirD laser for abbreviation of circular defect cavity laser which is fabricated in a 2-dimensional PhC structure. The lasing mechanism of CirD laser is very similar with the microdisk laser which has been introduced in Chapter 2. In this Chapter, the optical properties of the circular defect PhC cavity laser under optical pump conditions were investigated. The spectrum of edge emitting light shows CW lasing operation at 1.3 μm at RT. The results imply that the PhC laser with circular defect cavity is promising for WDM laser source for intra-chip optical interconnections.

5.2 Fabrication and measurement

Figure 5.1 shows the schematic diagram of the sample structure of a CirD laser investihated in this chapter. The sample was fabricated using an epi-wafer consisting of a slab layer and an AlGaAs layer, both of which were grown on a GaAs substrate. The slab layer fabricated was a

220-nm-thick GaAs layer with multiple InAs quantum dot (QD) layers. The 500 nm-thick AlGaAs layer was used as the bottom cladding layer for the slab layer when the AlGaAs layer was appropriately oxidized to AlO_x [1]. The PL peak measured at RT from the core layer was located at the wavelength of 1290 nm.

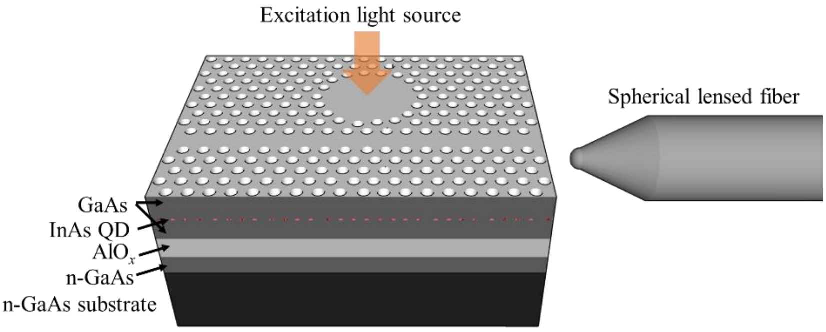

Fig. 5.1 Schematic diagram of the sample structure composed of GaAs, InAs QDs, AlO_x, n-GaAs layer, and n-GaAs substrate. The AlO_x cladding layer is obtained by a selective wet oxidation of AlGaAs. The output light through the waveguide is collected by a spherical lensed fiber. [2]

The fabrication process employed is shown in Fig. 5.2. The EB resist was spin-coated on the epi-wafer firstly. Secondly, the PhC pattern with a circular defect and a line defect was drawn on the resist by using the EB lithography process. According to the simulation results shown in Section 1.2.3, considering the errors of simulations and avoiding the fabrication differences caused in the EB lithography and dry etching process, the lattice constant a of the PhC structure to be fabricated was set as 340 nm, 350 nm, 360 nm, or 370 nm; the radius of the circular cavity R was set as 2.75a, 2.76a, or 2.77a; and the radius of the air holes r was set in the range from 0.24a to 0.31a in the EB lithography process.Thirdly, the sample was etched by a ICP etching process [3] to form the air holes penetrating the core layer. Then, the sample was emerged in the remover to take away the resist. Finally, the bottom AlGaAs layer was fully oxidized to be an AlO_x layer through the air holes by using selective wet oxidization process [4].

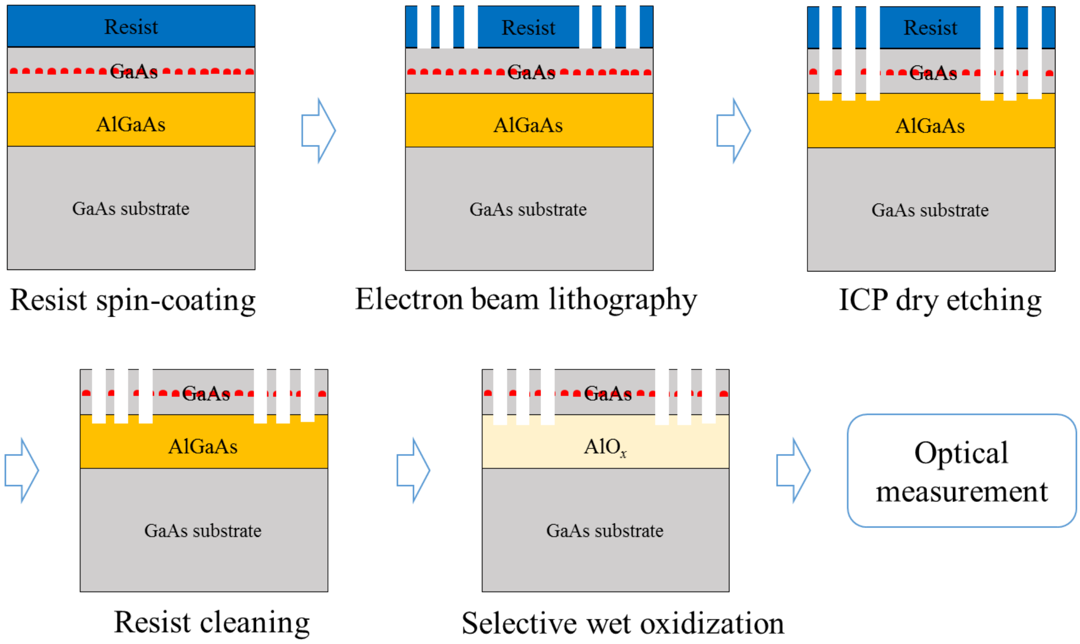

Fig. 5.2 The fabrication procedures for a CirD laser using a sample composed of GaAs epi-layer with InAs QDs, AlGaAs layer, and GaAs substrate.

Optical characterizations were performed with an optical measurement system, as shown in Fig. 5.3. The sample was mounted on a horizontal stage and the circular defect cavity was optically pumped from the upper side along this diection normal to the sample surface, as shown in Fig. 5.1. The pump source used in the experiment was a 785 nm laser diode, and the beam spot was 4 μm in diameter on the cavity surface through a 50× objective lens (numerical aperture = 0.55). The light generated in the circular defect cavity coupled to the line defect waveguide. In order to collect the output light, a spherical lensed fiber (SLF) which is horizontally placed next to the facet of the line defect waveguide. Furthermore, the light vertically emitted from the surface of the cavity was also observed using the same 50× objective lens in the same way as Ref. 7. An optical spectrum analyzer (OSA) with high optical resolution of 0.07 nm was used to measure the spectrum and linewidth of the lasing mode collected by the SLF. Another spectrometer with high sensitivity was used to analyze the lasing mode collected by the 50× objective lens. The optical resolution of the spectrometer is 0.54 nm. The measurements were performed at RT under CW conditions.

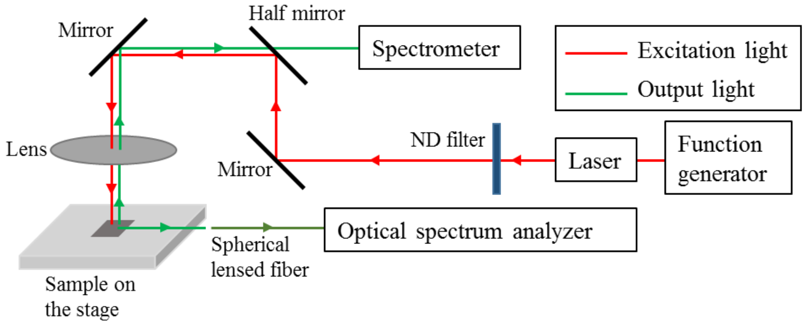

Fig. 5.3 Schematic diagram of optical measurement system used in this study. The spectrometer used to analyze the output light collected by the 50× objective lens has a high sensitivity and an optical resolution of 0.54 nm. The OSA connecting with the SLF has an optical resolution of 0.07 nm

5.3 Experimental results and discussion

Figure 5.4 shows the excitation power versus output power curves measured for typical 3 samples with various parameters. The parameters of samples are listed in the inset of each graph. All curves shown in Fig. 5.4 have a bending turn around the threshold part. By extrapolating the dot lines to the zero output power, the threshold excitation powers were estimated to be about 25 μW for all three samples. The CirD laser using an AlO_x cladding also had an ultra-small threshold which was comparable with the reported PhC lasers with membrane structures [8,9]. The output intensity increased with the increase of excitation power up to about 1 mW without any saturation, which should be attributed to the good thermal conductivity of AlO_x cladding layer [10,11]. The threshold current of the PhC laser with circular defect, I_{th}, can be estimated by the following equation.

$$P_{\mathrm{th}} \times k = I_{\mathrm{th}} \times \frac{hc}{e\lambda}, \tag{4.1}$$

where P_{th} is the threshold excitation power of 25 μW. h is the Planck constant, c is the speed of light in vaccum and e is the elementary charge. k is the ratio of the pump power absorbed by the slab layer to the whole incident power. Due to the similar heterostructure of slab layer and micro-PL measurement system described in Ref. 7, the same value of 0.15 for k can be used in this equation. λ is the wavelength of the lasing mode which is about 1.3 μm. Thus, I_{th} was estimated to be 4 μA, which was close to that of a typical LEAP laser [8,9]. It means that the electrical driven PhC lasers with circular defect cavities could have a reasonably small threshold current.

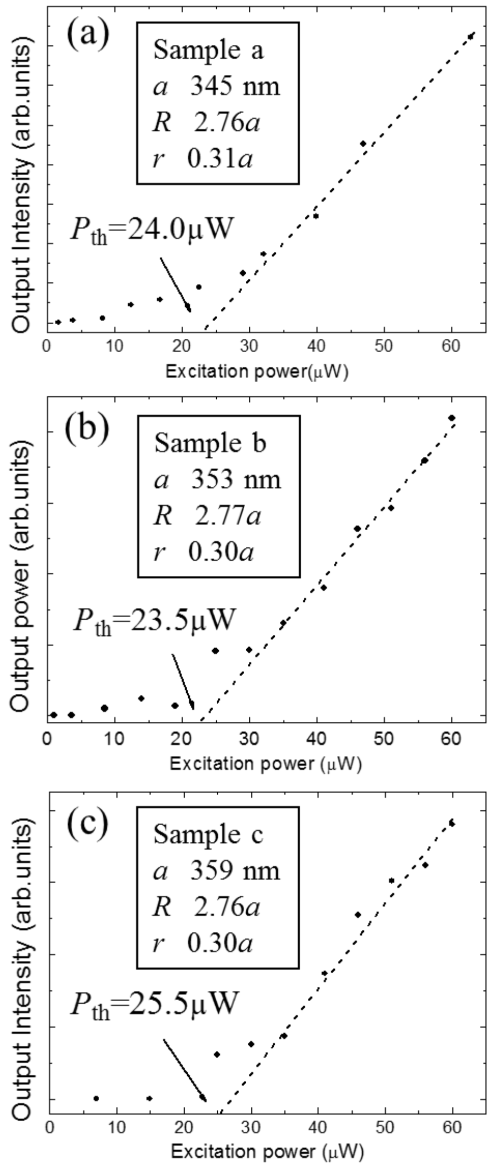

Fig. 5.4 Output intensities as a function of the excitation power measured for three samples with various parameters described in the corresponding insets. [2]

Figure 5.5 shows the spectrum of Sample b collected by the SLF when the excitation power was 0.92 mW. A sharp peak at wavelength of 1296.8 nm having the linewidth Δλ of 0.07 nm was observed. The measured $\Delta\lambda$ was the same as the resolution limit of OSA, which means that the real linewidth might be smaller than 0.07 nm. The cavity-resonant-linewidth was about 0.23 nm if the calculated Q factor of 5600 as illustrated in Fig. 1.12 was used for estimation. The experimental value of $\Delta\lambda$ is much smaller than the estimated cavity-resonant-linewidth. Therefore, the detected mode was of the coherent light, indicating of an obvious lasing operation of the PhC lasers with the circular cavity.

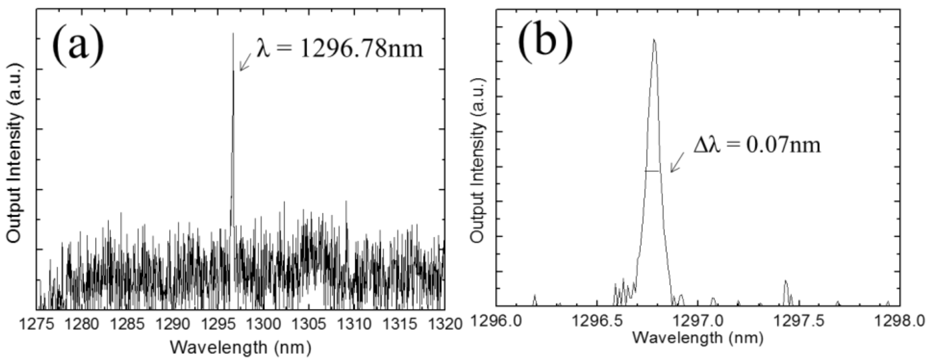

Fig. 5.5 (a) Spectrum for Sample b collected with a spectrum analyzer. (b) The central peak of the spectrum. [2]

Figure 5.6 shows the spectrum of Sample b collected by the objective lens and measured by the spectrometer. The excitation power was also 0.92 mW. A sharp peak at wavelength of 1296.8 nm with linewidth of 0.54 nm can also be observed on the spectrum. The linewidth also achieves the resolution of the spectrometer. Therefore, the sharp peak in Fig. 5.6 corresponds to the lasing mode shown in Fig. 5.5(a). Furthermore, because of low Q factor and weak localization, two wide peaks at 1287.0 nm and 1306 nm show weak amplified spontaneous emission in the cavity. By comparing the spectra collected by the objective lens and SLF, these non-lasing modes were suppressed mightily when the light was output through the waveguide. It is because these modes overlapping with the waveguide band is suppressed by the radiation loss at the horizontal direction. The output waveguide selected the WGM and filtered other non-lasing modes.

Another series of samples with the parameters of $2.75a \leq R \leq 2.78a$, $0.23a \leq r \leq 0.27a$ and $a = 360$ nm were fabricated. The wavelengths of the lasing modes for the samples are summarized in Fig. 5.7. The lasing modes of the samples are summarized from the spectra collected by the 50× objective lens. The lasing modes show sharp peaks with narrow FWHM on the spectrum due to the high Q factor. Therefore, the wavelengths of the lasing modes are defined by the peaks with the smallest FWHM on the spectra. Figure 5.7 shows the graphs which compared the simulation and experimental results for the wavelength of the lasing mode dependent on R and r. The wavelengths of the lasing modes increase when R becomes larger and decreases when r becomes larger. It is corresponding to the trend of the simulated wavelength of the WGM in the circular cavity. The wavelength differences between measurement and simulation result should be attributed to the simplified structure used in the FDTD simulations. The InAs QDs were not contained when modelling the structure in simulations. It results that an offset in the band structure and wavelength of the lasing mode.

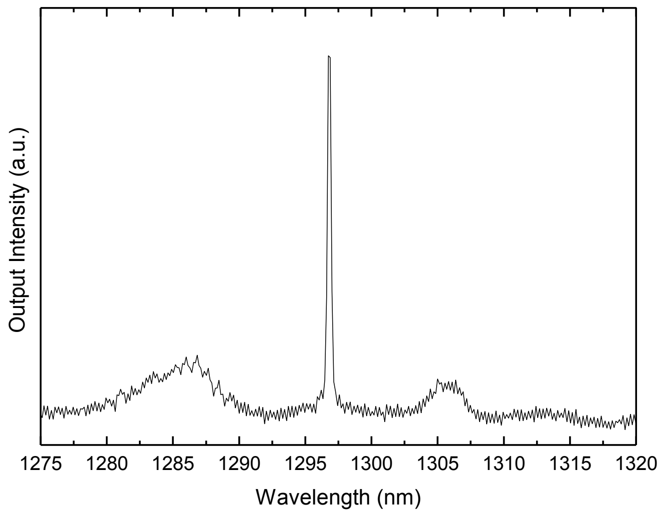

Fig. 5.6 Spectrum for sample b collected by the 50× objective lens and analyzed by the spectrometer.

WGM is a type of wave that can travel around concave part which is the periphery of the circular resonator in the fabricated samples [12]. Because the circular resonator was formed by 18 shifted air holes, the standing wave of the WGM in the circular resonator has 9 waves [13]. When R is larger or r is smaller, the periphery of the circular resonator becomes larger. Thus, wavelength of the WGM increases for keeping fitting the resonator perfectly. The matching of the experimental results and simulations implies that the lasing modes are the WGM in the circular resonators.

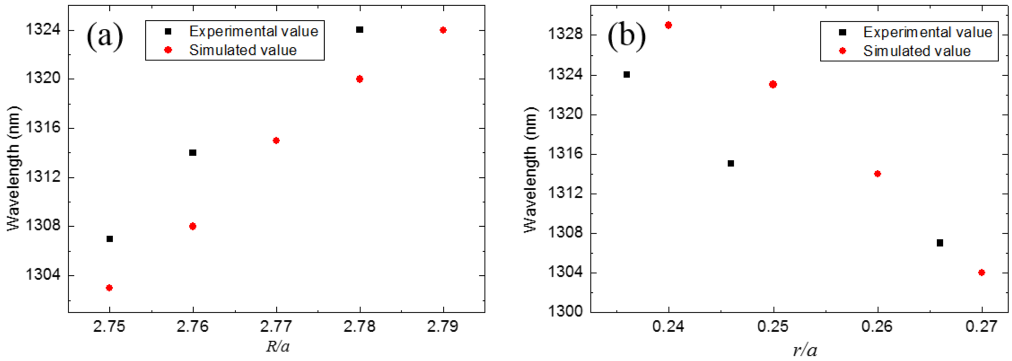

Fig. 5.7 The experimental wavelengths of lasing mode and simulated wavelengths for the WGM dependent on R or r. (a) r is fixed to be $0.27a$. (b) R is fixed to be $2.75a$. [2]

5.4 Summary

The lasing action in a PhC laser from the output waveguide by using a circular defect cavity has been demonstrated. The fabricated circular defect cavity performed a threshold excitation power of about 25 μW. The wavelength of the lasing mode depending on the R and r verified that the lasing mode is the WGM in the circular resonator. The observed optical properties of the circular defect cavity suggest a feasibility of realizing electrically driven PhC lasers with AlO_x cladding layers.

References

[1] K. Kukita, H. Nagatomo, H. Goto, R. Nakao, K. Nakano, M. Mochizuki, M. Kondow, M. Morifuji and F. Ishikawa: “Introduction of GaInNAs Gain Medium into Circularly Arranged Photonic Crystal Cavity,” Japanese Journal of Applied Physics 50, 102202 (2011).

[2] X. Zhang, T.Hino, S. Kasamatsu, S. Suga, E. He, Y. Xiong, M. Morifuji, H. Kajii, A. Maruta, and M. Kondow: “1.3µm lasing of circular defect cavity photonic crystal laser with an AlO_x cladding layer,” IEICE Electronics Express 14, 18 (2017).

[3] X. Zhang, Y. Togano, K. Hashimura, M. Morifuji and M. Kondow: “Dry etching of Al-rich AlGaAs with silicon nitride masks for Photonic crystal fabrication,” Japanese Journal of Applied Physics 54, 042003 (2015).

[4] M. Kondow, T. Kawano and H. Momose: “Selective Oxidation of AlGaAs for Photonic Crystal Laser,” Journal of Applied Physics 48, 050202 (2009).

[5] Y. Xiong, T. Okada, X. Zhang, M. Morifuji, M. Kondow: “Numerical Demonstration of the Feasibility of the Current Driven Photonic Crystal Laser Diode Used for Wavelength Division Multiplexing," ISCS 030 (2016).

[6] M. Morifuji, Y. Nakaya, T. Mitamura, M. Kondow: “Novel Design of Current Driven Photonic Crystal Laser Diode,” IEEE Photonics Technology Letters 21, 513 (2009).

[7] M. Nomura, S. Iwamoto, K. Watanabe, N. Kumagai, Y. Nakata, S. Ishida, and Y. Arakawa: “Room temperature continuous-wave lasing in Photonic crystal nanocavity,” Optics Express 14, 6308 (2006).

[8] S. Matsuo, T. Sato, K. Takeda, A. Shinya, K. Nozaki, H. Taniyama, M. Notomi, K. Hasebe, and T. Kakitsuka: “Ultralow Operating Energy Electrically Driven Photonic Crystal Lasers,” IEEE Journal of Selected Topics in Quantum Electronics 19, 4900311 (2013).

[9] S. Matsuo, T. Sato, K. Takeda, A. Shinya, K. Nozaki, H. Taniyama, M. Notomi, K. Hasebe, and T. Kakitsuka: “Room-temperature continuous-wave operation of lateral current injection wavelength-scale embedded active-region Photonic crystal laser,” Optics Express 20, 3773 (2012).

[10] M. Morifuji, and Y. Nakaya: “Numerical Design of Photonic Crystal Cavity Structure with AlAs/AlOx Cladding Layers for Current-Driven Laser Diodes,” Journal of Applied Physics 48, 112001 (2009).

[11] T. Okabe, M. Morifuji and M. Kondow: “Role of aluminum oxide cladding layers in heat transfer in a semiconductor slab with Photonic crystal,” Journal of Applied Physics 53, 022701 (2014).

[12] S. L. McCall, A. F. J. Levi, R. E. Slusher, S. J. Pearton, and R. A. Logan: “Whisperinggallery mode microdisk lasers,” Applied Physics Letter 60, 289 (1992).

[13] A. Tanaka, M. Kondow, and M. Morifuji: “Analysis of Cavity Waveguide Coupling in Two-Dimensional Photonic Crystals,” IEEE Photonics Journal 6, 4700309 (2014).

Chapter 6

Conclusions

In this study, the dry etching process for fabricating PhC structure in a GaAs/AlGaAs-based epi-wafer was optimized. Optical properties of the PhC laser with a circular resonator was measured.

In Chapter 3, the ICP deep dry etching of $Al_{0.8}Ga_{0.2}As$ for the fabrication of a PhC structure has been investigated firstly. By applying antenna power during the SiN_x mask etching process, the verticality of the air holes in the mask layer was improved owing to the contribution of chemical etching effect. Furthermore, when SiN_x was used as the mask layer, the vertical profile of the air holes fabricated by ICP dry etching was round because the charge up on the sidewall of the SiN_x mask layer bends the trajectories of the incident positive ions. Then, a thinner SiN_x mask layer was used to suppress the mask retardation and the effect caused by charge up. As a result, a PhC structure having air holes with a depth of 1.7 μm and a diameter of 190 nm was obtained.

Then, for realizing WDM by using the designed PC cavity laser with circular resonators operating at 1.3-μm range, the target filling ratio r/a of the PC structure was set to be larger than 0.3 when a is 340 nm. Due to the electron scattering in EB lithography process and mask retardation in mask etching process, the setting value in the EB lithography process and the thickness of the SiN_x mask layer were both optimized. Firstly, regular PhC patterns can be achieved on the resist when a_c was set as 340 nm and r_c was 75 and 80 nm in EB lithography process. Secondly, the thickness of SiN_x mask was optimized as 150 nm for protecting the substrate when etching the GaAs substrate. Finally, a GaAs PC structure with $r/a>0.3$ was successfully fabricated after mask removing process.

In Chapter 4, the experiments are aimed on optimizing the dry etching for GaAs/AlGaAs-based epi-wafers. The GaAs-based core layer with the InAs QDs in the epi-wafer shows selectivity when the dry etching recipe optimized for GaAs and $Al_{0.95}Ga_{0.05}As$ was used. The selectivity caused contractions on the diameter of the air holes. By reducing the antenna power, the contraction of the diameter for the air holes was reduced because of good balance between the physical etching effect and chemical etching effect for core layer was achieved. Finally, air holes with minor contraction were fabricated on the epi-wafer by using a multi-step etching recipe.

In Chapter 5, the lasing action in a PhC laser from the output waveguide by using a circular defect cavity has been demonstrated. The fabricated circular defect cavity performed a threshold excitation power of about 25 μW. The wavelength of the lasing mode depending on the R and r means that the lasing mode is the WGM in the circular resonator. The optical properties of the circular defect cavity show feasibility of realizing electrical driven PhC lasers using AlO_x cladding layers.

These results obtained show that the possibility of fabricating electrically driven CirD lasers, because the etching process was optimized and the lasing operation was confirmed on the circular resonator fabricated on the PhC structure. It also shows the possibility of applying the proposed CirD laser to intra-chip optical interconnections.

Appendix A

Influence of Fabrication Errors on Performance of CirD Laser

Fabricating errors always exist during the fabrication processes which may affect the performance of the fabricated CirD laser. The PBG which is generated by the periodic structure of the PhC structure is an essential element which is related to the confinement of the photons. However, the fabricating errors may distort the periodic structure, so that the PBG may shift and leakage of photons become more obvious. It is necessary to discuss the influence of the fabrication errors on performance of the fabricated CirD laser.

One typical fabrication error is induced by EB lithography process, which may cause the shape of the air hole not being an ideal circular, but an oval as shown in Fig. 1(a). A former student in our group, Mr. Katagiri, has discussed the influence on the PhC lasers with a line defect cavity when the shape of the air holes is oval in his thesis. The result has referential vale for discussing the CirD laser with air holes having irregular circular shape. In his thesis, he calculated the Q factor of the defect cavity in the PhC structure shown in Fig. 1(b) having air holes with different shape by applying the FDTD method. During the simulation progress, the area of the oval was set as a constant. The ratio of short axis r_2 and long axis r_1, and the degree Θ was used to adjust the shape of the air holes. When the ratio is 1, the shape of the air holes is an ideal circular. When the ratio is smaller, it means more sever fabricating errors in the EB lithography process. The oval center for each air hole and the structure used for calculation were always the same as shown in Fig. 1(b) for every calculation. The calculation focused on the variation of Q factor when the ratio of short axis r_2 and long axis r_1 or Θ changes.

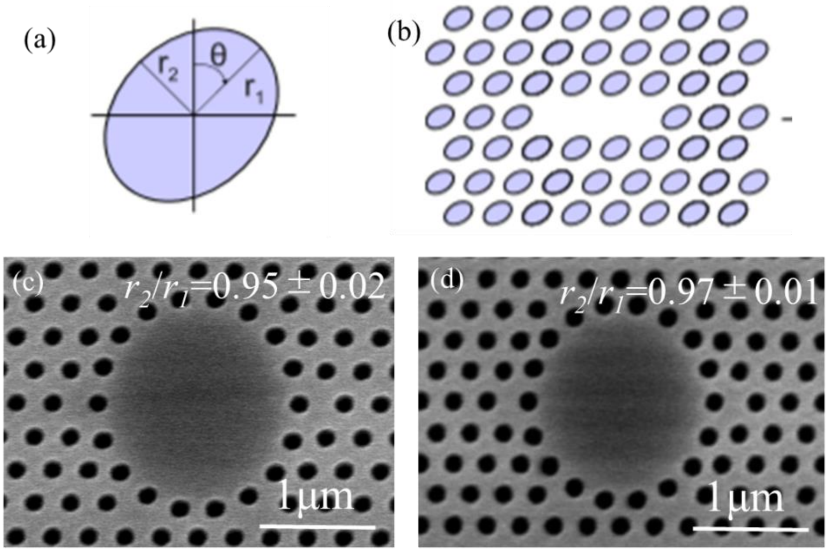

Fig.A1 (a) The oval shape used to simulate the fabricating errors on air holes. (b) The structure used to discuss the influence of fabricating errors. (c) and (d) Two typical SEM images of fabricated CirD laser which is introduced in Chapter 4.

The FDTD results show that when the ratio is larger than 0.9, no matter how much Θ is, the *Q* factor of the model shown in Fig. 1(b) varies within 20% and has no negative effects on the lasing properties. For example, when the ratio is 0.9, the biggest *Q* factor of 5800 is obtained when Θ is 30°, and smallest Q is 4800 when Θ is 0°. Because *Q* factor represents the attenuation of energy in the calculation field, this conclusion can also be applied to the CirD laser. Furthermore, because the simulated *Q* factor of the CirD laser is close to that of the structure shown in Fig. 1(b). If the ratio is larger than 0.9, the fabrication errors caused by EB lithography will not affect the lasing properties of CirD laser neither.

Fig. 1(c) and 1(d) show two typical SEM images of the CirD laser. r_1 and r_2 of 20 air holes for each picture were measured, and then get the average value of the ratio. The ratio of r_1 and r_2 is about 0.95 and 0.97 for these two pictures, which are both larger than 0.9. The estimation shows that the fabrication errors caused by EB lithography may not affect the lasing properties of the CirD laser in this study.

Acronyms and Abbreviations

1D	one-dimensional
CAD	computer-aided design
CCP	capacitively coupled plasma
CirD	circular defect cavity
CW	continuous-wave
EB	electron beam
FDTD	finite-difference time-domain
ICP	inductively coupled plasma
ICT	information and communication technology
LD	laser diodes
LEAP	lambda-scale embedded active-region photonic-crystal
OSA	optical spectrum analyzer
PBG	photonic band gap
PCSEL	photonic crystal surface emitting lasers
PhC	photonic crystal
QD	quantum dot
RIE	reactive ion etching
RT	room temperature
SEM	scanning electron microscope
SLF	spherical lensed fiber
TE	transverse electric
TM	transverse magnetic
UV	ultraviolet
VCSEL	vertical-cavity surface-emitting lasers
WDM	wavelength-division multiplexing
WGM	whispering gallery mode

Achievements

I. Publications

[1] Xiuyu Zhang, Yuji Togano, Kentaro Hashimura, Masato Morifuji, and Masahiko Kondow: “Dry etching of Al-rich AlGaAs with silicon nitride masks for Photonic crystal fabrication” Japanese Journal of Applied Physics 54, 042003 (2015).

[2] Xiuyu Zhang, Kento Takeuchi, Xiaolong Cong, Yifan Xiong, Masato Morifuji, Akihiro Maruta, Hirotake Kajii, and Masahiko Kondow: “Dry etching of deep air holes in GaAs/AlGaAs-based epi-wafer having InAs quantum dots for fabrication of photonic crystal laser”, Japanese Journal of Applied Physics 56, 126501 (2017).

[3] Xiuyu Zhang, Takafumi Hino, Satoshi Kasamatsu, Shobu Suga, Elbert He, Yifan Xiong, Masato Morifuji, Hirotake Kajii, Akihiro Maruta, and Masahiko Kondow: “1.3µm lasing of circular defect cavity photonic crystal laser with an AlO_x cladding layer”, IEICE Electronics Express 14, 18 (2017).

II. International Conferences

[1] Xiuyu Zhang, Kentaro Hashimura, Yuta Imada, Takahumi Hino, Tomoyuki Okada, Masato Morifuji, and Masahiko Kondow: “GaAs-based 2-dimensional Photonic crystal slab with large r/a used for wavelength-division multiplexing” the 43rd International Symposium on Compound Semiconductors, MoP-ISCS-031, Toyama, Japan, Jun. 27, 2016.

[2] Xiuyu Zhang, Masato Morifuji, and Masahiko Kondow: “Research of the multi-wavelength light source without multiplexer” International Symposium of Institute for Academic Initiatives, Osaka University “Opto Osaka 2015”, P-78, Osaka, Jan. 14, 2015.

[4] Yifan Xiong, Xiuyu Zhang, Elbert He, Ryo Tezuka, Takafumi Hino, Satoshi Kasamatsu, Masato Morifuji, Hirotake Kajii, and Masahiko Kondow: "Photonic Crystal Laser with Low-Quality Factor" the 25th International Semiconductor Laser Conference, WE50, Kobe, Japan, Sept. 14, 2016.

[5] Masahiko Kondow, Xiuyu Zhang, Yifan Xiong, and Masato Morifuji: "Stimulated emission from Photonic crystal cavity with AlOx cladding layer" 2016 Collaborative Conference on 3D & Materials Research, Mo-111-9, Seoul, Korea, Jun. 20, 2016.

[6] Yifan Xiong, Tomoyuki Okada, Xiuyu Zhang, Masato Morifuji, and Masahiko Kondow: "Numerical Demonstration of the Feasibility of the Current Driven Photonic Crystal Laser Diode Used for Wavelength Division Multiplexing" the 43rd International Symposium on Compound Semiconductors, MoP-ISCS-030, Toyama, Japan, Jun. 27, 2016.

III. Domestic Conferences

[1] Xiuyu Zhang, Kentaro Hashimura, Yuta Imada, Takahumi Hino, Tomoyuki Okada, Masato Morifuji, and Masahiko Kondow: "Optimized parameters of GaAs based 2-dimensional Photonic crystal slab having air hole arrays with a large radius" The 3rd KANSAI Nanoscience and Nanotechnology International Symposium, PS-72, Osaka, Japan, Dec. 8, 2015.

IV. Scholarship

[1] Research Promotion Scholarship, Marubun Research Promotion Foundation, 2016.

[2] Japanese Government (Monbukagakusho: MEXT) Scholarship, The Global University Project, 2015.04~2016.03.

Acknowledgements

First and foremost, I would like to express my sincere gratitude to my advisor Professor Masahiko Kondow (Division of Electrical, Electronic and Information Engineering. Graduate School of Engineering. Osaka University) for the continuous support of my Ph.D. study and related research, for his patience, motivation, and immense knowledge. His appropriate and critical advices always lead to successful research.

Besides my advisor, I am very grateful to Assistant Professor Masato Morifuji (Division of Electrical, Electronic and Information Engineering. Graduate School of Engineering. Osaka University), and Associate Professor Hirotake Kajii (Division of Electrical, Electronic and Information Engineering. Graduate School of Engineering. Osaka University) for their insightful comments and encouragement.

I would like to thank Professor Toshimichi Ito (Division of Electrical, Electronic and Information Engineering. Graduate School of Engineering. Osaka University) and Professor Masayoshi Tonouchi (Division of Electrical, Electronic and Information Engineering. Graduate School of Engineering. Osaka University) for reviewing the dissertation and giving valuable comments.

I would like to thank the rest of my thesis committee:Professor Yusuke Mori (Division of Electrical, Electronic and Information Engineering. Graduate School of Engineering. Osaka University), Professor Mitsuhiro Katayama (Division of Electrical, Electronic and Information Engineering. Graduate School of Engineering. Osaka University), Professor Masanori Ozaki (Division of Electrical, Electronic and Information Engineering. Graduate School of Engineering. Osaka University), Professor Katayama Ryuji (Division of Electrical, Electronic and Information Engineering. Graduate School of Engineering. Osaka University), Professor Nobuya Mori (Division of Electrical, Electronic and Information Engineering. Graduate School of Engineering. Osaka University), and Professor Tetsuya Yagi (Division of Electrical, Electronic and Information Engineering. Graduate School of Engineering. Osaka University) for their helpful suggestions on the dissertation.

I am also highly thankful to Professor Akihiro Maruta (Division of Electrical, Electronic and Information Engineering. Graduate School of Engineering. Osaka University) and Assistant Professor Masahiro Uemukai (Division of Electrical, Electronic and Information Engineering. Graduate School of Engineering. Osaka University) for their precious supports.

My sincere thanks also go to Professor Mitsuhiro Katayama (Division of Electrical, Electronic and Information Engineering. Graduate School of Engineering. Osaka University) and Assistant Professor Hiroshi Tabata (Division of Electrical, Electronic and Information Engineering. Graduate School of Engineering. Osaka University) for the use of the SEM apparatus. I also thank Mr. Hitoshi Kubo (Division of Electrical, Electronic and Information Engineering. Graduate School of Engineering. Osaka University) for the use of the sputtering apparatus.

I would like to thank my fellow lab mates Mr. Kentaro Hashimura, Mr. Yuta Imada, and Mr. Takahumi Hino for their supports and discussions on dry etching process. Also, I am very grateful to Mr. Yifan Xiong and Mr. Xiaolong Cong for their valuable comments.

Lastly, I would like to thank my whole family for all their love and encouragement. Especially, I sincerely express my gratitude to my father Henfa Zhang and my mother Shizhen Yu. I am also grateful to Ms. Yunyun Yang for her accompany and spiritual supports.